Theoretical investigation of n-butane isomerization in metal-substituted aluminosilicates

Zur Erlangung des akademischen Grades eines

DOKTORS DER NATURWISSENSCHAFTEN

(Dr. rer. nat.)

von der KIT-Fakultät für Chemie und Biowissenschaften

des Karlsruher Instituts für Technologie (KIT)

genehmigte

DISSERTATION

von

M. Sc. Lucas Fabian Spiske

1. Referent: Prof. Dr. Felix Studt
2. Referentin: apl. Prof. Dr. Karin Fink
Tag der mündlichen Prüfung: 23. Oktober 2023

Erklärung zur Selbstständigkeit

Ich versichere, dass ich diese Arbeit selbstständig verfasst habe und keine anderen als die angegebenen Quellen und Hilfsmittel benutzt habe, die wörtlich oder inhaltlich übernommenen Stellen als solche kenntlich gemacht und die Satzung des KIT zur Sicherung guter wissenschaftlicher Praxis in der gültigen Fassung vom 24.05.2018 beachtet habe.

Karlsruhe, den 18.02.2024, _____

Lucas Spiske

Abstract

The continuous increase of greenhouse gases in our atmosphere, which are the cause of the steady increase of the earths temperature, is to a large extent caused by the emission of such gases, for example carbon dioxide (CO_2), in industrial processes. In the petrochemical industry specifically, a large amount of CO_2 is produced through flaring of unwanted light hydrocarbons, like e.g. butane. To combat the problem of climate change caused by the increased production of greenhouse gases, it is paramount to utilize these side products in an efficient way. In the specific case of butane, catalytic isomerization into isobutane is possible. Isobutane is a much more valuable molecule as it can be diversely used in the industry e.g. to improve the octane number of gasoline, or for the production of methyl-tert-butyl ether (MTBE) via isobutylene. However, current catalysts that are used to catalyze this reaction contain toxic components, rendering the use of these catalysts hazardous and environmentally harmful. Therefore, thorough and vast research is necessary to discover efficient, cheap and ecofriendly catalysts for the n-butane to isobutane isomerization reaction.

This problem is tackled computationally by the use of highly accurate density functional theory (DFT) calculations. The underlying mechanisms of the n-butane isomerization reaction are investigated using a model catalyst, H-SSZ-13 (CHA structure), that is cost-effective and easy to calculate. The two main reaction pathways for the 2-butene isomerization that are extensively discussed in the literature, namely the monomolecular and bimolecular mechanisms, are optimized and compared to each other. Additionally, two novel reaction mechanisms are proposed, the (intermolecular) hydrogen transfer and the methyl transfer mechanisms. The former shows how olefinic species formed during the reaction can catalyze the reaction itself, while the latter provides a second pathway through which the formation of side products of the reaction may be explained. Reaction barriers were calculated for all mechanisms at a high level of theory. The results show that in the H-SSZ-13 zeolite, the monomolecular mechanism is favored above the bimolecular mechanism at 400 °C with a free energy barrier of 152 kJ/mol. The hydrogen transfer mechanism has a fairly high free energy barrier of 203 kJ/mol, while the barrier for the methyl transfer mechanism is very high at 227 kJ/mol and therefore not feasible at the considered reaction conditions.

These reaction mechanisms were then re-optimized in a variety of different zeolites and zeotypes of CHA, AFI and MOR structure. Different optimal reaction pathways were found for the monomolecular mechanism depending on the specific zeolite. The bimolecular mechanism was shown to be either competing or dominant in comparison to the monomolecular mechanism for zeolites with a higher framework acidity, which is the case for the AFI zeolite. The barriers for the hydrogen shift barriers range from 181 kJ/mol to 236 kJ/mol, meaning that for strongly acidic zeolites they still need to be considered, while the methyl transfer mechanism only shows barriers of $\geq$217 kJ/mol.

All the findings are finally concluded in linear scaling relations utilizing the ammonia heat of adsorption as a descriptor. These scaling relations are known to be able to predict the trends in reactivity in zeolite catalysis, and this also holds true for the reaction mechanisms investigated in this work.

Zusammenfassung

Der stetige Anstieg an Treibhausgasen in unserer Atmosphäre, welche der Grund für den konstanten Anstieg der Temperatur der Erde sind, beruht zu einem großen Teil auf der Emission dieser Gase, z.B. von Kohlenstoffdioxid (CO_2), durch industrielle Prozesse. Speziell in der petrochemischen Industrie wird eine große Menge an CO_2 durch Flaring von ungewollten leichten Kohlenwasserstoffen, wie z.B. Butan, produziert. Um das Problem des Klimawandels, welches auf dem erhöhten Ausstoß von Treibhausgasen beruht, zu bekämpfen, is es von hoher Wichtigkeit, diese Nebenprodukte effizient zu nutzen. Im Fall von Butan ist eine katalytische Isomerisierung zu Isobutan möglich. Isobutan ist ein sehr viel wertvolleres Molekül aufgrund der diversen Verwendungsmöglichkeiten in der Industrie, z.B. zur Verbesserung der Oktanzahl von Benzin oder in der Synthese von Methyl-tert-butyl-ether (MTBE) via Isobutylen. Jedoch enthalten gegenwärtig für diese Reaktion verwendete Katalysatoren toxische Komponenten, wodurch deren Verwendung gefährlich und umweltschädlich ist. Daher ist eine gründliche und breite Forschung notwendig, um effizientere, billigere und umweltfreundlichere Katalysatoren für die Isomerisierung von n-Butan zu Isobutan zu entdecken.

In dieser Arbeit wird dieses Problem rechnerisch mithilfe von sehr genauen Dichtefunktionaltheorie (DFT) Rechnungen angegangen. Die zugrundeliegenden Mechanismen der n-Butan Isomerisierung werden mithilfe eines Modell-Katalysators, H-SSZ-13 (CHA), untersucht, welcher kostengünstig und einfach zu berechnen ist. Die zwei in der Literatur ausgiebig diskutierten Reaktionspfade für die Isomerisierung von 2-Buten, nämlich der monomolekulare und der bimolekulare Mechanismus, werden in dem Zeoliten H-SSZ-13 optimiert und miteinander verglichen. Zusätzlich wurden zwei weitere Reaktionsmechanismen vorgestellt, der (intermolekulare) Wasserstoff-Transfer-Mechanismus und der Methyl-Transfer-Mechanismus. Ersterer zeigt eine Möglichkeit auf, wie Olefine, welche während der Reaktion gebildet werden, die Reaktion selbst katalysieren können, während letzterer einen zweiten Reaktionspfad beschreibt, durch welchen die Bildung von ungewünschten Nebenprodukten der Reaktion erklärt werden können. Die Reaktionsbarrieren wurden für alle Mechanismen mithilfe sehr genauer Methoden berechnet. Diese Barrieren zeigen, dass für den Zeolit H-SSZ-13 mit einer Barriere von 152 kJ/mol bei einer Temperatur von 400 °C der monomolekulare Mechanismus gegenüber dem bimolekularen Mechanismus bevorzugt wird. Der Wasserstoff-Transfer-Mechanismus hat eine eher hohe freie Barriere der freien Energie von 203 kJ/mol, während die Barriere für den Methyl-Transfer-Mechanismus mit 227 kJ/mol sehr hoch und daher bei den betracheten Reaktionsbedingungen nicht plausibel ist.

Diese Reaktionsmechanismen werden anschließend in einer Reihe von verschiedenen Zeoliten und Zeotypen von CHA, AFI und MOR neu optimiert. Für den monomolekularen Mechanismus werden abhängig von dem konkreten Zeoliten unterschiedliche Reaktionsp-

fade als optimal berechnet. Für Zeolite, welche eine höhere Azidität aufweisen, wie es für AFI der Fall ist, wird der bimolekulare Mechanismus als konkurrierend oder sogar als dominant gegenüber den monomolekularen Mechanismus berechnet. Die Barrieren des Wasserstoff-Transfer-Mechanismus reichen von 181 kJ/mol bis 236 kJ/mol, was bedeutet, dass diese im Fall von stark aziden Zeoliten berücksichtigt werden müssen, während der Methyl-Transfer-Mechanismus nur Barrieren von $\geq$217 kJ/mol aufzeigt.

Alle Resultate werden schlussendlich mittels linearer Skalierungsbeziehungen zusammengefasst, welche sich auf die Adsorptionsenergie von Ammoniak als Deskriptor beziehen. Es ist bekannt, dass diese Skalierungsbeziehungen Tendenzen in der Reaktivität von Zeolit-Katalysatoren voraussagen können, und dies gilt auch hier für die in dieser Arbeit untersuchten Reaktionsmechanismen.

Contents

1. Introduction

1.1. Future of Fossil Fuels

In the current time of climate change, there is a rising global conscience about the need to reduce the release of greenhouse gases into the atmosphere and to increase the use of green energy sources like solar energy and biomass. While the use of green energy in form of electricity from solar panels or plant-based biofuels is constantly rising, the vast majority of power used on earth is still, and will presumably be for a long time in the future, produced from fossil fuels. Due to the constantly increasing population, general life quality and resulting energy demands, the global consumption of fossil fuels is still increasing, as can be seen in Fig. 1.1.[1] However, fossil resources are finite and depleting. While fossil fuel reserves may be able to serve the energy demand for the next several decades, the increased emission of greenhouse gases like carbon dioxide (CO_2) will result in a drastic increase of the earths temperature due to the resulting increase of the greenhouse effect.[2] The problem of the rising temperature due to the greenhouse effect in the next several decades is a global problem caused by the use of fossil fuels, together with uncontrolled deforestation and modern forms of agriculture and farming. This increase in temperature due to these man-made effects, knowingly and inadvertently, will cause drastic changes to the earths climate and ecosystem, with the rise of the sea level, melting of ice around the poles, and many other effects taking place. These changes are also, as far as we are concerned, irreversible, as the regeneration of fossil fuels takes millions of years, classifying them as non-renewable energy sources.
While the causes and effects of global warming due to the increase of greenhouse-active gases like e.g. CO_2 and methane are well understood and widely accepted, at least in the scientific world, the global responses and actions taken to try to do something about this problem do not reflect the urgency of the matter. Enormous political and technological countermeasures are required if we are to curb the predicted threat to human habitats and ecosystems. As this is also, first and foremost, a multi-generational problem, we are in desperate need to find solutions to these problems now, since if we do not, the next generations afterwards will have to face the consequences of our inaction. However, this is a problem that requires a global and forward-thinking conscience and cooperation, which we most certainly do not have now. Still, we must always strive to search for and provide solutions for these issues, in order to improve upon the current situation to the best of our capabilities.

It is obvious that an abrupt stop of the use of fossil fuels in the near future is unrealistic for a multitude of reasons. For the next several decades, fossil fuels will stay the primary source for energy on planet earth. Therefore, continuous research in the field of fossil fuel refinement stays paramount for making sure that the fossil fuels which are used for energy production are used as efficiently as possible.
Three natural deposits fall under the definition of fossil fuels: coal, oil, and gas. Oil, also called crude oil or petroleum, is a complex mixture of smaller hydrocarbons, most commonly

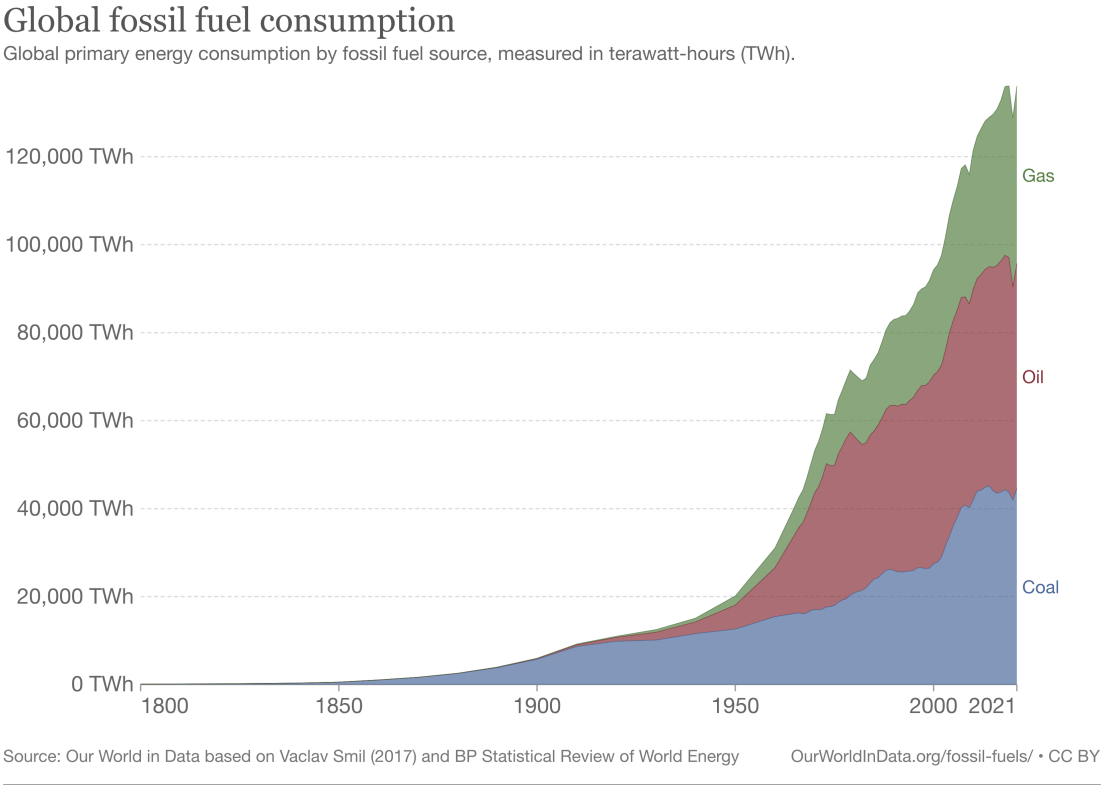

Figure 1.1.: Global primary energy consumption by fossil fuel source, split into the fossil fuels coal, gas, and oil. A clear exponential increase in the energy consumption can be seen, starting from around the beginning of the 20th century. This clear trend showcases that the global energy demand, and therefore also the consumption of fossil fuels, will further increase in the future. Adapted from Ref.[1] with permission from OurWorldInData.org, copyright 2022.

alkanes, cycloalkanes and aromatics, with small amounts of compounds containing nitrogen, oxygen and sulfur. Petroleum can be refined to high-value products like liquid fuels, solvents, lubricants and other products. Fuels derived from petroleum account for approximately one-third to one-half of the global energy supply.[3] While petroleum itself is a liquid, butane as one of its components is itself a gas with a high vapor pressure. Butane, which has the two isomers n-butane and isobutane, is not only a natural component of petroleum, but it is also a by-product of the catalytic cracking during the petroleum refinery process.[4] n-Butane, having a lower vapor pressure than its isomer isobutane, is blended into gasoline to regulate the vapor pressure of the fuel.[5] Through this process, the octane number of the produced fuels is controlled. Isobutane, on the other hand, is mostly used during the petroleum refining process as a feedstock to alkylation units. It is reacted together with C_3 to C_5 olefins to form isoparaffin compounds of high-quality gasoline.[4,5] Some refineries do not possess a hydrocracking facility for the supply of isobutane; in such cases, the abundant n-butane may be isomerized to isobutane.

Especially in the oil industry, flammable gases and vapors, like e.g. butane, in this case called associated gases, are oftentimes unwanted components or side products that are flared, i.e. burned to CO_2 and other components which are released into the atmosphere as a safe way of disposal.[6,7] According to a flare gas reduction report in 2011, flaring is a global environmental issue as it produces roughly 400 million tons of CO_2 per year, corresponding to about 2% of global CO_2 emissions from energy sources.[8]

This leads to the challenge of reducing the amount of flaring during the processing of fossil fuels, and to use these light hydrocarbons in a more energy-efficient way. One way to do

this is to improve upon the n-butane isomerization reaction towards isobutane, which is a much more valuable chemical than n-butane, used next to the petrochemical industry also as a reactant in the methyl-tert-butyl ether (MTBE) synthesis.[9] As this isomerization reaction is catalyzed by solid catalysts, experimental and theoretical investigations of the reaction mechanism, thermodynamics and kinetics of the reaction are paramount to be able to optimize catalysts and reaction conditions.

1.2. Zeolites as Capable Catalysts in Petrochemical Industry

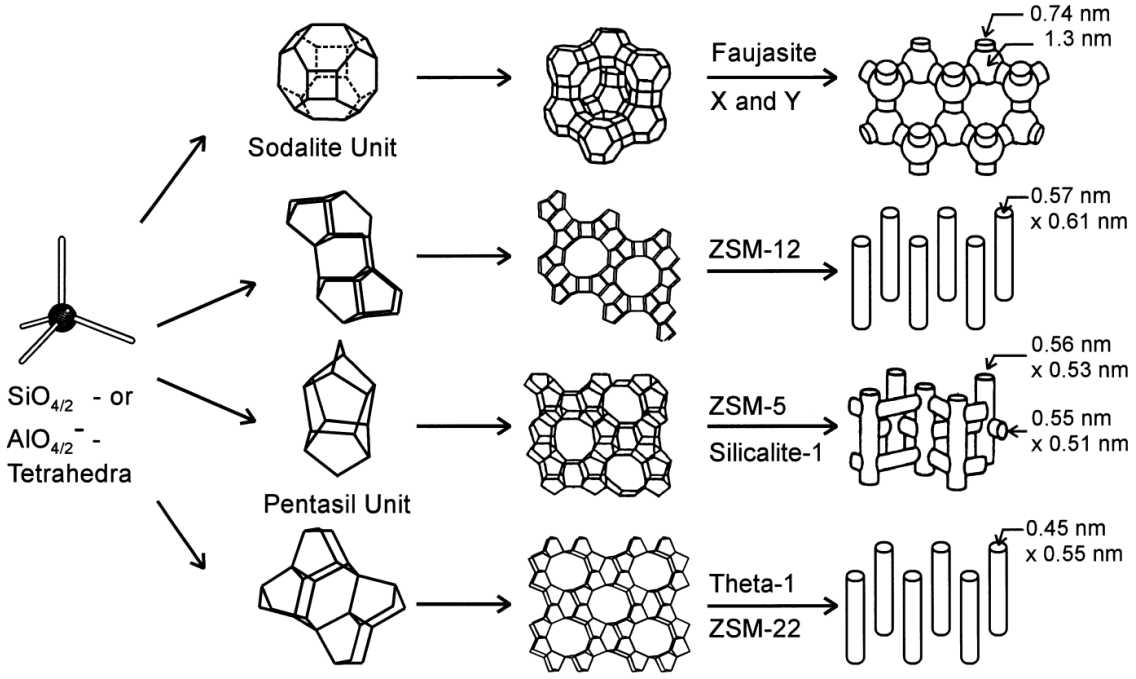

Figure 1.2.: Structures of four selected zeolites and how they are constructed from SiO_4 building blocks. Adapted from Ref.[10] with permission from Solid state ionics, copyright 2000.

Zeolites are microporous aluminosilicate minerals which can be found in nature.[10] As tectosilicates, their chemical formula follows the equation of $(Si + Al)/O = 1/2$, where the Si/Al ratio is variable.[11] Their elementary building blocks are SiO_4 and AlO_4 tetrahedra, meaning that every silicon and aluminum atom is surrounded by four oxygen atoms in a tetragonal way. These tetrahedra are connected at their edges by common oxygen atoms.[10] Utilizing these building blocks, a vast variety of three-dimensional structures can be formed. Currently, over 150 different zeolites have been synthesized, while about 40 of them are natural zeolites.[12] Some well known examples of zeolite structures are chabazite (CHA), faujasite (FAU), ferrierite (FER) and mordenite (MOR). In Fig. 1.2, it is shown how these three-dimensional structures can be constructed from simple SiO_4 tetrahedra. In the first column after the SiO_4 building unit, the smallest units which represent the periodic structure of the respective zeolite are shown. In computational chemistry, this is also referred to as the smallest possible unit cell, with a specific number of tetrahedral sites (T-sites). In the second column, larger superstructures of the zeolites are formed by repeating those units in all three spatial directions. This leads to pore and/or channel structures of the zeolites. For example, in the second row, the ZSM-12 zeolite has a channel structure with a channel diameter of 0.57 nm. The faujasite zeolite, however, has a pore structure.
If the zeolite structure contains alumina, the alumina will substitute a silica atom of the framework. Since Al^{3+} has one less valence electron than Si^{4+}, the resulting negative

charge is compensated by a hydrogen atom. This hydrogen atom will bind to one of the four neighboring oxygen atoms of the alumina. Due to it not being strongly bound to the zeolite framework, it is acidic in nature and can therefore facilitate reactions in a catalytic manner. The exact acidity itself depends on the zeolite framework. Due to these circumstances, the zeolite is now a very capable catalyst, where the acid site where the proton sits is the reactive center. Since the acidity and reactivity of the system depends on the framework structure of the zeolite as well as the Si/Al ratio, these catalysts can be fine-tuned towards the specific needs of any catalytic reaction by controlling these parameters. The choice of the zeolite and its framework properties also plays a big role especially in improving the selectivity towards certain products. As an example, some zeolites with a pore structure have only very small windows through which small molecules can diffuse into the pore. There, through catalytic reactions, larger molecules may be formed, which may then be too large to diffuse out of the pore again. For products to be able to diffuse out of the zeolite pore again, further reactions which result in a decrease in size of the trapped molecule are necessary. This is one simple way of limiting products using zeolite catalysts towards those below a certain size threshold.
The structure of a zeolite also plays a crucial role in product selectivity. Fig. 1.3 gives an illustrative example of this so-called shape-selective catalysis towards the reactants: While both possible reactants are C_7 alkanes, only the linear one is able to enter the zeolite pore, because the branched alkane is too bulky.[13] This is another advantageous charateristic of zeolites for product selectivity.

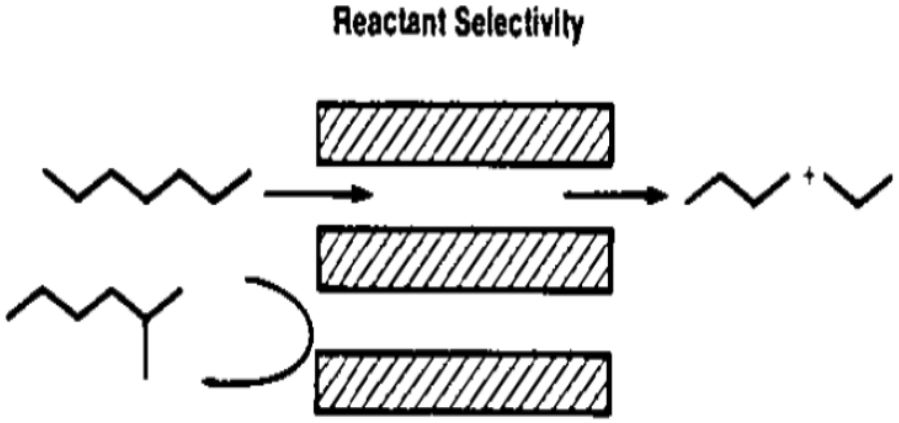

Figure 1.3.: Schematic diagram showcasing the shape selectivity towards linear molecules through pores of a zeolite catalyst. Bulky reactants are not able to enter the zeolite pore. Adapted from Ref.[13] with permission from the Chemical Society Washington, copyright 1976.

Zeolites are widely used especially in the fields of oil refining and petrochemistry due to the aforementioned beneficial properties, as well as non-toxicity, high surface areas, and low cost.[14] Additionally, zeolites are ion exchangers, meaning that they can act as Brønsted acids in catalytic reactions. Another large field of application of zeolites is the purification of water and wastewater due to their cation exchange capacity and adsorption kinetics.[15] Many non-natural zeolite structures have been synthesized to improve upon their catalytic features. Zeolite preparation is usually performed using hydro/solvothermal methods, and through the choice of reaction conditions like reaction time and temperature, the resulting zeolite structure can be controlled.[14]
While zeolites have been used in e.g. the petrochemical industry since the 1960s,[15] they have gained more and more attention over the years as catalysts. In Fig. 1.4, we show the number of scientific papers that have been published in the field of zeolite catalysis

each year from 1980 until now. A clear steady increase in the amount of research done can be seen, showcasing the growing importance of zeolites as capable and versatile catalysts. As of today, there exist a total of roughly 50000 publications in the broad field of zeolite catalysis.

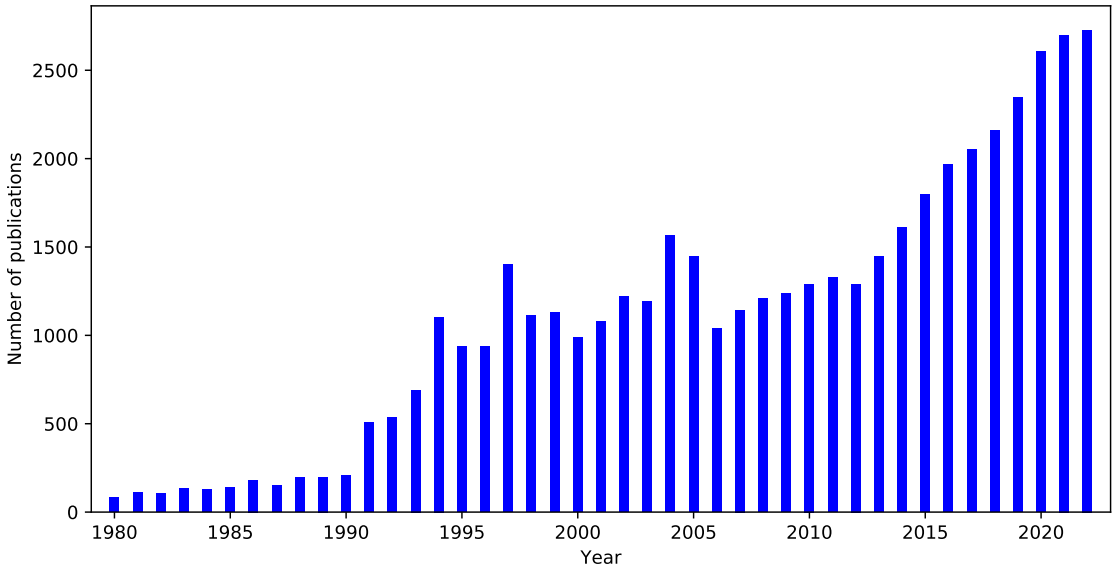

Figure 1.4.: Number of scientific papers published on zeolite catalysis each year from 1980 until 2022. Data was obtained from the Web of Science website[16] using the search keywords "Zeolite* and (Catalysis* or Catalyst*)".

1.3. Industrial Butane Isomerization

An isomerization reaction describes, as defined by the International Union of Pure and Applied Chemistry (IUPAC), a chemical reaction, where the product of the reaction is an isomer of the reactant, with isomers being species with the same atomic composition, i.e. molecular formula, but different line or stereochemical formulae, i.e. a different chemical structure.[17] This reaction is performed on a large industrial scale for the isomerization of n-butane to its only isomer isobutane. Due to the importance of this specific reaction as a large scale industrial process, we will discuss the catalysts used for the reaction as well as the (proposed) reaction mechanisms in detail.
One widely used catalyst for butane and higher alkane isomerizaion in industry is chlorinated alumina, oftentimes doped with platinum.[18] For alumina, $\gamma - Al_2O_3$ is used in experiments to investigate the catalyst. While alumina itself is already a solid-state acid, $\gamma - Al_2O_3$ alone is not active as a catalyst for the n-butane isomerization reaction even at high temperatures (i.e. <600 K).[19] Chloration of the alumina with CCl_4, however, greatly enhances the reactivity, explained by the formation of nascent $AlCl_3$[19] and the resulting increase in acidity.[9] Doping the catalyst with platinum to create $Pt/Al_2O_3 - Cl$ catalysts makes them applicable for n-butane isomerization even at low temperatures (120-200 °C).[20,21] In Fig. 1.5, we see how the butane equilibrium depends on the temperature. It is clear that for higher yields of the desired product isobutane, the reaction should be performed at lower temperatures.[22]

This is done in the only large-scale technology for n-butane isomerization right now, known as the *Butamer* process,[21] commercialized by UOP in 1941. This process is a fixed-bed catalytic process performed in vapor phase at 120-220 °C.[20] It is predominantly used in the industry due to its high conversion and selectivity.

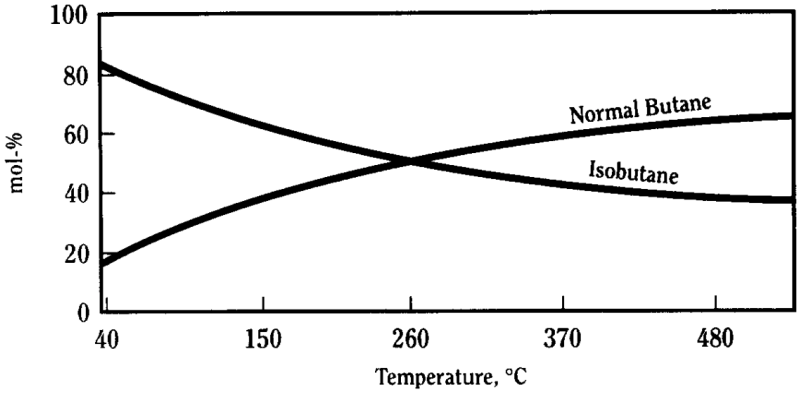

Figure 1.5.: Butane equilibrium, given in mol-%, depending on the temperature. Adapted from Ref.[22] with permission from Fuel Processing Technology, copyright 1993.

It is clear from thermodynamic considerations that the direct isomerization from n-butane to isobutane does not take place under reaction conditions. Instead, in the *Butamer* process, the isomerization is thought to proceed through three key steps: Dehydrogenation of butane to butene, isomerization of butene to isobutene, and hydrogenation of isobutene to isobutane.[22] (see also Fig. 1.4) The catalyst used for this reaction is the amorphous UOP I-8 catalyst, which consists of multiple components that each contribute in catalyzing one or more of those reaction steps. These catalysts are therefore called bifunctional catalysts. Since the discovery of the original I-8 catalyst, newer catalysts called I-80, I-84, I-122 and I-124 have been developed, showcasing higher performance.[23] While the exact catalyst components are proprietary information, the general structure as well as the activity and selectivity are known. For the first and last step, namely the dehydrogenation and hydrogenation reactions, an active metal of group 8 of the PSE is dispersed on a highly porous substrate, which helps facilitate these reactions.[22] For the isomerization of the olefin, a strong acid site is needed for the protonation of the olefin. The formed secondary carbonium ion can then isomerize through a cycloalkyl intermediate to the tertiary isobutyl cation.
One of the major drawbacks of the *Butamer* process is that it is necessary to add toxic organic chlorides to the raw reactant stream to maintain the activity of the catalyst, which of course causes environmental problems.[20,23]
Next to the chlorinated alumina catalysts, sulfated zirconia (SZ in short) catalysts have been extensively investigated and tested for the butane isomerization reaction. It was found that treatment of ZrO_2 with sulfuric acid and subsequent calcination leads to a sulfated zirconia catalyst ($S - ZrO_2$) that is active for butane isomerization at low temperatures.[9,24] Similar to the chlorinated alumina catalyst, addition of Pt leads to an increase in activity and stability of the catalyst. While sulfated metal oxide catalysts in general provide many advantages over chlorinated alumina, like lower operation costs and no need for chlorine, the drawbacks are the lower activity and therefore harsher reaction conditions, specifically for the butane isomerization reaction.[20] While originally Pt was used here the same way it is used for C_5 and C_6 isomerization, Pd has been found to be more active at low temperatures and a greater stability against impurities than Pt,[23] most likely due to a different isomerization mechanism. Some larger scale processes have been set up using these Pd-SZ catalysts. In Fig. 1.6, the main industrial butane isomerization process with the chlorinated alumina catalyst is compared to other isomerization processes. The yield of hydrocarbons is very high for all examples, although it is still the highest for the UOP *Butamer* process at 98%.

A third class of catalysts that have become increasingly popular in catalysis in general, but

No.	Parameter	UOP process on chlorinated catalyst	NPP Neftekhim process on oxide catalyst	Process on catalyst Pd-SZ, IC SB RAS
1	Process temperature, °C	160–220	180–220	120–160
2	Pressure, MPa	2.5–3.2	1.0–1.5	2.0–2.5
3	Feed space velocity, h^{-1}	6.0–8.0	6.0–10.0	4.8–8.0
4	Molar ratio H_2/butane	0.03–0.07	0.06–0.1	0.05–0.15
5	*n*-Butane conversion per pass, %	50–60	50–55	60–65
6	Yield of C_{4+} hydrocarbons per pass, %	98	94–95	92–96

Figure 1.6.: Comparative characteristics of different n-butane isomerization processes. UOP utilizes a chlorinated alumina catalyst in its *Butamer* process, NPP Neftekheim utilizes an oxide catalyst, and the Institute of Catalysis, Siberian Branch of Russian Academy of Sciences utilizes a Pd sulfated zirconia catalyst. Adapted from Ref.[23] with permission from Pleiades Publishing Ltd., copyright 2019.

also in the petrochemical industry, are zeolite catalysts, as we have already discussed in section 1.2. There are different reaction mechanisms proposed for the n-butane isomerization over zeolites, but up to date, no clear consensus has been drawn yet as to which of those mechanisms is predominant in which type of zeolite. The two main reaction mechanisms are the monomolecular mechanism, where butene isomerizes through a cyclopropyl cation, and the bimolecular mechanism, where two butene molecules dimerize to C_8, and crack into fragments again after rearrangement. The mechanistic details of the butene isomerization reaction is discussed in section 1.4.
Frequently investigated zeolite structures for these reactions are MOR, CHA and H-ZSM-5.

1.4. Butane Isomerization Mechanisms

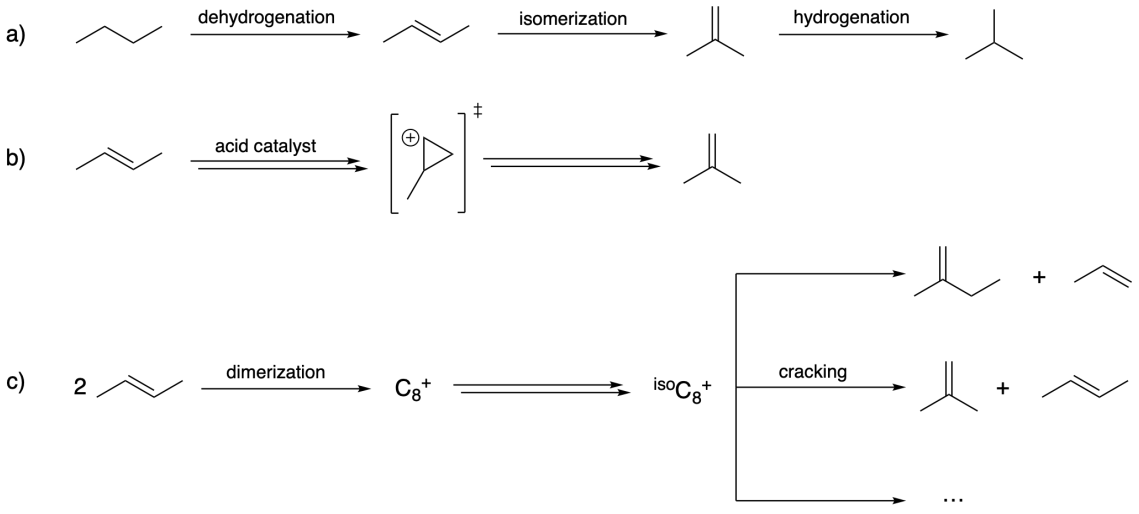

Figure 1.7.: Scheme of the catalytic n-butane isomerization mechanisms. a) Overview of the isomerization process, consisting of the dehydrogenation, isomerization and hydrogenation steps. b) Monomolecular 2-butene isomerization pathway. c) Bimolecular 2-butene isomerization pathway; depending on the structure of $^{iso}C_8^+$, the cracking reaction will yield olefins of different chain lengths.

A general overview of the butane isomerization reaction mechanisms is given in Fig. 1.7. Fig. 1.7a shows that the isomerization does not take place directly from n-butane to isobutane; rather, the olefin can isomerize to isobutene only after the dehydrogenation of butane to butene. Isobutene is then hydrogenated again to isobutane. The origin of the first olefins in this reaction is still not clear to this day. Some suggest that some olefins

may be present from the start of the reaction due to small impurities of the reactant feed, while others argue that coking of the catalyst may result in unsaturated hydrocarbons able to start the reaction.[9] Independent of the origin of the olefinic species, Wulfers et al.[25] have shown that adding small amounts of olefins to the reactant feed greatly increases the rate of isobutane production. This underlines the importance of olefinic species for the start of the isomerization reaction.
Fig. 1.7b shows the monomolecular (sometimes referred to as unimolecular) mechanism of butene isomerization. Here, the olefin is protonated by an acidic catalyst (in our case a zeolite). The transition state of the isomerization itself is a cyclopropyl cation. The reaction mechanism is shown and explained in more detail, for a variety of different zeolite catalysts, in the following chapters.
Fig. 1.7c shows the bimolecular mechanism, with two butene molecules as the reactants. The two C_4 molecules can dimerize due to the acidic catalyst to a C_8^+ cation. This cation can then rearrange to different $^{iso}C_8^+$ structures. Depending on the cation structure, cracking will yield different products, e.g. 2 C_4 olefins or a C_3 and a C_5 olefin. These side products are generally not wanted and therefore lower the selectivity towards the desired C_4 product. Due to the size of the C_8 fragments, the selectivity between the monomolecular and bimolecular mechanisms may be controlled through the choice of catalyst structure due to their confinement effects and shape selectivity.
While the skeletal isomerization of longer chain hydrocarbons is rather well understood and thought to occur via the monomolecular pathways,[26,27] mechanisms for the isomerization of n-butane are still debated with experiments suggesting that the bimolecular mechanism might also play a dominant role.[9,28–33] Although both the unimolecular and bimolecular mechanisms are widely accepted as the two possibilities for n-butane isomerization, no clear consensus has been reached yet as to which of these pathways contributes to which extent towards product formation.
While earlier research proposed the bimolecular mechanism as the main reaction pathway,[28,29] recent research states that the monomolecular mechanism is favored.[25,33,34] The bimolecular pathway, however, is thought to be responsible for the formation of unwanted products that lead to lower product selectivity and deactivation of the catalyst.[33] In a recent article, the influence of both acid site density as well as support acidity/metal balance are discussed as important factors impacting the ratio of the monomolecular to bimolecular mechanism.[35]
Both mechanisms are thought to occur via the formation of olefinic intermediates. Recently, the influence of olefins on the conversion and product distribution has been investigated,[25] and a clear preference towards the monomolecular mechanism has been found. However, further investigations are still needed to understand how side products with different chain lengths such as C_3 and C_5 are formed.

1.5. Computational Chemistry in Zeolite Catalysis

In addition to the experimental findings, a deeper mechanistic understanding of the reaction mechanisms at hand can lead to further and more detailed insight into the reasons why some catalysts prefer one mechanism over the other. Theoretical calculations are able to substantiate experimental findings, and vice versa. There are many structural effects or energetic values, especially in zeolite catalysis, that are important to the reactivity of the system, but very hard (or sometimes even impossible) to measure experimentally. This includes adsorption energies, dispersion effects and reaction barriers. With quantum chemical methods, however, all these values can be calculated by modeling the catalyst structure and optimizing the reactant structure and transition states for the reaction.
The by far most used quantum chemical method is density function theory (DFT), as

will be described in detail in chapter 2.2. The PBE-D3 functional,[36–38] with the D3 part signifying a dispersion correction, is a widely used functional to investigate zeolite catalysts. However, simply using this functional likely leads to very large errors in reaction energies and especially barriers. This has been shown by investigating the accuracy of the PBE-D3 functional, among other functionals, on zeolite catalysts, specifically reaction energies and barriers that are typical to the methanol-to-olefins (MTO) process.

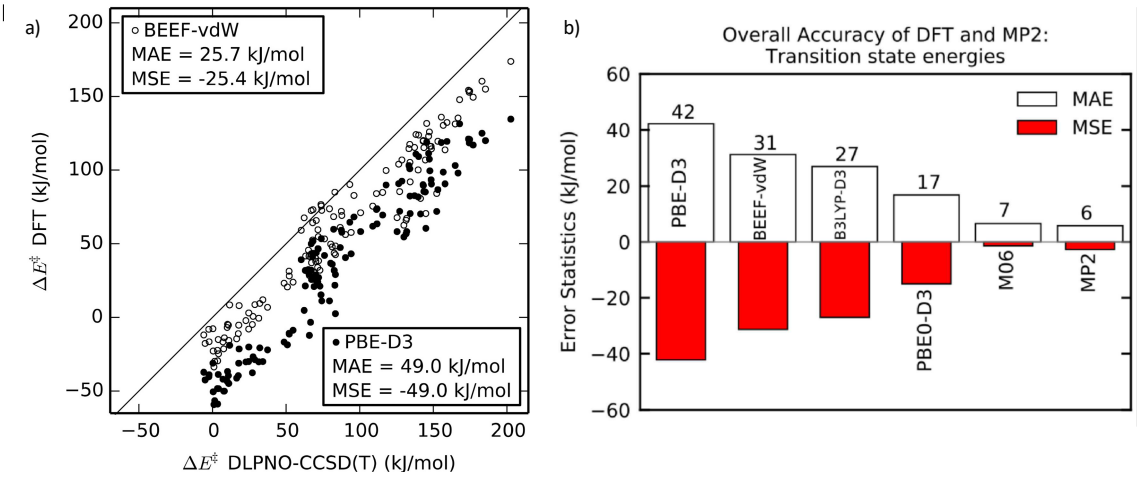

Figure 1.8.: a) Parity plot for the activation barriers investigated in the SSZ-13 and SAPO-34 zeolites. PBE-D3 values are compared to DLPNO-CCSD(T) values. Figure adapted from Ref.[39] with permission from the Journal of Physical Chemistry Letters. b) Comparison of high-accuracy DLPNO-CCSD(T) transition state barriers with the PBE-D3 method, among others. The mean absolute errors (MAE) as well as the mean signed errors (MSE) are given for each method. Figure adapted from Ref.[40] with permission from Wiley-VCH Verlag GmbH & Co. KGaA, Weinsheim.

Fig. 1.8a shows a parity plot comparing the computed activation barriers for a set of 130 reaction barriers using both the PBE-D3 and the BEEF-vdW functionals against the high-accuray DLPNO-CCSD(T) method, utilizing the cluster model approach (see chapter 2.6).[39] The zeolites investigated in this study were the SSZ-13 as well as the AlPO-34 zeolites. Focussing on the PBE-D3 results, it can clearly be seen that the calculated barriers using this functional are vastly underestimated in comparison to the high-accuracy method, with a mean signed error (MSE) of -49 kJ/mol. A similiar result has been obtained by Goncalves et al.,[40] who investigated a smaller, but very similar set of 17 reactions for the SSZ-13 and Cu-SSZ-13 zeolites, also utilizing the same cluster model approach. The results of this particular investigation are shown in Fig. 1.8b. Very similar findings of vastly underestimated reaction barriers (MSE=-42 kJ/mol) for these reactions substantiate the previous findings in Fig. 1.8a. Additionally, among others, the M06 hybrid functional[41] was investigated on its accuracy towards these reactions, and a very low mean average error (MAE) of only 7 kJ/mol was reported. The accuracy is the same, if not slightly better, than the oftentimes used DLPNO-CCSD(T) method[42–44] for the cluster model correction. Therefore, this functional is used in this thesis to calculate single point energies of the cluster model structures to improve upon free energies.

Through the use of these computational methods, calculation of energies that are descriptive for the acidity of a zeolite catalyst are possible at a very high accuracy. These descriptors include the adsorption energies of small molecules like alkanes and olefins, ammonia (NH_3) and carbon monoxide (CO). Especially the ammonia heat of adsorption can serve as a strong guide to the reactivity of a catalyst in comparison to similar catalysts,[45–47] and is cost-effective to calculate. Using it as a descriptor, it is possible to compare the reactivities of various zeolites with the same base structure, but different acid site substitutions, to

each other.
For any zeolite framework, it is possible to construct different zeotypes by changing the framework atoms and/or the acid side atom. By doing this, a large amount of different zeotypes of the same framework type can be constructed. The reaction pathways can then rather easily be investigated for other zeolites. This is a huge advantage in zeolite catalysis, as many different catalysts can be screened at a comparatively low computational cost this way.
Additionally, the effect of confinement can indirectly be calculated through the calculation of reaction barriers in zeolites which only differ in their framework structure. As an example, both the AFI and the MOR zeolites have channel-like structures, but their channel sizes are slightly different. While the AFI and MOR channels are both constructed by 12-membered rings, the AFI channel is almost perfectly circular, while the MOR channel is more oval. This may result in different reactivities especially for large molecules which are adsorbed inside the zeolite.

1.6. Scope of the Thesis

This work aims to contribute to the understanding of the catalytic n-butane isomerization reaction over a variety of different zeolite structures. By utilizing Density Functional Theory (DFT) calculations together with high-level accuracy cluster model corrections, the reaction mechanisms for the 2-butene isomerization reaction to isobutene have been calculated in H-SSZ-13 as a model catalyst. An intermolecular hydrogen shift mechanism is proposed to explain the formation of olefins from alkanes and vice versa, together with a methyl shift transfer as an additional reaction pathway that leads to prominent side products.
The optimized reaction pathways are then transferred and re-optimized in a variety of different zeolite structures to gain a deeper understanding of how well different zeolites are able to catalyze the n-butane isomerization reaction due to their different Brønsted acidities and confinement effects. Furthermore, linear scaling relations are established to help predict the catalytic reactivity of zeolites for this reaction without having to fully investigate the whole reaction pathway at a high level of theory.
Lastly, the MOR zeolite is investigated for the n-butane isomerization reaction, and kinetic simulations were performed to investigate the reaction rates which are then compared to experimental findings for this specific zeolite.
The contents of this thesis can be summarized by the following[1]:

- Chapter 2 gives an introduction to the computational methods that are used in this thesis, as well as specific details about the geometry of the chemical structures investigated herein.
- Chapter 3 focuses on the two 2-butene isomerization mechanisms, which are the monomolecular and the bimolecular isomerization mechanisms of 2-butene to isobutene.

[1]The results shown in chapters three to six are based on the following publications:

- L. Spiske, P. N. Plessow, K. Kazmierczak, B. D. Vandegehuchte and F. Studt. Theoretical investigation of catalytic n-butane isomerization over H-SSZ-13. *Front. Catal.* 3, 2023.
- M. E. Potter, L. Spiske, P. N. Plessow, E. B. McShane, M. Carravetta, B. Vandegehuchte, K. Kazmierczak, F. Studt and R. Raja. Combining computational and experimental studies to gain mechanistic insights for n-butane isomerisation with a model microporous catalyst. *Submitted to Cat. Sci. Technol.*
- L. Spiske, P. N. Plessow, K. Kazmierczak, B. D. Vandegehuchte and F. Studt. Towards predicting trends for n-butane isomerization in zeolite catalysis. *In preparation.*
- L. Spiske, P. N. Plessow, K. Kazmierczak, B. D. Vandegehuchte and F. Studt. Kinetic simulations of the n-butane isomerization over acidic mordenite. *In preparation.*

The mechanisms of those two pathways were first optimized in the model CHA catalyst H-SSZ-13, and then transferred to different CHA and AFI zeotype structures, as well as the MOR zeolite. Differences in barrier heights for the rate-determining steps (RDS) between the two mechanisms are discussed, as well as the respective influences the enthalpy and entropy contributions have on the free energy barriers. Lastly, the influence of the reaction temperature on the competing mechanisms is discussed for a range from 100 °C to 700 °C.

- Chapter 4 deals with the formation of prominent side products that are formed during the reaction. The specific product distribution of the n-butane isomerization reaction is discussed based on experimental findings. A methyl transfer mechanism is proposed, which is able to convert a C_4 olefin into C_3 and C_5 by means of methyl transfer reactions to and from surface methoxy species. The RDS of this mechanism is identified, and the reaction steps up to and including this barrier are optimized in all investigated zeolites herein, and subsequently discussed. The methyl transfer mechanism is then compared to the uneven β-scission in the bimolecular mechanism, through which side product formation is usually explained in the literature.
- In chapter 5, the origin of olefinic species during the n-butane isomerization reaction is discussed. After a general discussion of possible origins of those species, a hydrogen transfer mechanism is proposed, which describes how even small amounts of olefin can catalyze the isomerization reaction, since the olefin itself is reproduced during the reaction. Similar to the earlier chapters, this mechanism is optimized in all investigated zeolites, and RDS barriers are subsequently discussed.
- In chapter 6, linear scaling relations are used to investigate the dependency of the RDS barriers for each zeolite on their acidity, described by the ammonia heat of adsorption. The quality of those scaling relations is discussed, as well as how well they are able to correctly describe trends even at a lower level of theory. Furthermore, the influence of both zeolite acidity and confinement effects are investigated and discussed using these scaling relations. Last, the overall predictive power of reaction enthalpies calculated at the PBE-D3 level of theory is assessed by comparison with the M06 level of theory in a parity plot.

2. Computational Methods

2.1. Introduction

For the accurate calculation of all chemical structures and properties in the field of computational chemistry, the application of sophisticated computational methods is needed. However, even after running highly demanding computational calculations, one still needs to carefully judge the accuracy of the results based on the system investigated and the methods used.
The reason for this is the fact that for these quantum chemical calculations, it is impossible to calculate an exact solution for any chemical system (that involves more than one electron). In the 17th century, Sir Isaac Newton derived the physical laws of classical mechanics. Using these laws, one might argue that it should be possible to fully calculate the position and velocity of any particle at any given point in time; this is also referred to as determinism. Unfortunately, an exact analytic solution to an n-body problem can only be found for n $\leq$ 2. The same is the case in quantum mechanics, where any system containing more than one electron cannot be exactly solved (more precisely, the electron-electron interaction term cannot be solved exactly). This leads to the conundrum of having to approximate the energies of systems to the best of ones abilities, and trying to get as close to the actual correct energy of a system as possible. To tackle this problem, a multitude of theories have been proposed, supplying us with the tools to try to calculate our chemical systems of interest as accurately as possible. Some of these theories are the Hartree-Fock Theory, Post-Hartree-Fock Theories like Coupled Cluster, Full-CI, and more; and Density Functional Theory (DFT). DFT in particular is the theory of choice for most computational scientists as it arguably provides the best trade-off between computational cost and accuracy. This is why DFT was also used in all calculations in this thesis, and the majority of the Computational Methodology section is focused on DFT.
In the following, the most important aspects of DFT, as well as further aspects for quantum chemical calculations, are discussed.

2.2. Density Functional Theory

The main goal in computational chemisty is (in the case of non-relativistic calculations) always the same: To solve the Schrödinger equation for a given system Ψ to get the energy of the system, E, as a solution. The Schrödinger equation in its simplest form reads

$$\hat{H}\Psi = E\Psi \ , \tag{2.1}$$

where $\hat{H}$ is the Hamiltonian operator. This Hamiltonian consists of contributions of the kinetic energy of both nuclei and electrons, the coulomb attraction between the two, the electron-electron repulsion and the nucleus-nucleus repulsion, and reads

$$\hat{H} = -\sum_{i=1}^{N}\frac{1}{2}\nabla_i^2 - \sum_{A=1}^{M}\frac{1}{2M_A}\nabla_A^2 - \sum_{i=1}^{N}\sum_{A=1}^{M}\frac{Z_A}{r_{iA}} + \sum_{i=1}^{N}\sum_{j>i}^{N}\frac{1}{r_{ij}} + \sum_{A=1}^{M}\sum_{B<A}^{M}\frac{Z_A Z_B}{R_{AB}} \ . \tag{2.2}$$

Here, R_A and r_i describe the position vectors of the nuclei and eletrons, respectively; r_{iA} is the distance between electron i and nucleus A; r_{ij} is the distance beween the two electrons i and j; R_{AB} is the distance between two nuclei A and B; ∇ is the Laplacian operator; M_A is the ratio of the mass of nucleus A to the mass of one electron; and Z_A is the atomic number of nucleus A. It is important to note here that this Hamiltonian is given in atomic units, where the following convention is used:

$$e = m_e = \hbar = \frac{1}{4\pi\epsilon_0} = 1 \ . \tag{2.3}$$

Now, the Born-Oppenheimer-Approximation can be used to simplify this operator. In short, the kinetic energy of the nuclei (the second term in 2.2) is assumed to be zero because the mass of a nucleus is assumed to be infinitely greater than the mass of an electron, and therefore the nuclei are stationary compared to the electrons. Subsequently, it can also be assumed that the interaction energy between nuclei and eletrons (third term in 2.2) is constant, and therefore not impacting the wave function Ψ. Thus, the remaining electronic part of equation 2.2 can be written in a concise manner:

$$\hat{H} = \hat{H}_{\text{el}} = \hat{T}_{\text{e}} + \hat{V}_{\text{e}} + \hat{V}_{\text{ext}} \ , \tag{2.4}$$

where the electronic Hamiltonian simply consists of the kinetic energy operator $\hat{T}$, and the potential energy operators $\hat{V}$. The external energy operator $\hat{V}_{\text{ext}}$ contains not only the electron-nuclei interaction from the equations above, but can also contain other external fields, like electronic or magnetic fields.
Now, a way to describe our system of electrons and nuclei is needed. While older computational methods, like for example Hartree-Fock methods, make use of wave functions derived from Slater determinants to describe Ψ, the focus here will only lie on the Density Functional Theory approach, or DFT in short. In this theory, one makes use of the idea that only the electron density $\rho(r)$ is necessary to fully describe any system, and the energy of the system is then given as a functional of that density:

$$E = E[\rho(r)] \ . \tag{2.5}$$

Proving this requires some long and sophisticated mathematics and has been done by Hohenberg and Kohn, who postulated two theorems for it. Therefore, it will only shortly be discussed how this approach can be justified.

2.2.1. The Hohenberg-Kohn Theorems

In DFT, when an electron density $\rho(r)$ is used to describe a system, the electrons of the system interact with one another and with an external potential $\hat{V}_{\text{ext}}$. It needs to be proven that the electron density (which we take to be the ground state density) describes the Hamiltonian to connect the density with the energy of the system. This can be done by a *reductio ad absurdum* proof, where an assumption of the existence of two different external potentials with the same ground state density ρ_0 is disproven, and therefore proving that the non-degenerate ground state density ρ_0 determines the external potential. This is the first Hohenberg-Kohn Theorem, the Existence Theorem.
The second Hohenberg-Kohn Theorem is the Variational Theorem. In Hartree-Fock theory, it can be easily shown that the expectation value of the Hamilton operator for a wave function is always greater or equal the exact energy E_0 of the system:

$$E_{\text{VP}} = \frac{\left\langle \Psi \middle| \hat{H} \middle| \Psi \right\rangle}{\langle \Psi | \Psi \rangle} \geq E_0 \ . \tag{2.6}$$

The same can be done here to show that the electron density also obeys the variational principle. This then means that the ground state electron density gives us the ground state

energy E_0.
Through those two theorems, it has been proven that the ground state electron density describes the external potential. Therefore, it is now possible to describe any system by its electron density $\rho(r)$ instead of a wave function Ψ.

2.2.2. Kohn-Sham Equations

They key assumption that is made now is that the electrons in the system are non-interacting. The energy of the system can then be conveniently split up into different contributions:

$$E[\rho(r)] = T_{\mathrm{ni}}[\rho(r)] + V_{\mathrm{ne}}[\rho(r)] + V_{\mathrm{ee}}[\rho(r)] + \Delta T[\rho(r)] + \Delta V_{\mathrm{ee}}[\rho(r)] \ . \tag{2.7}$$

These terms describe the kinetic energy of the non-interacting electrons, the nuclear-nuclear interaction, the potential energy of the nuclear-electron interaction (these first three terms as the first three terms on the right hand side of Eq. 2.2), the kinetic energy correction from the electron-electron interaction (which we first assumed to be non-interacting), and the non-classical corrections to the electron-electron repulsion energy, respectively. The electron-electron repulsion energy is also often described with the Coulomb-Operator $\hat{J}$. If the electron density is assumed to be described by the orbitals χ_i, which are themselves one-electron wave functions, one can construct the many-electron wave function as in the form of a Slater determinant:

$$\rho = \sum_{i=1}^{N} |\chi_i(r)|^2 \ . \tag{2.8}$$

By doing this, the energy of Eq. 2.7 can then be written within an orbital expression for the density as

$$\begin{aligned} E[\rho(r)] = \sum_{i}^{N} \left(\left\langle \chi_i \middle| -\frac{1}{2}\nabla_i^2 \middle| \chi_i \right\rangle - \left\langle \chi_i \middle| \sum_{k}^{\text{nuclei}} \frac{Z_k}{|r_i - r_k|} \middle| \chi_i \right\rangle \right) \\ + \sum_{i}^{N} \left\langle \chi_i \middle| \frac{1}{2} \int \frac{\rho(r')}{|r_i - r'|} dr' \middle| \chi_i \right\rangle + E_{\mathrm{xc}}[\rho(r)] \ . \end{aligned} \tag{2.9}$$

All electron-electron interactions except the Coulomb term are put into the term E_{xc}, where the subscript stands for exchange correlation (XC). From Eq. 2.9, the Kohn-Sham equation

$$h_i^{\mathrm{KS}} \chi_i = \epsilon_i \chi_i \tag{2.10}$$

can be derived, with the Kohn-Sham Operator being

$$h_i^{\mathrm{KS}} = -\frac{1}{2}\nabla_i^2 - \sum_{k}^{\text{nuclei}} \frac{Z_k}{|r_i - r_k|} + \int \frac{\rho(r')}{|r_i - r'|} dr' + V_{\mathrm{xc}} \tag{2.11}$$

and

$$V_{\mathrm{xc}} = \frac{\delta E_{\mathrm{xc}}}{\delta \rho} \ . \tag{2.12}$$

V_{xc} is a functional derivative and describes all contributions to the total energy of the system that we cannot compute in an exact manner. The DFT equations have all been derived in a way that ensures that the energy is in fact exact, but one still has to solve the problem using approximations since the exact form of the XC functional is unknown. Other than this functional, every other term of Eq. 2.10 can be exactly solved. This reduces the problem of solving the DFT equations to finding good approximations for the exchange-correlation, which is the centerpiece of DFT. A select few important XC functionals that have found widespread use in computational chemistry will be discussed in the following.

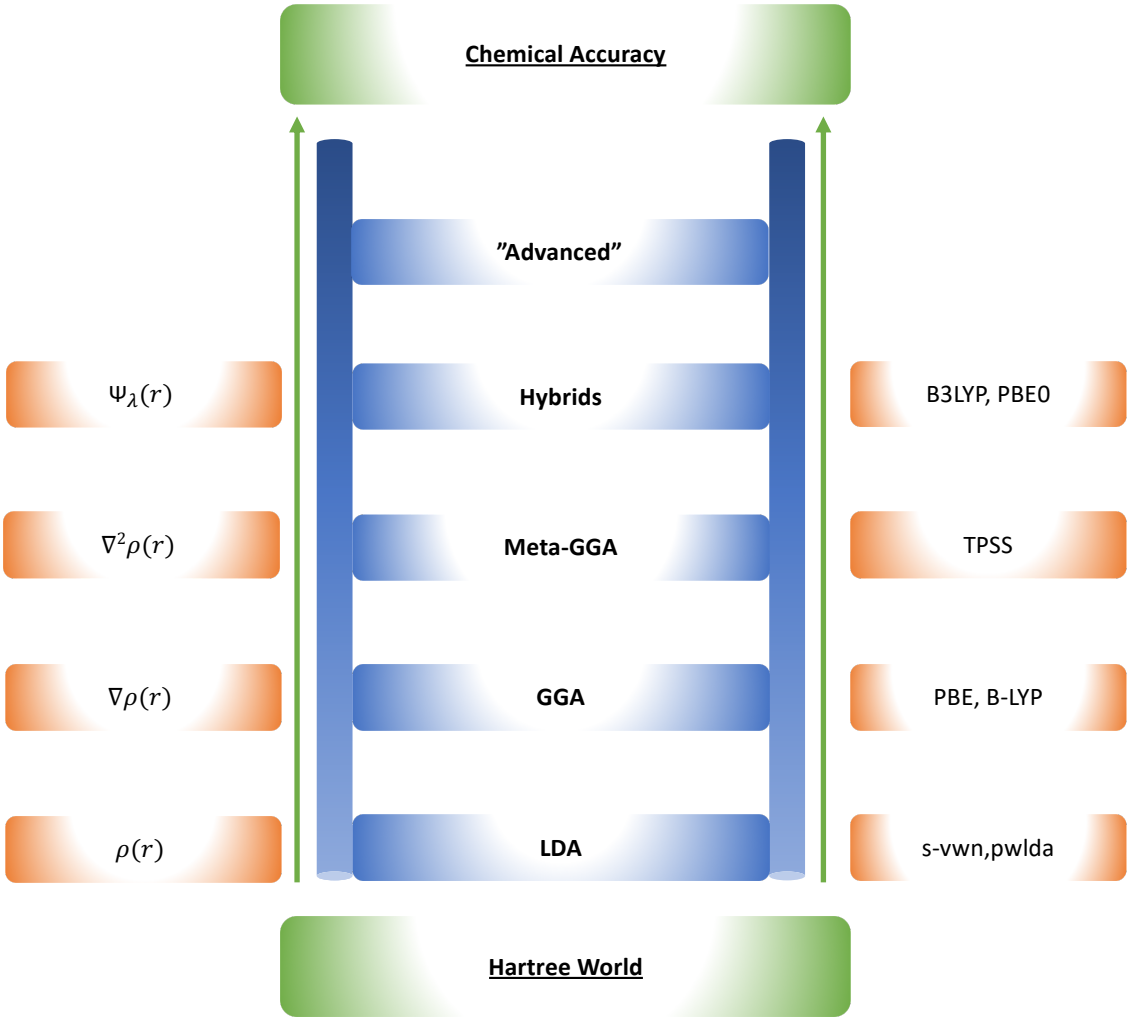

Figure 2.1.: Jacobs ladder, showing the ascension from the "Hartree world" towards high chemical accuracy by means of increasingly sophisticated approaches to describe the Exchange-correlation functional in DFT. Typical functionals of each approximation are given on the right, while on the left, the underlying computational approach is shown.

2.2.3. Exchange-Correlation Functionals

The XC functional contains all contributions to the energy that cannot be exactly solved, which is the electron-electron repulsion and the difference in energy arising from the original Kohn-Sham assumption that the electron-electron repulsion element is zero. This means that it is possible to optimize empirical parameters to this XC term, which is oftentimes done for XC functionals. A first simple approximation to the exchange energy E_x was proposed by Slater in 1951,[48] which is called the Slater exchange:

$$E_\mathrm{x}[\rho(r)] = \frac{9\alpha}{8}\left(\frac{3}{\pi}\right)^{1/3}\int \rho^{4/3}(r)dr \ . \tag{2.13}$$

Slater assumed the factor α to be 1; studies by Bloch[49] and Dirac[50] show higher accuracy of this approximation for $\alpha = \frac{2}{3}$.
Improving on this initial approximation, XC functionals of various complexity and accuracy have been developed. Perdew and Schmidt[51] have described this "ascension" from the low-level accuracy Hartree approximation towards the exact description of the exchange correlation as an ascension on "Jacob´s ladder", which is shown schematically in Fig. 2.1. The lowest rung on this ladder above the Hartree approximation is the simple *Local Density*

Approximation (LDA). In the LDA approach, the XC is described only by the electron density of the system:

$$E_{\mathrm{XC}}^{\mathrm{LDA}}[\rho(r)] = \int \rho(r)\epsilon_{\mathrm{xc}}(r)dr \ , \tag{2.14}$$

where the energy density ϵ_{xc} is treated as the sum of individual exchange and correlation contributions. Comparing Eq. 2.13 with Eq. 2.14, we see that the Slater exchange energy density is given by

$$\epsilon_{\mathrm{xc}}[\rho(r)] = -\frac{9\alpha}{8}\left(\frac{3}{\pi}\right)^{1/3}\rho^{1/3}(r) \ . \tag{2.15}$$

While the LDA approximation to the XC functional is the most basic, it is able to yield fairly accurate results for solids and solid surfaces.[51] Due to its simplicity, it is also used for simple and fast calculations that do not necessarily need high accuracy, like structure optimizations, but is not commonly used for the calculation of molecular properties as e.g. atomization energies can be strongly overestimated. Commonly used LDA XC functionals are the s-vwn[48,52,53] and pwlda[48,52,54] functionals.
On the next rung of the ladder is the *Generalized Gradient Approximation* (GGA), which greatly reduces those errors by adding in the dependency of the XC energy on, as the name already suggests, the gradient of the electron density, as now a non-uniform electron gas is considered. Most GGA functionals add this correction towards the LDA XC functional:

$$E_{\mathrm{XC}}^{\mathrm{GGA}}[\rho(r)] = \int \rho(r)\epsilon_{\mathrm{xc}}\left[\frac{|\nabla\rho(r)|}{\rho^{4/3}(r)}\right]dr \ . \tag{2.16}$$

The most well known GGA functionals are the B-LYP,[48,52,55] B-VWN,[48,52,56] B-P[48,52,56,57] and PBE[36,48,52,54] functionals. These functionals are characterized by their specific parametrization of the correlation contribution. They greatly increase the accuracy in total energies,[58] atomization energies[56,58] and energy barriers[59] in comparison to the LDA approach. In this thesis the PBE functional proposed by Perdew[36] is used for structural optimizations, which does not introduce empirical parameters, but only fundamental constants. It is a very frequently used functional in computational chemistry, as it yields results without too big errors for practically any chemical system.
Two rungs further up Jacob´s ladder are the Hybrid methods, also sometimes called adiabatic connection methods. The idea is to go from the non-interacting KS system (Eq. 2.10) towards the interacting system, using a parameter λ, ranging from 0 to 1, describing the electron-electron interaction:

$$E_{\mathrm{XC}} = \int_0^1 \langle\Psi_\lambda|V_{\mathrm{XC}}(\lambda)|\Psi_\lambda\rangle\, d\lambda \ . \tag{2.17}$$

This is called the *Adiabatic Connection Formula*. The XC energy is then split up into a contribution of the HF exchange energy $E_{\mathrm{X}}^{\mathrm{HF}}$ (which in the case of $\lambda = 0$ is the full contribution), and the DFT XC energy $E_{\mathrm{XC}}^{\mathrm{DFT}}$, which is approximated by the DFT functional of choice. With the parameter a controlling the contribution of both these energy contributions, one arrives at the equation

$$E_{\mathrm{XC}} = (1-a)E_{\mathrm{XC}}^{\mathrm{DFT}} + aE_{\mathrm{X}}^{\mathrm{HF}} \ . \tag{2.18}$$

Some well known hybrid functionals are the B3LYP[48,52,55,56,60] and PBE0[36,48,52,54,61] functionals. They differ by their values for a, as well as the addition of further empirical parameters to improve the XC energies.
One further step towards higher accuracy is done by hybrid meta exchange-correlation

(MHYB) functionals. One of these is the M06 functional,[41] which is highly parametrized and optimized using large molecule databases. The exchange functional part is given by

$$E_{\mathrm{X}}^{\mathrm{M06}} = \sum_{\sigma} \int \left[F_{X\sigma}^{\mathrm{PBE}}(\rho_\sigma, \nabla\rho_\sigma) f(\omega_\sigma) + \epsilon_{X\sigma}^{\mathrm{LSDA}} h_X(x_\sigma, z_\sigma) \right] dr \tag{2.19}$$

with $F_{X\sigma}^{\mathrm{PBE}}(\rho_\sigma, \nabla\rho_\sigma)$ being the PBE exchange energy density, $\epsilon_{X\sigma}^{\mathrm{LSDA}}$ the local spin density approximation for exchange

$$\epsilon_{X\sigma}^{\mathrm{LSDA}} = -\frac{3}{2}\left(\frac{3}{4\pi}\right)^{1/3} \rho_\sigma^{4/3} \tag{2.20}$$

(compare to Eq. 2.15), $f(\omega_\sigma)$ the spin kinetic-energy-density enhancement factor

$$f(\omega_\sigma) = \sum_{i=0}^{m} a_i \omega_\sigma^i \ , \tag{2.21}$$

where

$$\omega_\sigma = (t_\sigma - 1)/(t_\sigma + 1) \quad , \quad t_\sigma = \tau_\sigma^{\mathrm{LSDA}}/\tau_\sigma \quad , \quad \tau_\sigma^{\mathrm{LSDA}} = \frac{3}{10}(6\pi^2)^{2/3}\rho_\sigma^{5/3} \tag{2.22}$$

and $h_X(x_\sigma, z_\sigma)$ a parametrization term. σ denotes the component along an arbitrary space-fixed axis of electron spin angular momentum. As this functional has been shown to yield highly accurate results when used to compute reactions in zeolite catalysis,[40] it is used in this work to calculate high-level correction terms for all systems. It is also important to note here that the M06 functional also intrinsically considers dispersion interactions and have shown to perform very well for systems dominated by dispersion-like interactions.[41]

2.2.4. Self-Consistent Field (SCF) Scheme

One important characteristic of both HF and DFT equations is that they have to be solved iteratively, as in, one needs to converge the energy of a system in an iterative manner. This is done with the Self-Consistent Field (SCF) method, originally proposed by Hartree,[62] which can be used for both HF and KS-DFT equations. They are, in fact, very similar to each other. A flow chart showcasing how the SCF procedure works for DFT is shown in Figure 2.2.

The first step is to choose a basis set, or, as is the case in non-periodic DFT calculations in this work, two basis sets, adding an auxiliary basis set. This auxiliary basis set represents the electron density $\rho(r)$. By making use of this additional basis set, the scaling of the computational cost with the system size is reduced from formal N^4 scaling, as it is in HF calculations, to N^3 scaling, therefore greatly improving performance. For periodic calculations, plane-wave basis sets are used, while for non-periodic calculations, atom-centered basis sets are used, which are discussed in more detail in section 2.3.

After choosing a basis set, the chemical structure is calculated using quantum chemical methods. After calculation of the density matrix $\mathbf{P}^{\mathrm{n}}$, this matrix is compared to the old density matrix $\mathbf{P}^{\mathrm{n}-1}$; if the difference between the matrices is too large (i.e. larger than the set convergence criteria), new KS equations are constructed and the density matrix is recalculated. This is the iterative part of the SCF scheme. After converging the density matrix, which happens when the changes in the matrix lie within the convergence criteria, the calculation is either finished if it was a simple single point calculation, or, in case of a geometry optimization, the molecular geometry is optimized with the converged density matrix. Again, if the new geometry satisfies the set optimization criteria, then the calculation is finished; otherwise, the geometry is changed and the energy of the system is calculated anew.

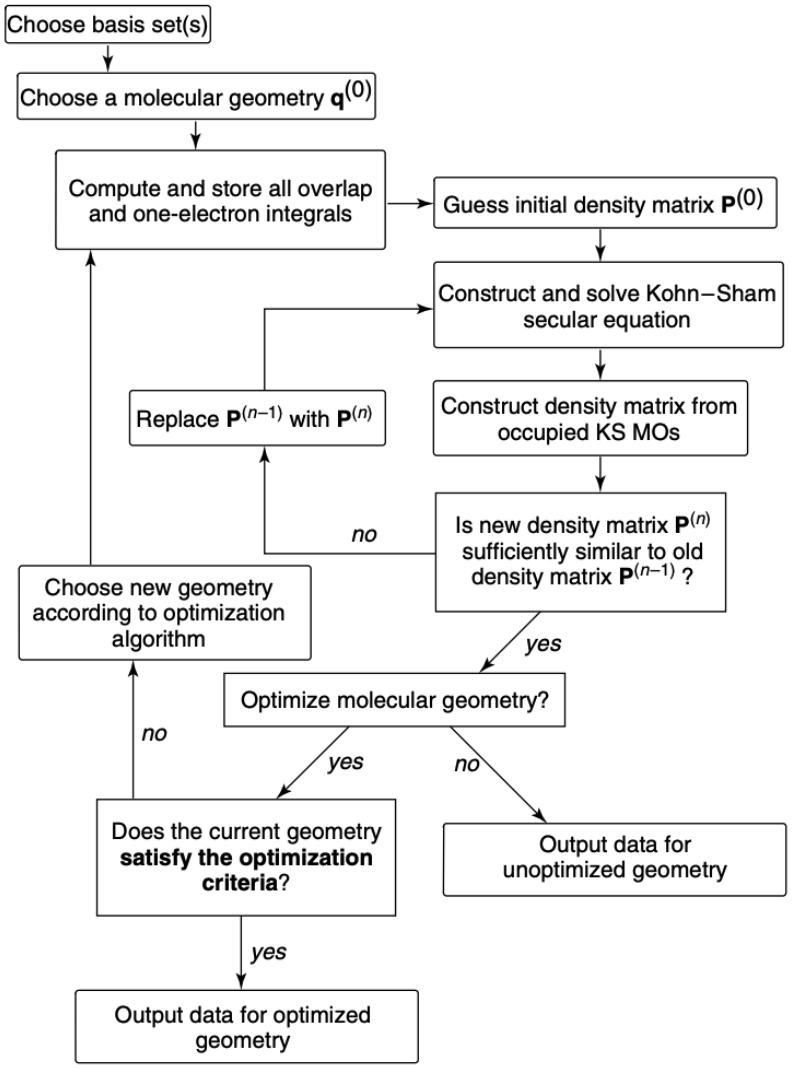

Figure 2.2.: Flow chart showcasing the Kohn-Sham SCF procedure. Reproduced from Ref.[63] with permission from Wiley, copyright 2004.

2.2.5. Dispersion Correction

An important energy contribution to consider when calculating total energies is the *van der Waals* energy contribution E_{vdW}. It is an interaction energy between two molecules or moieties that stems from dipole-dipole interactions. Even non-polar molecules, like alkanes, can create a dipole moment through fluctuations of the electron density. This dipole can then induce a charge distribution in another molecule, leading to an attractive electronic interaction between the two. This interaction of induced dipoles with each other is called dispersion interaction, "London" force, or also "attractive *van der Waals*" force. It is strongly positive for very short distances because of electron repulsion (also known as Pauli repulsion), has a minimum at short distances with atoms being close to each other, and goes to zero for high distances. It can be shown that the interaction energy between induced dipoles depends on the inverse sixth power of the distance r. A well known model of this interaction is the Lennard-Jones potential:

$$E_{\mathrm{LJ}}(r) = \epsilon \left[\left(\frac{r_0}{r} \right)^{12} - 2 \left(\frac{r_0}{r} \right)^{6} \right] \quad . \tag{2.23}$$

Here, ϵ is the depth of the minimum and r_0 is the minimum energy distance. The r^{12} part describes the repulsive interaction and the r^6 part the attractive part of the potential. This

potential is shown schematically in Fig. 2.3 for the interaction of two atoms A and B. r^*_{AB} in the figure represents the minimum energy distance r_0 of Eq. 2.23.

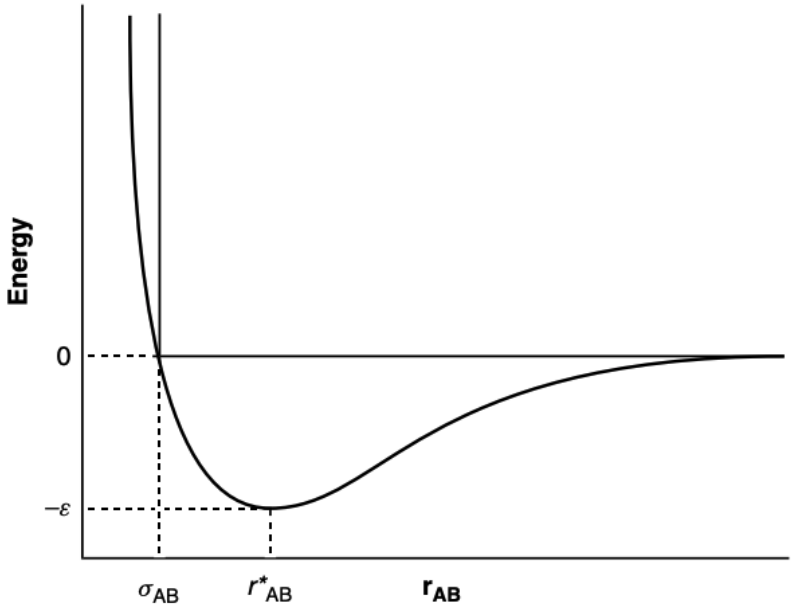

Figure 2.3.: Lennard Jones Potential showing the repulsive interaction between atoms at very short distances and the attractive interaction at short distances, leading to a minimum in the energy at the bond length r^*_{AB}. Reproduced from Ref.[63] with permission from Wiley, copyright 2004.

Dispersion corrections for DFT calculations have been proposed by Grimme et al. at four different levels, ranging from DFT-D1 to DFT-D4,[64–67] and are widely used in computational chemistry to describe the dispersion energy contribution of systems. In this thesis the DFT-D3[66] correction is employed, where the dispersion correction consists of a two-body and a three-body term. The two-body term, which contributes more to the dispersion energy than the three-body term, is given by

$$E^{(2)} = \sum_{AB} \sum_{n=6,8,10,\ldots} s_n \frac{C_n^{AB}}{r_{AB}^n} f_{d,n}(r_{AB}) \ , \tag{2.24}$$

where A and B index atoms, C_n^{AB} describes the n-th order dispersion coefficient for atom pair AB, r_AB is the distance between atoms A and B, and $f_{d,n}(r_{AB})$ are damping factors used to avoid singularities during the calculations. The three-body term is given by

$$E^{(3)} = \sum_{ABC} f_{d,(3)}(\bar{r}_{ABC}) E^{ABC} \ , \tag{2.25}$$

where the geometrically averaged radii $\bar{r}_{ABC}$ are used in the damping function and E^{ABC} are dispersion terms derived from third-order perturbation theory.
As this contribution is fairly cost-effective to calculate and only needs the coordinates of the structure, this calculation is usually amended after the SCF calculation of a system. The D3 energy contribution is then simply added to the total energy of the system.

2.3. Basis Sets

To efficiently solve any HF or DFT equation to calculate the energy of a system, one needs to use basis sets to either describe the one-electron orbitals $\chi(r)$ or the electron probability density $\rho(r)$, see Eq. 2.5, of the system. Basis sets themselves are sets of mathematical

functions. One simple but still accurate choice are the so-called Slater Type Orbitals (STOs) of the form

$$\Phi^{\mathrm{STO}}_{\zeta,n,l,m}(r,\theta,\psi) = N \cdot Y_{l,m}(\theta,\phi) r^{n-1} \exp(-\zeta r) \ . \tag{2.26}$$

Here, N is a normalization constant and $Y_{l.m}$ are spherical harmonic functions. While these types of functions are able to describe the electronic structure rather accurately, they are problematic to use in practice because of their high computational cost stemming from the necessity to solve three- and four-index two-electron integrals which cannot be solved analytically. While there do exist optimized basis sets using STOs,[68] a commonly used alternative to STOs are Gaussian-Type Orbitals (GTOs) which are constructed through Gaussian functions, which are functions with an exponential decay of $\exp(-r^2)$ instead of $\exp(-r)$:

$$\Phi^{\mathrm{pGTO}}_{\zeta,n,l,m}(r,\theta,\psi) = N \cdot Y_{l,m}(\theta,\phi) r^{2n-2-l} \exp(-\zeta r^2) \ . \tag{2.27}$$

While these primitive Gaussian-Type orbitals (pGTOs) are efficient to calculate in practice, one drawback is their form at the nucleus, which is smooth and differentiable, instead of having a cusp at $r = 0$. Also, the functions fall off too quickly for higher distances r because of the increased order of r in the exponential function. An accurate approximation which remedies these drawbacks is the construction of contracted GTOs (cGTOs) through linear combination of multiple pGTOs:

$$\Phi^{\mathrm{cGTO}}(\vec{r}) = \sum_{n=1}^{L} d_n \Phi^{\mathrm{pGTO}}_n \ . \tag{2.28}$$

A number of L pGTOs are contracted to form one cGTO using the contraction coefficient d_n, which can be optimized together with the individual exponents of the pGTOs to minimize errors. A basis set constructed in this way is called segmented contracted. Through this, chemically accurate STOs are approximated through linear combination of computationally efficient GTOs. Such basis sets were first constructed by Pople et al.[69] and were later optimized.[70] They are of the form STO-MG, where M stands for the number of Gaussians used to approximate the STO. More well-known basis sets are the ones optimized by Dunning[71–74] and Jensen.[75,76] Furthermore, there are well-known basis sets which have been developed in Karlsruhe. The def2-TZVP(P) basis set[77,78] is one such basis set and is the one used in this thesis for all calculations. It is a Karlsruhe basis set of triple zeta valence quality, which means that per valence shell, three GTOs are used to describe each element. An additional flat polarization function is also added to increase accuracy for heavier elements, i.e. elements of the fifth group and higher.[79]

2.4. Resolution of the Identity (RI)

For DFT calculations, the computational cost scales with the size of the system, or in other words, with the number of atoms N. Also, the calculation of the integrals during the DFT procedure scales with N^4, which is rather expensive. The N^4 scaling comes from the fact that four-center integrals $(\nu\mu|\kappa\lambda)$ have to be calculated. It is, however, possible to circumvent the N^4 scaling by the introduction of an auxiliary basis set $\phi_P(r)$ that is similar/the same as the regular basis sets. The Coulomb energy of the system is given by the Coulomb operator

$$\hat{J}_{\nu\mu} = \sum_{\kappa\lambda} (\nu\mu|\kappa\lambda) P_{\kappa\lambda} \tag{2.29}$$

with the four-center integral given by

$$(\nu\mu|\kappa\lambda) = \int \phi_\nu(r_1)\phi_\mu(r_1) \frac{1}{r_{12}} \phi_\kappa(r_2)\phi_\lambda(r_2) d^3d_1 d^3r_2 \tag{2.30}$$

and $P_{\kappa\lambda}$ being the density matrix. One can now substitute the products of the basis functions $\phi_\nu(r)$ and $\phi_\mu(r)$ with a single basis function, the auxiliary basis function $\phi_p(r)$, multiplied with a set of coefficients:

$$\phi_\nu(r)\phi_\mu(r) = \sum_\mu c^p_{\nu\mu}\phi_p(r) \ . \tag{2.31}$$

The coefficients are determined through minimization:

$$(\phi_\nu\phi_\mu - \tilde{\phi}_\nu\phi_\mu|\phi_\nu\phi_\mu - \phi_\nu\tilde{\phi}_\mu) = Min \ . \tag{2.32}$$

The idea now is to formally insert a 1, or identity, in the form of some matrices P and Q into Eq. 2.30. This is called the resolution of the identity, or RI in short. This gives us, in analogy to Eq. 2.29, the RI Coulomb operator:

$$J^{\mathrm{RI}}_{\nu\mu} = (\nu\mu|\underbrace{P)(P|Q)^{-1}(Q}_{1}|\kappa\lambda)P_{\kappa\lambda} \ . \tag{2.33}$$

This way, the coloumb operator now consists only of integrals which scale by N^3 at most. While it is not formally a definite reduction of the computational cost by one order of magnitude in N, it is a decrease by about a factor of 10. Therefore, the RI approximation is widely used for DFT calculations.

2.5. Calculation of Periodic Systems

Many systems of interest in quantum chemistry are periodic in nature, like e.g. surfaces, or are for computational convenience modeled as periodic, as it is often done for e.g. nanoparticles. The zeolite structures that are investigated in this thesis are also periodic, as their SiO_4 building stones build up a larger, periodic superstructure, as was shown in Fig. 1.2. As such, these systems cannot be calculated the same way single molecules can be calculated, as the periodicity needs to be taken into account.
First, a unit cell needs to be defined, containing all atoms of the system which represent the full periodic system. The lattice described by this unit cell must be invariant under translation, e.g. the structure repeats indefinitely in all directions. The periodicity of a wave function ψ, which describes an electron in the periodic system, can be modeled by a lattice-periodic factor $u(r)$ and a phase factor e^{ikr}:

$$\psi_k(r) = e^{i\mathbf{k}r}u_k(r) \ , \tag{2.34}$$

where the index $\mathbf{k}$ is a vector; this is called Bloch's theorem.[49] This type of wave function is called a plane wave. Using Bloch's theorem, it is possible to calculate the total energy of a system if $u_\mathbf{k}(r)$ is known by summing, or integrating, over all those k-points in the Brillouin zone (the unit cell in reciprocal space). In practice, k-points are always summed over. The computational costs of the calculation can then be greatly reduced by reducing the number of k-points to sum over. By introducing reciprocal lattice vectors G, $u_\mathbf{k}(r)$ is now expressed in terms of those lattice vectors, and the wave function ψ can in turn be described entirely by plane-waves:

$$\psi_{n,\mathbf{k}}(r) = \sum_G c_{n,k+G}\exp(i(\mathbf{k}+G)r) \ . \tag{2.35}$$

Here, the coefficients $c_{n,k+G}$ can be optimized to approach the lowest energy solution. Similar to the previous chapter, a certain amount of plane-wave functions can now be chosen as the basis set to describe the system. For plane-waves, this is done by truncating the basis set at a certain cut-off energy

$$E_{\mathrm{cut-off}} = \frac{\hbar^2}{2m}|G_{max}|^2 \ . \tag{2.36}$$

In practice, the choices of the cut-off energy is straight-forward, as it is easy to converge it towards a value after which a further increase in cut-off energy causes only minimal changes in the final energy of the system.
An additional way to increase the cost-efficiency in periodic calculations is given by the projector augmented-wave (PAW) method.[80] To properly describe the electronic structure both close to the nucleus and in the bonding region, the wave function is split into two parts, which are a partial-wave expansion for the former and envelope functions for the latter. The envelope functions are expanded into plane waves. The wave functions that describe the core region are transformed into smoother wave functions and can that way be computed more easily.

2.6. The Cluster Model Approach

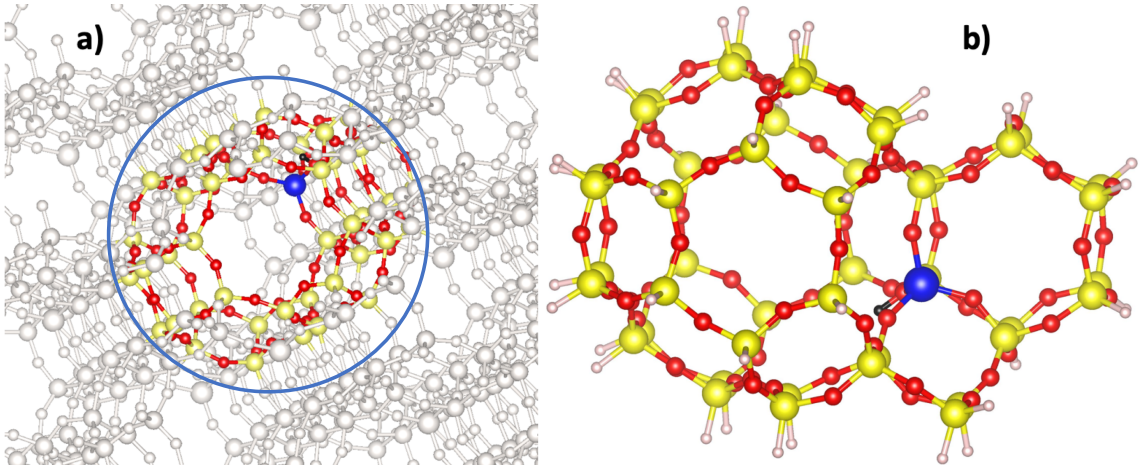

Figure 2.4.: a) Periodic structure of the H-SSZ-13 (chabazite) zeolite with the atoms of the cluster model cut-out out-lined in color. b) 46T Cluster model of H-SSZ-13, saturated with hydrogen. The cluster model retains the pore structure of the zeolite to encompass confinement effects. Coloring: blue - Si, red - O, yellow - Al, black - acidic H, light pink - saturating H.

In computational chemistry, there is always the dilemma of having to trade computational accuracy for higher computational cost. While the calculations of small molecules that do not consist of elements which are computationally difficult to solve can be performed at a very high level of theory, this is unfortunately not the case for any larger system, like for example the zeolite catalysts investigated in this thesis. Usually, somewhat of a middle ground needs to be found between accuracy and cost. However, when taking a closer look at the zeolite catalyst systems at hand, it is clear that the part of the catalyst that is most important for describing a catalytic reaction is only the small part of the periodic structure where the reaction takes place. Most of the atoms in the unit cell are needed to fully describe the periodic superstructure of the zeolite, but do not actually have any significant effect on the catalytic reaction at hand. Hence, the deduction is that it is feasible to only calculate the most important part of the zeolite structure, together with any reactant molecules in it, using a high-level method, while it suffices to describe the rest of the zeolite structure using a lower-level method. As this cannot be done in one single calculation, three separate calculations have to be performed: One calculation of the periodic structure at low level theory; one calculation of the non-periodic reactive center at low level theory; and one calculation of the non-periodic reactive center at high level theory. It is also important to note that the lower level theory that is used in the calculations needs to be the same for both the periodic and the non-periodic structure.
The main challenge here is to find a suitable way to construct a molecule that describes the

reactive center of the periodic zeolite. This is done by the construction of so-called cluster models, originally proposed by Sauer and coworkers who introduced this as a method between the low-level DFT and high-level MP2 methods.[81–85] In this thesis, the M06 functional together with the def2-TZVPP basis set will instead be used as the high-level method. The cluster models were cut from the periodic structure in a way that ensures that the vicinity around the reaction center is very well described. As the cluster model is non-periodic, the cluster model needs to be terminated at some point; this is done by substituting all non-oxygen atoms that are on the outside of the cluster model by terminating H-atoms (see Fig. 2.4 and also 2.8). A cluster model with a number of N tetrahedral atoms, or in short T atoms, is called a NT cluster model. Figure 2.4, as an example, showcases both the a) periodic structure, with the cluster model that is later cut out shown in the blue circle, and b) 46T cluster model of the H-SSZ-13 (CHA) zeolite that is used in this thesis.
Considering these structures, we arrive at Eq. 2.37, which gives the cluster model (CM) corrected energy of the systems:

$$E = E^{\mathrm{PBC}}_{\mathrm{PBE-D3}} + E^{\mathrm{CM}}_{\mathrm{M06/def2-TZVPP}} - E^{\mathrm{CM}}_{\mathrm{PBE-D3/def2-TZVPP}} \ . \tag{2.37}$$

Using this cluster model method, the enthalpy contributions of the free energies calculated in this thesis are expected to be within chemical accuracy, which means an error of $\leq$1 kcal/mol or $\leq$4 kJ/mol.

2.7. Thermodynamics

Calculating the electronic energy of a chemical system with the methods described above does not yet give the enthalpy $\Delta H^{\dagger}$, which is a thermodynamic variable. To obtain H starting from the potential energy, and to subsequently obtain the free energy G, some thermochemical contributions need to be considered for H, as well as the entropy S of the system at a given temperature, seeing as the electronic energy E_{elec} is only calculated for a system at 0 K. It is therefore also important to take entropic effects into account, which can have a huge impact on the relative reactivity of a system. The ideal gas approximation is employed for calculating these contributions, and an overview of how they are calculated is given here.
The free energy G and the enthalpy H of a system are given by the fundamental thermodynamic relations

$$\Delta G = \Delta H - T\Delta S \tag{2.38}$$

and

$$\Delta H = \Delta U + P\Delta V \ , \tag{2.39}$$

where T is the temperature, P is the pressure and U is the internal energy. Following statistical mechanics, U and S can be defined by a partition function Q:

$$U = k_B T^2 \left(\frac{\delta lnQ}{\delta T}\right)_{N,V} \tag{2.40}$$

$$S = k_B T lnQ + k_B T \left(\frac{\delta lnQ}{\delta T}\right)_{N,V} \ . \tag{2.41}$$

In the ideal gas approximation, the energy components of the partition function Q become separable, so that the problem of finding the partition function Q can be reduced to

the problem of finding its components, namely translational, rotational, vibrational and electronic contributions:

$$Q = q_{\text{trans}}\, q_{\text{rot}}\, q_{\text{vib}}\, q_{\text{elec}} \ . \tag{2.42}$$

Similarly, the entropy of a system also consists of these four different contributions:

$$S_{\text{tot}} = S_{\text{trans}} + S_{\text{rot}} + S_{\text{vib}} + S_{\text{elec}} \ . \tag{2.43}$$

The derivation of all these terms will be omitted here due to simplicity, and the individual terms are only discussed briefly.
First, the translational partition function is given by

$$q_{\text{trans}} = \left(\frac{2\pi M k_B T}{h^2}\right)^{3/2} V \tag{2.44}$$

and the translational entropy contribution by

$$S_{\text{trans}} = \frac{5}{2}R + Rln\left(\frac{k_B T}{P}\left(\frac{2\pi M k_B T}{h^2}\right)^{3/2}\right) \ , \tag{2.45}$$

where M is the total molecular mass and only molecular parameter in both cases, which means that the translational contributions can easily be computed just knowing this value. Also, as q_{trans} and S_{trans} are the only functions depending on the volume V (the $\frac{k_B T}{P}$ term in Eq. 2.45 can be replaced by $\frac{V}{N_A}$ in the ideal gas approximation), the volume is fixed to the standard volume $V^0 = 24.5$ L, which is the volume that 1 mol of an ideal gas occupies at at pressure of 1 atm.
The rotational contributions can be derived by making use of the rigid-rotor approximation. The rotational partition function is given by

$$q_{\text{rot}} = \frac{\sqrt{\pi}}{\sigma}\left(\frac{8\pi^2 k_B T}{h^2}\right)^{3/2}\sqrt{I_x I_y I_z} \tag{2.46}$$

and the rotational entropy contribution by

$$S_{\text{rot}} = 0 \quad , \quad \text{if monoatomic} \tag{2.47}$$

$$S_{\text{rot}} = R\left[1 + ln\left(\frac{8\pi^2 I k_B T}{\sigma h^2}\right)\right] \quad , \quad \text{if linear} \tag{2.48}$$

$$S_{\text{rot}} = \frac{1}{2}R\left[3 + ln\left(\frac{\sqrt{\pi}}{\sigma}\left(\frac{8\pi^2 k_B T}{h^2}\right)^{3/2}\sqrt{I_x I_y I_z}\right)\right] \quad , \quad \text{if nonlinear} \tag{2.49}$$

where σ is a symmetry index, given by the molecular point group of chemical group theory, and $I_{x,y,z}$ are the three moments of inertia, which are derived from the molecular structure. Thus, the geometry and symmetry of a molecule is important for calculating the rotational contributions to enthalpy and entropy.
The vibrational contribution functions are derived assuming that the full vibrational energy can be expressed as a sum of contributions of each vibrational mode, and by approximating each of those vibrational modes as a harmonic oscillator. Doing so, the vibrational partition function is found to be

$$q_{\text{vib}} = \prod_{i=1}^{3N-6}\left(\frac{1}{1 - \exp(-h\omega_i/k_B T)}\right) \tag{2.50}$$

and the vibrational entropy contribution is

$$S_{\text{vib}} = R \sum_{i=1}^{3N-6} \left[\frac{h\omega_i}{k_B T(\exp(h\omega_i/k_B T) - 1)} - ln(1 - \exp(-h\omega_i/k_B T)) \right] \ , \tag{2.51}$$

where ω is the vibrational frequency. These contributions are for the case of a non-linear molecule; in the case of a linear molecule, the indices of the product in Eq. 2.50 and the sum in Eq. 2.51 only range to $3N - 5$. To calculate these values, it is necessary to first calculate the needed vibrational frequencies of the structure.
The electronic contributions are the easiest to compute. In a common convention, the ground state for each energy component is defined to be zero; thus, the electronic partition function is simply given by

$$q_{\text{elec}} = 1 \tag{2.52}$$

and the electronic entropy contribution by

$$S_{\text{elec}} = Rln(2s + 1) \ , \tag{2.53}$$

where s stands for the spin of the system.
After calculating S_{tot} (Eq. 2.43) and Q (Eq. 2.42) through all these contributions, the ideal-gas Gibbs free energy can then be computed by means of Eq. 2.38.

2.8. Transition State Search

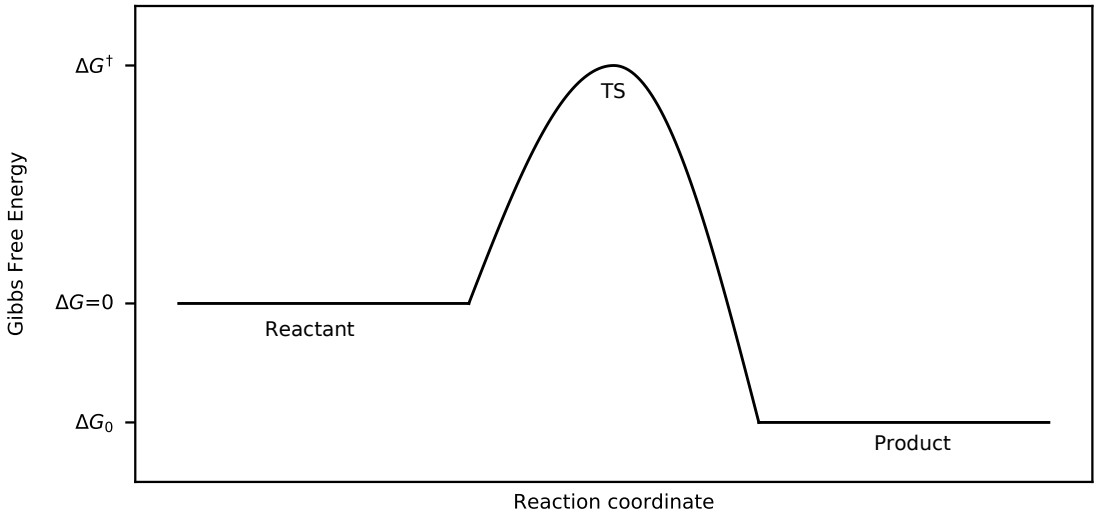

Figure 2.5.: Schematic illustration of a reaction path along the reaction coordinate, going from the initial state (IS) over the transition state (TS) to the final state (FS).

When optimizing reaction pathways for chemical reactions, stable intermediate structures as well as a transition state (TS) that links two intermediate structures together, have to be optimized. In transition state theory (TST), a chemical reaction is modeled to proceed via a reaction coordinate, which leads from the initial state (IS) to the final state (FS) geometry of the system along the minimum energy path (MEP). The IS and FS on this so-called potential energy surface are minima, and the TS is in a minimum in all coordinates except the reaction coordinate, where it is in a maximum. This point then is a first-order saddle point; a visual representation of these structures along a reaction coordinate is given in Fig. 2.5. It is possible to confirm these states by calculating the harmonic frequencies of

the structures (which are also used to calculate vibrational contributions, see Eq. 2.50 and Eq. 2.51) using a partial Hessian. The IS and FS structures must have no imaginary frequencies, and the TS must have exactly one.
To find and optimize the TS structure one is looking for, several tools are available in quantum chemical programs and in the literature. In this thesis, mainly two of those methods were used to optimize TS structures, and are discussed here briefly. The first is the *Automated Relaxed Potential Energy Surface Scan* (ARPESS).[86] Here, linear combinations of bond lengths are used to optimize the TS geometry. While some information or chemical intuition about how the final TS will look like is needed, it is a useful tool to optimize and also re-optimize transition states in e.g. zeolite catalysis. As the transition states found in this work were first optimized in the H-SSZ-13 zeolite and subsequently simply transferred to different zeolite structures and there re-optimized, this was the method of choice for almost all transition states.
Fig. 2.6 shows a simple example for one of these optimizations: In this TS, the hydrogen

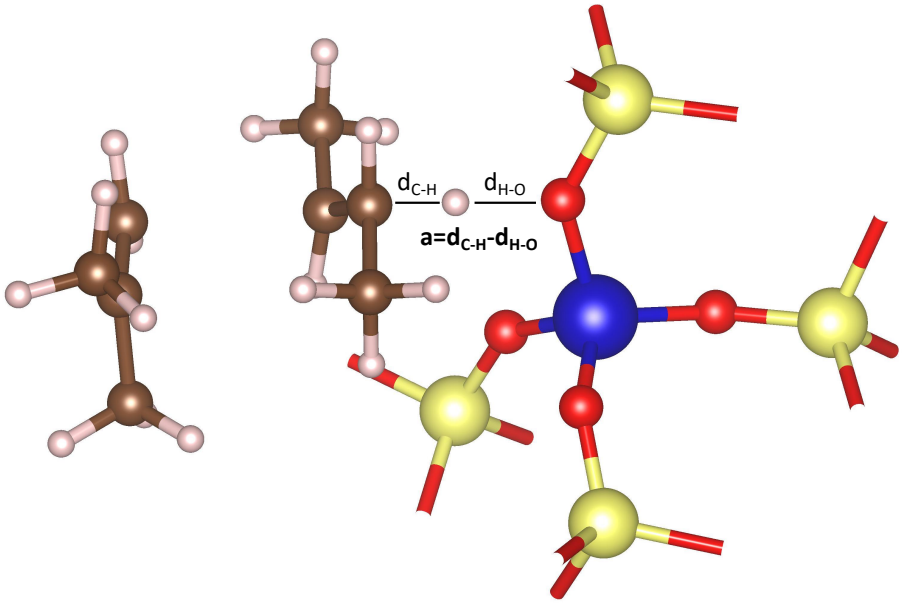

Figure 2.6.: Image of a transition state calculated in this work (see chapter 3) using the ARPESS program. The bond distances d_{C-H} and d_{H-O} were used together in a constrained linear combination to optimize the transition state.

atom in the middle (in light pink) is transferred from an oxygen atom (in red, to the right) to a carbon atom (in brown, to the left). In the optimized TS structure, the H atom is almost exactly in the middle between the oxygen and the carbon, as one would expect. Therefore, to optimize the transition state, putting the H atom between the C and O atoms, with equal distances to them, served as a very good initial guess for the transition state. The bond lengths d_{C-H} and d_{H-O} were then chosen in the constrained optimization of the linear combination $a = d_{C-H} - d_{H-O}$.
The second method used here is the *Nudged Elastic Band* (NEB) method.[87–91] This method requires no prior knowledge of the transition state, as it requires only the optimized initial and final states, which it will then (in its simplest form) simply connect by optimizing the MEP between the two.

2.9. Calculation of Gibbs Free Energies and Reaction Barriers

Utilizing the equations and tools which have been presented up until now, Gibbs free energy barriers can be calculated by optimizing the geometries of the IS, TS and FS of the

reactions and afterwards performing energy and entropy calculations (the entropy within the harmonic approximation). Geometry optimizations and energy calculations of periodic structures have been performed with the VASP program package[92–96] in version 5.4.1 using the atomic simulation environment (ASE) Python library as a facilitator,[97] at the PBE-D3 level of theory.[36,66] The projector augmented wave (PAW) method was used with standard PAW potentials and an energy cutoff of 400 eV for the wave function and an SCF energy convergence criterium of 10^{-8} eV and a geometry convergence criterium of 10^{-2} eV/Å. The Brillouin zone was sampled only at the Γ-Point. Transition state optimization was performed for most of the transition states with the ARPESS script.[86] For transition states that could not be easily optimized this way, NEB[87–91] calculations were performed instead. As both the CHA and the AFI zeolite have only one distinguishable T-site, the choice of T-site for the substitution with another atom to create an acid site is arbitrary. For the MOR zeolite, the T4 site is chosen, as is commonly done in literature.[98] As in each zeolite there are four different oxygen sites that the acid proton can occupy, it has been ensured that for all structures the energetically most favorable structure or transition state is chosen. Harmonic frequencies were computed based on a partial Hessian, where the adsorbate as well as the acid site (Al) and its four neighboring oxygen and silicon atoms are included. All stationary states were confirmed to contain the correct amount of imaginary harmonic frequencies, i.e. zero for minima and one for transition states. Entropy contributions at the given temperature were calculated using the harmonic approximation, where all frequencies under a threshold of 12 cm^{-1} are treated as 12 cm^{-1} to avoid inaccuracies in the entropy for low frequency vibrations.[45,99]
To improve the accuracy of the periodic energies at the PBE-D3 level, which widely underestimates barriers in zeolite catalysis,[40] smaller non-periodic cluster models were constructed, as described in section 2.6, for which then single point calculation were performed using the Turbomole program package.[100,101] For the cluster models, calculations employing both the D3-corrected PBE-D3 functional[36–38] as well as the M06 functional[41] were performed with the def2-TZVPP basis set.[77,78] The final energy E of a structure is accordingly given by Eq. 2.37. Free energies were calculated within the harmonic oscillator approximation at T=400 °C and p=1 bar.

2.10. Structural Details of the Investigated Zeolites

2.10.1. Periodic structures

The H-SSZ-13 zeolite in the chabazite structure has been chosen as the model catalyst due to its simplicity with only one possible T-site for Al substitution. The H-SSZ-13 zeolite with CHA structure has a narrow pore window size of 0.38 x 0.38 nm.[102] A CHA unit cell containing 36 T-sites has been chosen for this thesis. The optimized periodic CHA structure has lattice parameters of a = b = 13.625 Å, c = 15.067 Å, $\alpha = \beta = 90°, \gamma = 120°$ and V = 2422.314 $Å^3$. For the clean acid site, the hydrogen atom is bound to the crystallographic O4 position. As CHA has only one distinguishable T-site, substitution of one out of the 36 Si atoms in the unit cell with Al and compensating the charge with an acidic H atom leads to the structure shown in Fig. 2.7a with a Si/Al ratio of 35.
The H-SAPO-34 zeolite as well as its substituted AlPO-34 derivatives (Mg, Co, Zn) that are investigated in this work have the lattice parameters a = b = 13.875 Å, c = 15.017 Å, $\alpha = \beta = 90°, \gamma = 120°$ and V = 2503.686 $Å^3$. The H-SAPO-34 structure was obtained by substituting all Si atoms in the unit cell with alternating Al and P atoms, and substituting the Al acid site atom with Si, which is in the H-SAPO-34 structure substituting a P atom, resulting in a (Al+P)/Si ratio of 35. The periodic structure of the H-SAPO-34 framework is shown in figure 2.7b. The acid proton stays at the crystallographic O4 position for the clean acid site.
The substituted H-MAlPO-34 structures are then obtained by substituting the Si atom with

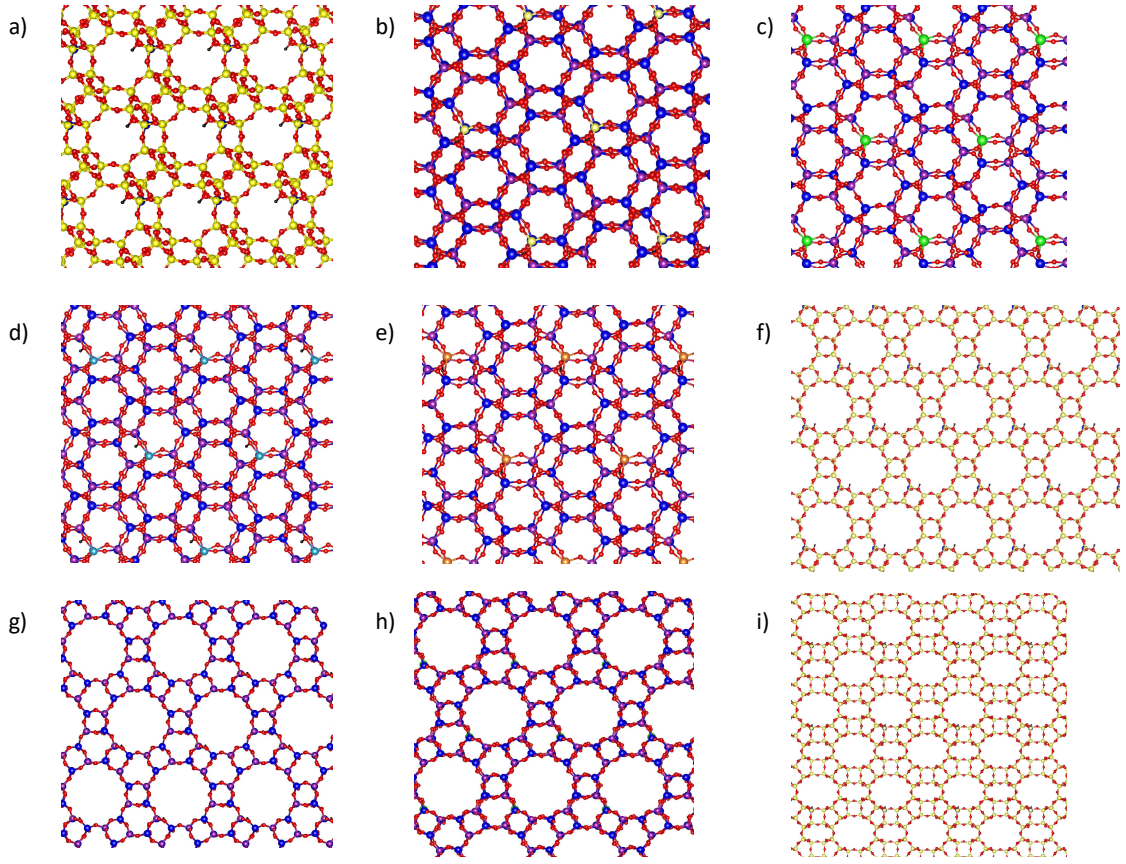

Figure 2.7.: Periodic structures of the zeolites investigated in this work. a) H-SSZ13, b) H-SAPO-34, c) H-MgAlPO-34, d) H-CoAlPO-34, e) H-ZnAlPO-34, f) H-SSZ-24, g) H-SAPO-5, h) H-MgAlPO-5 and i) H-MOR. Coloring: Si - yellow, Al - blue, O - red, acidic H - black, P - purple, Mg - green, Co - turquoise, Zn - orange.

either M=Mg, M=Co or M=Zn. Figures 2.7c, 2.7d and 2.7e show the periodic structures of the substituted H-MAlPO-5 zeolites, respectively. Because of the charge difference between Si_4^+ and M_2^+, M has to substitute Al_3^+ instead of P_5^+. This is achieved by simply interchanging all Al and P atoms of the unit cell. These structures all have a (Al+P)/M ratio of 35. For H-MgAlPO-34 and H-ZnAlPO-34, the acid site proton is also at the crystallographic O4 site; for H-CoAlPO-34 it is at the O1 site.

AFI has a unidimensional 12-ring channel structure (7.3 Å x 7.3 Å). Since AFI has a channel structure, the choice to be made is how many layers of atoms along the axis of the channel are to be used for the unit cell, as there is a need for a sufficient number of layers to negate possible influences of periodic images. This means that any periodic atoms should be at least 11 to 12 Å apart from each other. Here, a 48T unit cell was chosen for the periodic AFI zeolite structure, consisting of four layers of atoms in the x-y plain. Repeating this periodic image along the z-axis shows an Al-Al distance between periodically repeated atoms along the z-axis of 17.2 Å. The H-SSZ-24 unit cell lattice parameters are a = b = 13.886 Å, c = 17.211 Å, $\alpha = \beta = 90°, \gamma = 120°$ and V = 2874.219 Å^3. Figure 2.7f shows the periodic structure of the H-SSZ-24 zeolite. The H-SSZ-24 unit cell has a Si/Al ratio of 46. The acid proton is bound at the crystallographic O1 position for the clean acid site.

The substituted structures H-SAPO-5 and H-MgAlPO-5 were constructed analogous to the CHA structures above; they have lattice parameters of a = b = 13.836 Å, c = 16.832 Å, $\alpha = \beta = 90°, \gamma = 120°$ and V = 2801.361 Å^3 and an (Al+P)/Si and (Al+P)/Mg ratio of 46, respectively. An illustration of the chemical structure of those two zeotypes is shown in

Fig. 2.7g and 2.7h, respectively.
In Fig. 2.7i, the periodic structure of the MOR zeolite is shown. Similar to AFI, MOR has 12-membered rings forming the main channels of the structure. MOR additionally has smaller 8-ring side pockets that connect to the 12-rings. Similar to AFI, it has been made sure that periodic atoms in the MOR unit cell are sufficiently far distanced at 15.1 Å. The resulting unit cell contains 96 T-sites; the substitution of one Si T-site with Al leads to a Si/Al ratio of 95. There are four different T-sites available for this substitution; following the investigation of Brändle and Sauer,[103] the T4 position is chosen for the substitution as it is the most stable. They found, however, the energetic difference between the most stable (T4) and the least stable (T3) substitution to be very low at 4.4 kJ/mol. The naming convention of the T-sites is adapted from Alberti et al.[98] The MOR unit cell has lattice parameters of a = 18.256 Å, b = 20.534 Å, c = 15.084 Å, $\alpha = \beta = \gamma = 90°$ and V = 5654.520 Å^3.

2.10.2. Cluster Models

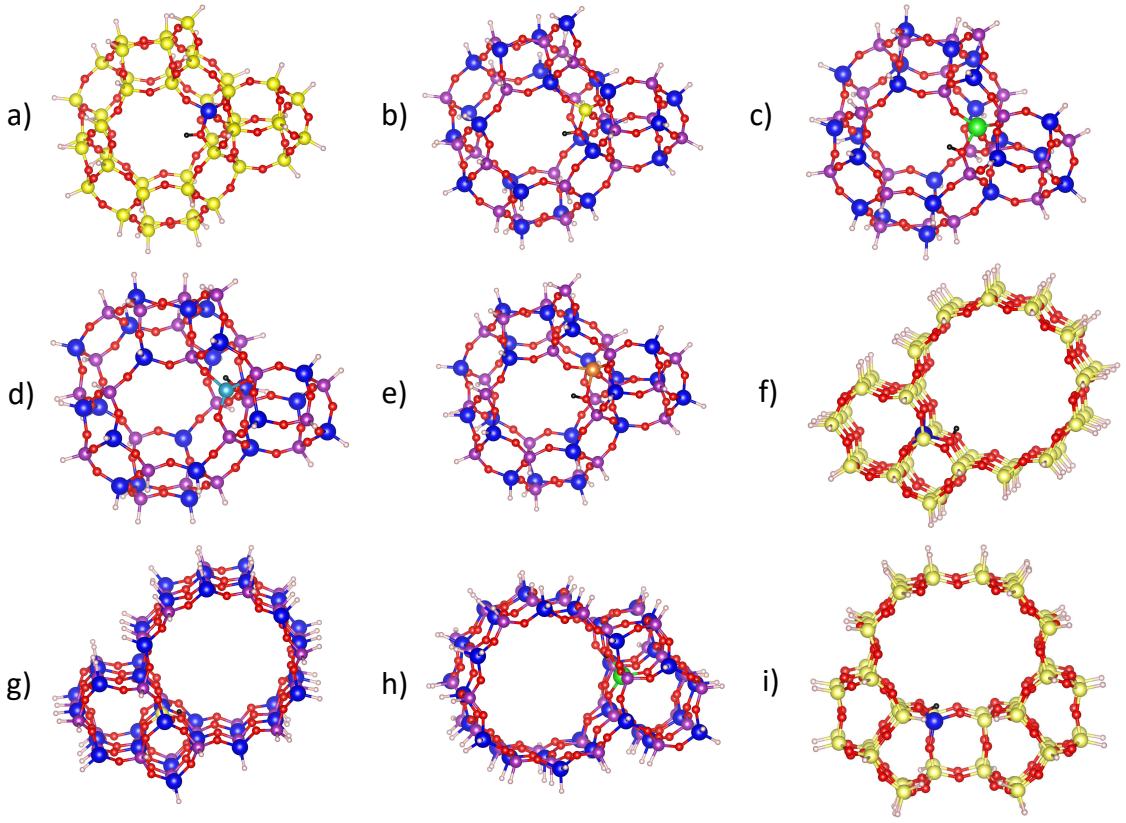

Figure 2.8.: Cluster model structures of the zeolites investigated in this work. a) H-SSZ13, b) H-SAPO-34, c) H-MgAlPO-34, d) H-CoAlPO-34, e) H-ZnAlPO-34, f) H-SSZ-24, g) H-SAPO-5, h) H-MgAlPO-5 and i) H-MOR. Coloring: Si - yellow, Al - blue, O - red, acidic H - black, terminating H - light pink, P - purple, Mg - green, Co - turquoise, Zn - orange.

Fig. 2.8 shows the structures of the cluster models that have been cut for the CHA, AFI and MOR zeolites. From Fig. 2.8a to 2.8i, the depicted cluster models are: H-SSZ-13, H-SAPO-34, H-MgAlPO-34, H-CoAlPO-34, H-ZnAlPO-34, H-SSZ-24, H-SAPO-5, H-MgAlPO-5 and H-MOR. For all CHA frameworks the cluster model is a 46T model and for both AFI and MOR frameworks it is a 68T model. All cluster models were constructed following the general rule that it should be as large as necessary and as small as possible. This ensures that while preserving high accuracy of the calculations, the computational cost is

Table 2.1.: Calculated adsorption energies of the co-adsorption of two 2-butene molecules in AFI H-SSZ-24 at different levels of theory.

B1 ads. energy [kJ/mol]	three layers	four layers	five layers
PBE-D3	-138.0	-142.7	-140.9
M06	-107.5	-105.7	-103.8

kept to a minimum. In all cluster models, it has been made sure that any terminating H must be at least four connecting atoms away from the acid site, ensuring that the chemical environment around the acid site is well described.
For the CHA cluster model, the pore structure of the zeolite needs to be preserved. Additionally, the small side chambers next to the main pore is preserved as well.
A similar consideration to the periodic unit cell size was needed for the size of the AFI and MOR cluster models. For AFI, 4 layers of atoms in the x-y plain were calculated to be the optimal choice. For this, the adsorption of two 2-butene molecules in H-SSZ-24 (structure B1, black line in Fig. 3.6 of chapter 3) was calculated for three cluster models consisting of 3, 4 and 5 layers of atoms, at the M06 level of theory. Results of the calculations are shown in Table 2.1. The difference in energies between 4 and 5 layers is not large enough to warrant the increase in computational cost, so the 4-layer cluster model was chosen for all calculations, shown for H-SSZ-24 in Fig. 2.8f.

For MOR, the same principles have been followed in constructing the cluster model. Here, also a 68T cluster model was chosen, which is shown in Fig. 2.8i. The main 12-ring channel as well as the 8-ring side channel are well described in the 68T cluster model. While a larger cluster model is not feasible due to increased computational costs, any smaller cluster models that were constructed showed immense convergence problems for the M06 cluster calculations and were therefore disregarded as possible cluster model sizes.

3. Butene Isomerization

The results presented in the following chapters are based on Ref.,[104] as well as the publications either currently submitted or still in preparation that are listed in the list of publications, as well as given as a footnote in chapter 1.6.

In this chapter, the reaction mechanism of both the monomolecular and the bimolecular butene isomerization reactions are investigated. The monomolecular mechanism is first calculated in the H-SSZ-13 zeolite, starting from a mechanism by He et al. who have calculated a reaction pathway in the H-ZSM-23 and H-ZSM-48 zeolites.[34] The isomerization barrier of 1-butene to 2-butene in H-SSZ-13 is shown to underline that both olefins can act as reactants for the isomerization reaction. The reaction mechanisms are then transferred to and optimized in a variety of other zeolites, which include four other CHA zeotypes, three different AFI structures, and the MOR zeolite. The differences in reactivities of this set of zeolite structures is discussed in detail, as well as how these depend on the acidity and confinement effects of the zeolites. The same procedure is followed for the bimolecular mechanism, which is calculated for all investigated zeolites. The focus in this study lies in the formation of isobutene; therefore, only the reaction that produces isobutene as a product is investigated in detail. Lastly, the reaction barriers for the two mechanisms are compared to each other to identify which mechanism is predominant for which zeolite framework and/or acid site substitution for butene isomerization. For this, the zeolite acidity and topology, as well as entropic effects and the computational accuracy thereof are considered in the discussion.

3.1. Monomolecular Butene Isomerization

3.1.1. H-SSZ-13

For the calculations performed here, a temperature of 400 °C has been chosen, as it is representative for general reaction conditions in butane isomerization, even though it lies towards the upper end of temperatures used for this reaction.[18,25,29,34,105]
Using olefins as the reactive species, the outcome of our calculations for the monomolecular isomerization reaction of 2-butene to isobutene will be discussed along the lines discussed in the literature. The monomolecular pathway (also called unimolecular pathway) was investigated in H-SSZ-13 based on the transition state geometries reported by He et al.,[34] who have investigated the reactions over H-ZSM-23 and H-ZSM-48 zeolites using the combined B3LYP:UFF method ONIOM scheme. The related reaction mechanism is shown in Fig. 3.1, together with slightly different reaction pathways that were optimized for other zeotypes. In principle, 1-butene could also act as a reactant, as the isomerization between 1-butene (A1) and 2-butene (A2) is facile in the zeolite. This barrier TS(A1-A2) was calculated to be 129 kJ/mol at 400 °C for H-SSZ-13, as can also be seen in Table A.1 in the appendix. Therefore, the choice of reactant is arbitrary, and the focus was put specifically on 2-butene as the reactant for now.

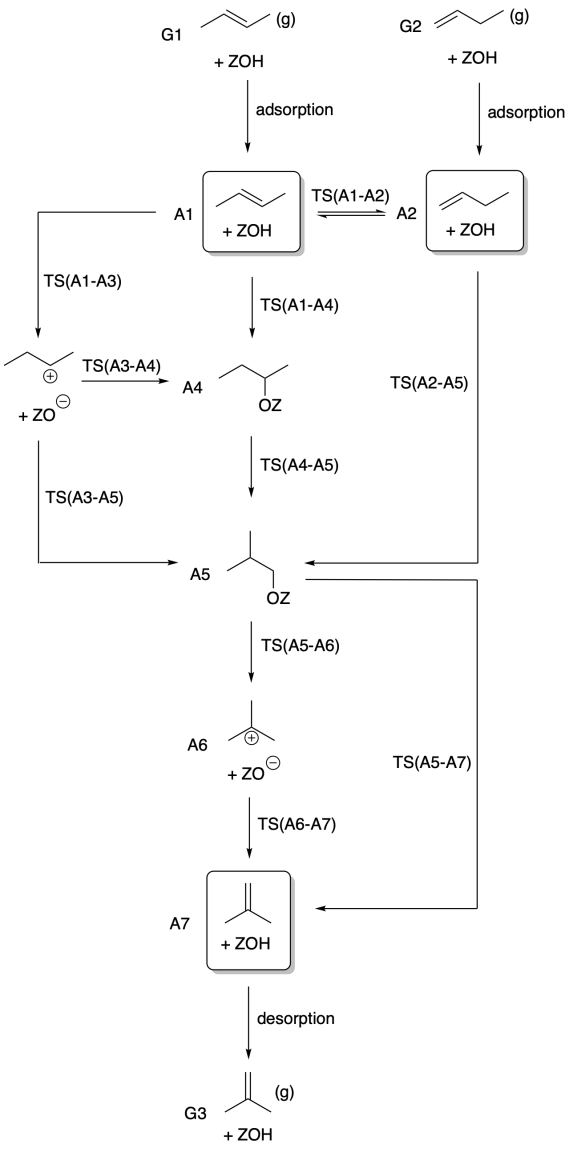

Figure 3.1.: Overview of the monomolecular isomerization mechanisms, referenced to the empty zeolite and either 1-butene or 2-butene in the gas phase. There have been different isomerization mechanisms calculated, depending on whether or not the n-butoxide (A4) is an intermediate of the pathway. The reactants and products are highlighted with boxes.

The reaction pathway proposed by He et al. shows that 1-butene (A1) is protonated by the acid site proton and immediately forms n-butoxide (A4). n-Butoxide then isomerizes to iso-butoxide (A5), passing through a cyclopropyl transition state. The calculations in this chapter indicate that the 2-butylcation (A3) that can form after the protonation is also local minimum. This reaction pathway is similar to the one proposed by He et al., albeit with the difference that 2-butene is the reactant, while He et al. started from 1-butene. As the double-bond migration in 1-butene is much faster than the skeletal isomerization reactions,[32] this does not affect the findings presented here. However, the barriers for decomposition of this cation towards 2-butene or isobutoxide are very low (6 and 3 kJ/mol, respectively), making it an unstable intermediate. The 2-butyl cation isomerizes through a structurally very similar cyclopropyl transition state to form isobutoxide (A5), see Table 3.1. Only the C2-C3 bond distance differs by a few pm, the other C-C bond distances are practically the same. The angles of the cyclopropyl ring are also very similar; for TS(A3-A5) and TS(A4-A5) they are 46.9°, 63.9°, 69.2° and 46.1°, 61.7°, 72.2°, respectively. As can be seen in Fig 3.2, the TS(A3-A5) and TS(A4-A5) transition states only differ in the orienta-

Table 3.1.: Key bond lengths, comparing the TS(A3-A5) transition state with the TS(A4-A5) transition state in H-SSZ-13, given in pm. The numbering of the carbon atoms is shown in Fig. 3.2.

	TS(A3-A5)	TS(A4-A5)
C1-C2	173	172
C1-C3	140	140
C2-C3	180	186

tion of the cyclopropyl ring in the zeolite pore. Depending on how this cationic structure is positioned, isobutoxide is able to isomerize towards either n-butoxide or the 2-butyl cation.

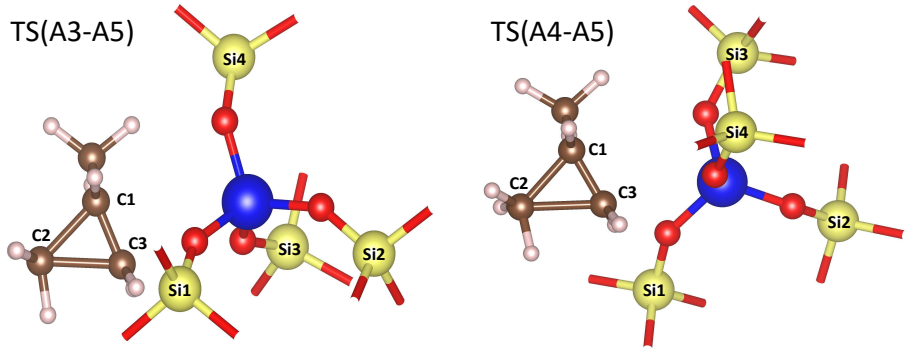

Figure 3.2.: Structures of the TS(A3-A5) and TS(A4-A5) transition states in H-SSZ-13. The cyclopropyl ring on the left is oriented the same way in both structures; the Si atoms of the zeolite framework on the right are numbered to illustrate the different orientation of the TS in the pore. The bond distances of the carbon atoms of the cyclopropyl ring are given in Table 3.1. Coloring: yellow: Si, red: O, blue: Al, white: H, brown: C.

The bond distances calculated for the n-butoxide pathway in H-ZSM-23 and H-ZSM-48 by by He et al.[34] also show very little deviations from the bond lengths calculated here. This is also true for the following two transition state structures, TS(A5-A6) and TS(A6-A7). In these two steps, the C-O bond of the isobutoxide is broken; the proton from the adjacent carbon then shifts over to yield the stable tertiary isobutyl cation (A6). In the final step, the acid site abstracts a proton from the cation and isobutene (A7) is formed. Isobutene can then desorb from the pore into the gas phase, leaving the clean zeolite behind (G3).

The free energy barriers for the monomolecular butene isomerization have been calculated and are shown in the free energy diagram in Fig. 3.3a. The calculated pathway via the stable 2-butyl cation has a free energy barrier of 87 kJ/mol to go from 2-butene to isobutoxide, which is 39 kJ/mol lower than that of the previously considered mechanism over n-butoxide, which was also re-optimized here in H-SSZ-13. The rate determining step for the n-butoxide pathway is the isomerization of n-butoxide to isobutoxide at 181 kJ/mol (shown in gray), while for the 2-butylcation pathway it is the reaction of isobutoxide to the isobutyl cation at 152 kJ/mol. This results in an overall difference in barriers of 29 kJ/mol. When referencing all energies and barriers to the clean H-SSZ-13 zeolite and 2-butene in the gas phase, an overall reaction barrier of only 152 kJ/mol is obtained at 400 °C (see Fig. 3.3a and Table 3.2) for the considered monomolecular mechanism.

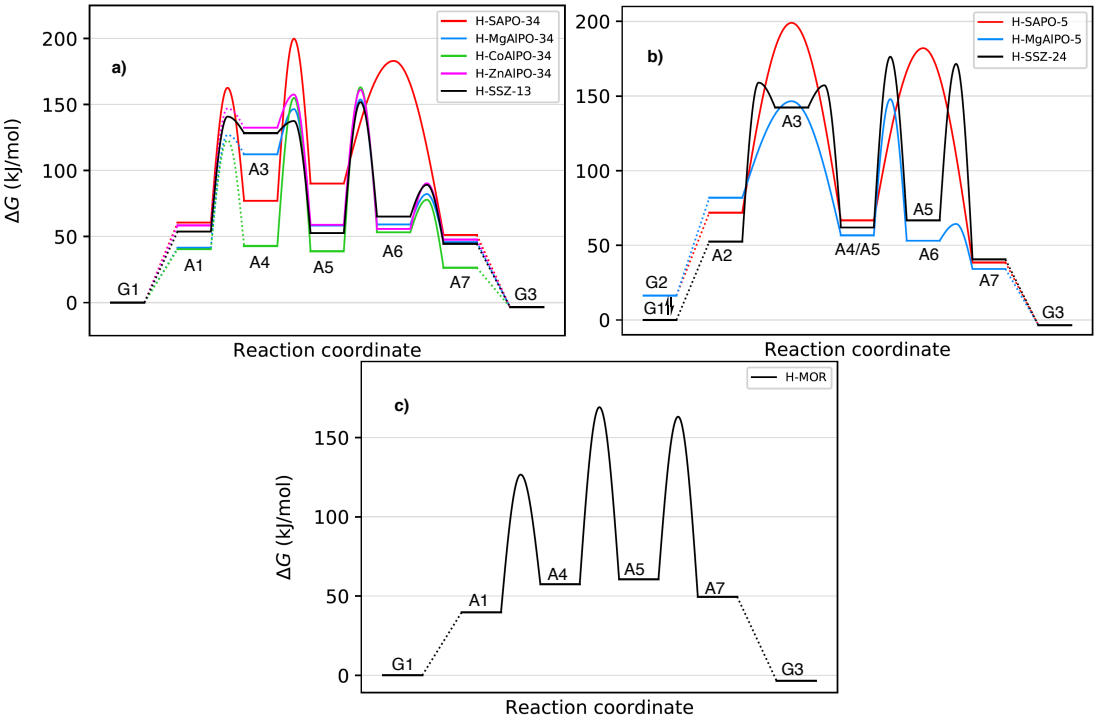

Figure 3.3.: Free energy diagrams of the monomolecular butene isomerization reaction for all calculated zeotypes of a) CHA, b) AFI and c) MOR structure. Reaction barriers that are drawn with a dashed line are estimated barriers. All energies and barriers are given in kJ/mol at T=400 °C and 1 bar.

3.1.2. CHA, AFI and MOR

3.1.2.1. Mechanistic Details

Fig. 3.1 shows all possible reaction pathways for the monomolecular 1- or 2-butene isomerization reaction to isobutene. After adsorption of the gas phase olefin (G1/G2) into the zeolite (A1/A2), three different pathways are possible for the isomerization towards isobutoxide (A5); the pathway taken depends on the zeotype.

- 2-butene can be protonated by the zeolite to form a stable 2-butyl cation (A3) and then either directly chemisorb to the acid site to form n-butoxide (A4), or it can isomerize and chemisorb in a concerted manner to form isobutoxide (A5).
- 2-butene can directly chemisorb to the acid site after protonation to form n-butoxide (A4), and from there isomerize to isobutoxide.
- 1-butene can directly isomerize to isobutoxide in a concerted reaction.

For some of the zeotypes, the isobutyl cation (A6) is not a stable intermediate and isobutoxide directly reacts to isobutene (A7) after desorption from the acid site. For all other zeotypes, the somewhat unstable isobutyl cation is an intermediate. In Fig. 3.3a-c, free energy diagrams are shown for the unimolecular pathway for all investigated CHA, AFI and MOR zeotypes, respectively.
In the CHA zeolite, the TS(A3-A5) barrier is lower than the TS(A4-A5) barrier in all zeolites except the H-CoAlPO-34 one. There, the pathway over n-butoxide has been calculated to have a barrier that is about 3.5 kJ/mol lower than the isobutyl cation pathway. The TS(A5-A6) from isobutoxide to the isobutyl cation is the RDS for all CHA zeolites except H-SAPO-34, in which the TS(A3-A5) is rate determining. Additionally, only in H-SAPO-34 is the isobutyl cation (A6) not a stable intermediate.

Table 3.2.: RDS transition states and barriers of the monomolecular butene isomerization for all investigated zeolites. RDS barriers are given in kJ/mol.

Zeolite	RDS	RDS barrier
H-SSZ-13	TS(A5-A6)	152
H-SAPO-34	TS(A3-A5)	188
H-MgAlPO-34	TS(A5-A6)	154
H-CoAlPO-34	TS(A5-A6)	163
H-ZnAlPO-34	TS(A5-A6)	161
H-SSZ-24	TS(A4-A5)	176
H-SAPO-5	TS(A2-A5)	199
H-MgAlPO-5	TS(A5-A6)	148
H-MOR	TS(A4-A5)	169

In the AFI zeolite, to be able to directly compare the isomerization barriers between the three AFI zeolites, all mechanisms are referenced to 2-butene in gas phase, as can seen in Fig. 3.3b. The initial state of 1-butene in gas phase and the clean zeolite (G2) is therefore 16 kJ/mol uphill in energy compared to 2-butene (G1). As already mentioned earlier, rapid isomerization between 1-butene and 2-butene allows 1-butene to be the reactant for this reaction, even if only 2-butene may be present for the reaction initially.
H-SSZ-24 has been calculated to isomerize 2-butene to isobutoxide through both the 2-butyl cation and n-butoxide, where the TS(A4-A5) is rate determining. For both other investigated AFI structures, isomerization happens directly from 1-butene to isobutoxide (TS(A2-A5)), which is also the RDS. Only for H-MgAlPO-5 is the isobutyl cation a stable intermediate. The TS(A3-A5) transition state was also optimized for both the H-SSZ-24 and the H-MgAlPO-5 zeolites, but have barriers which are 1 kJ/mol and 9 kJ/mol higher than the aforementioned RDSs, respectively. No such transition state could be optimized in H-SAPO-5.
For the H-MOR zeolite, butene isomerization has been calculated to proceed through the n-butoxide - isobutoxide pathway, as shown in Fig. 3.3c. The RDS of this pathway is the isomerization from n-butoxide to isobutoxide (TS(A4-A5)) at 169 kJ/mol.
Interesting to note here is the fact that the energetically most favorable O-site at which either chemisorption or physisorption takes place changes depending on the zeotype. As an example, the isobutoxide (A5) is shown in Fig. 3.4a-e for all investigated CHA zeotypes. For H-SSZ-13, isobutoxide adsorbs at the O3 site, whereas in all other zeotypes, it adsorbs at the O2 site. The energetically most favorable adsorption site has been calculated for these intermediates at the M06 level of theory.

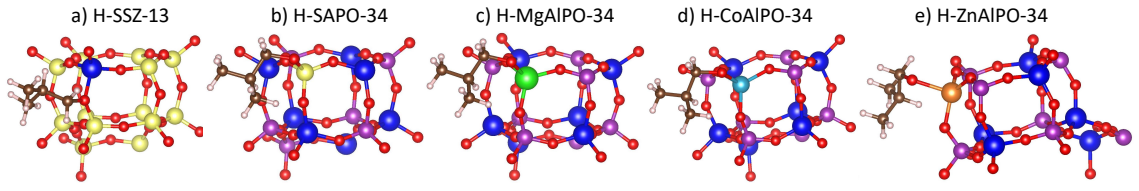

Figure 3.4.: Cutout of the CHA zeolite showing isobutoxide adsorbed at the acid site for five different zeotypes. Coloring: Si - yellow, Al - blue, O - red, acidic H - black, P - purple, Mg - green, Co - turquoise, Zn - orange.

3.1.2.2. Discussion of Reaction Barriers

In Table 3.2, the RDS steps together with the associated RDS barriers for the monomolecular butene isomerization are given for each investigated zeolite. The Mg-substituted zeolites

have very low overall barriers, with H-MgAlPO-5 having the lowest barrier overall of 148 kJ/mol. This makes sense as Mg-substituted zeolites are known to be very strongly acidic, leading to low reaction barriers. Surprisingly, the unsubstituted H-SSZ-13 zeolite also showcases a very low RDS barrier of 152 kJ/mol, even though its acidity is of medium strength. The other end of the spectrum is occupied by the H-SAPO zeolites, which have RDS barriers of 188 and 199 kJ/mol. This is due to their very low acid strength. The acidity of both the Co- and the Zn-substituted CHA zeolites is slightly lower that of H-SSZ-13, leading to barriers of 163 and 161 kJ/mol, respectively.
These findings are substantiated by recent work done by Cnudde et al.,[106] who investigated the isobutene protonation reaction in the H-SSZ-24 zeolite and selected AFI zeotypes using MD simulations and umbrella sampling. They found the reactivity for this reaction to increase in the order of H-ZrAlPO-5 < H-SAPO-5 < H-SSZ-24 < H-MgAlPO-5, which nicely corresponds to the reactivity ordering found here.
The similarly substituted zeolites with differing topologies are now compared to each other. When comparing the CHA with the AFI structures, the AFI zeolites show higher barriers for the monomolecular butene isomerization, except for the Mg-substituted one. Seeing as the C_4 moiety is rather small, the smaller and more confined pore structure of CHA may favor transition states more than the more open and spacious channel structures of AFI and MOR. The unsubstituted H-MOR zeolite has an RDS barrier of 169 kJ/mol, which is 7 kJ/mol lower than that of the H-SSZ-24 zeolite. Since the AFI and MOR zeolite structures only differ slightly in their shape of the channel, this difference may be attributed to a difference in acid strength instead.
Overall, the majority of the calculated barriers are accessible at a temperature of 400 °C. Slower rates are expected for especially the H-SAPO zeolites, while for the H-MgAlPO zeolites as well as H-SSZ-13 the reaction is quick. As an example, calculating the rate constant for H-MgAlPO-34 by using a simple TST approach leads to a value of 46 s^{-1}, while for H-SAPO-5 it is 0.005 s^{-1}.

3.2. Bimolecular Butene Isomerization

3.2.1. Reaction mechanism

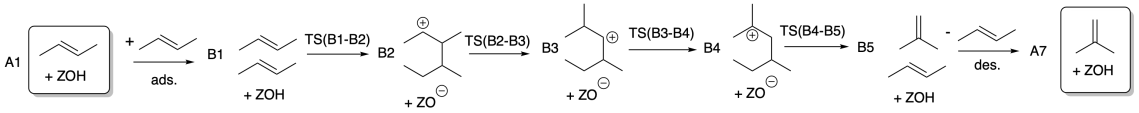

Figure 3.5.: Mechanism of the bimolecular butene isomerization mechanism.

In the bimolecular mechanism, two C_4 olefins adsorb within the same zeolite pore and react with each other, forming a C_8 intermediate that can undergo different hydrogen and methyl shifts. These shifts have been calculated to have very low reaction barriers,[107] which leads to a multitude of different C_8 isomers being produced. After isomerization, the C_8 intermediates can crack again to yield either different C_4 species, in this case n-butene and isobutene, or C_3 and C_5 olefins through uneven β-scission. In the scope of this thesis, only one specific pathway is considered for the C_8 intermediate that yields the desired products, isobutene and 2-butene. This was done to be able to directly compare this to other mechanisms herein. The bimolecular mechanism investigated is shown schematically in Fig. 3.5.
After adsorption of two 2-butene molecules into the zeolite pore (B1), the 2-butene molecule closest to the active site is protonated, which triggers the formation of a new C-C bond between the now positively charged carbon adjacent to the protonated carbon and one of the sp^2 carbons of the second 2-butene molecule, forming the 3,4-dimethylhexan-2-ylium

ion (B2). This ion then first undergoes a methyl shift to 2,4-dimethylhexan-3-ylium ion (B3), and then a hydrogen transfer to form the more stable tertiary 2,4-dimethylhexan-2-ylium ion (B4). Both these shifts have rather low barriers and are therefore expected to happen fast once B2 has been formed. Lastly, the 2,4-dimethylhexan-2-ylium ion can crack into isobutene and the 2-butyl ion, which is readily deprotonated by the acid site to yield 2-butene (B5). The first and last transition states of the bimolecular pathway, olefin dimerization and cracking, mirror each other, with almost identical bond lengths in the transition states (see Fig. C.2 in the appendix). After desorption of both olefins (A7 and G3), one of the two reacting 2-butenes has been isomerized to isobutene. This reaction pathway has been found to be optimal in all of the investigated zeolites herein.

3.2.2. Discussion of Reaction Barriers

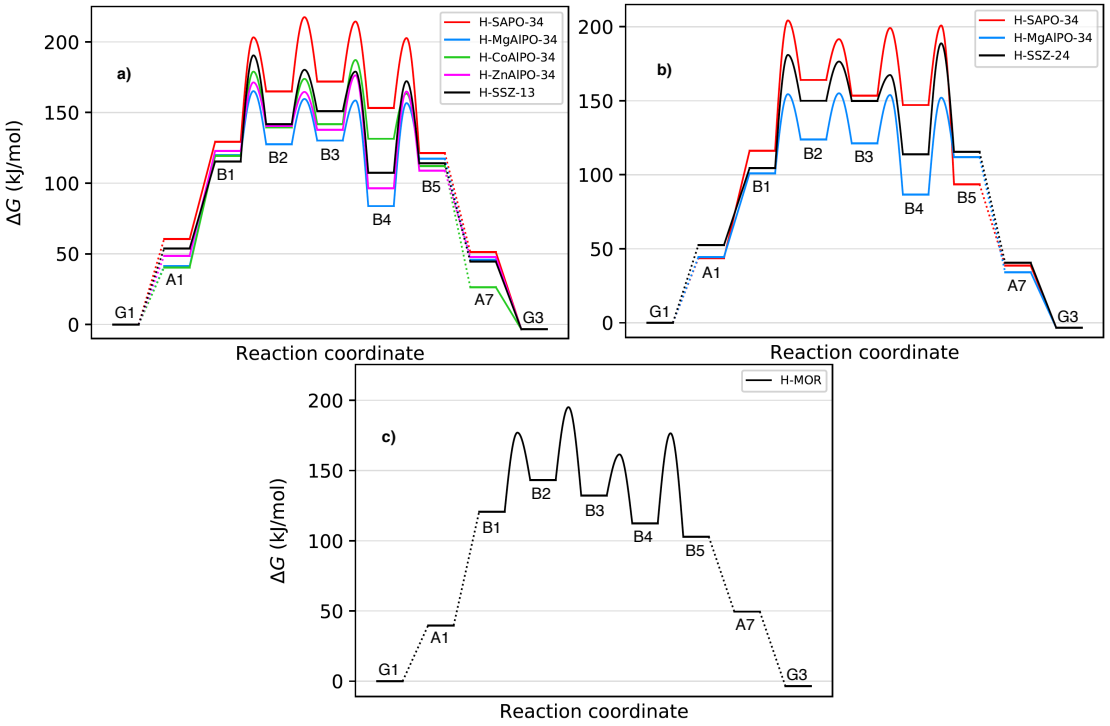

Figure 3.6.: Free energy diagrams of the bimolecular butene isomerization reaction for all calculated zeotypes of a) CHA, b) AFI and c) MOR structure. All energies and barriers are given in kJ/mol at T=400 °C and 1 bar.

The Gibbs free energy pathways for the bimolecular butene isomerization mechanism for all investigated zeolites are shown in Fig. 3.6, with the respective RDS barrier heights given in Table 3.3. Analogous to the monomolecular mechanism, the Mg-substituted zeolites showcase the lowest RDS barriers, with H-MgAlPO-5 being the lowest at 155 kJ/mol, while the H-MgAlPO-34 RDS barrier is 10 kJ/mol higher at 165 kJ/mol. The H-SAPO zeolites have the highest RDS barriers again, with H-SAPO-34 having the highest barrier of all investigated zeolites at 218 kJ/mol. In general, with the exception of the Mg-substituted zeolites, the calculated RDS barriers are fairly high at the reaction temperature of 400 °C, being mostly larger than 180 kJ/mol. These barriers result in rather small reaction rates. For example, calculated rate constants using these RDS barriers are 13.2 s^{-1} for H-MgAlPO-34 and $1.7 \cdot 10^{-4}$ s^{-1} for H-SAPO-34. A comparison between H-SSZ-13, H-SSZ-24 and H-MOR shows that the RDS barriers for these zeolites are all in a small range of 6 kJ/mol. This gives rise to the assumption that the topology of the zeolite framework

Table 3.3.: RDS transition states and barriers of the bimolecular butene isomerization for all investigated zeolites. RDS barriers are given in kJ/mol.

Zeolite	RDS	RDS barrier
H-SSZ-13	TS(B1-B2)	190
H-SAPO-34	TS(B2-B3)	218
H-MgAlPO-34	TS(B1-B2)	165
H-CoAlPO-34	TS(B3-B4)	187
H-ZnAlPO-34	TS(B3-B4)	176
H-SSZ-24	TS(B4-B5)	189
H-SAPO-5	TS(B1-B2)	204
H-MgAlPO-5	TS(B2-B3)	155
H-MOR	TS(B2-B3)	195

does not have as big of an impact on the reactivity towards the bimolecular mechanism as the zeolite acidity does. However, going from H-MgAlPO-34 to H-MgAlPO-5, the RDS barrier decreases by 10 kJ/mol, and going from H-SAPO-34 to H-SAPO-5 it decreases by 14 kJ/mol. This consistent decrease shows that, in general, AFI zeolites are more active towards the bimolecular mechanism than CHA zeolites.
The variety in which step of the reaction pathway is the RDS shows that no one transition state is consistently the highest in the bimolecular mechanism. For example, looking at the free energy diagram for H-MgAlPO-5 in Fig. 3.6b and the corresponding barriers in Table A.1 in the appendix, all four transition states of the reaction pathway are in a range of only 3 kJ/mol. Considering the computational accuracy of the calculations, the deduction of the actual RDS is very delicate in this case, as they all are within the error range of the calculations.
One further reason for the high barriers of the bimolecular mechanism is the necessary co-adsorption of two olefins into the zeolite. As can be seen in Fig. 3.6, the second adsorption step from A1 to B1 comes with an increase in free energy that is equal to or, for many zeolites, higher than the initial olefin adsorption step from G1 to A1. The adsorption energy for two 2-butene molecules in the zeolite (B1) is >100 kJ/mol for all investigated zeolites. This co-adsorption is unfavorable because of strong entropic effects, giving rise to the very high free energies after co-adsorption. The isomerization, on the other hand, is not very demanding: For example, from two 2-butene molecules adsorbed in H-SSZ-13, the difference to the highest transition state is 62 kJ/mol, which is 36 kJ/mol lower than for the monomolecular pathway (98 kJ/mol). But taking the adsorption energies and entropic penalties into account, the free energy difference between the reference molecules and the highest transition state is 190 kJ/mol for the bimolecular pathway, whereas it amounts to only 152 kJ/mol for the monomolecular pathway. This shows that when looking at the actual reaction barriers, it is essential to take entropic effects into account.

3.3. Comparison Between Mono- and Bimolecular Mechanisms

3.3.1. Comparison at 400 °C

To compare the calculated reaction barriers for the mono- and bimolecular mechanisms with each other, the contribution of the enthalpy and entropy parts of the Gibbs free energy to these differences is investigated first. The H-SSZ-13 zeolite will serve as an example case here. In Fig. 3.7, both monomolecular and bimolecular pathways are depicted; Fig. 3.7a shows only the enthalpy contribution ΔH, while Fig. 3.7b shows the Gibbs free energy ΔG.

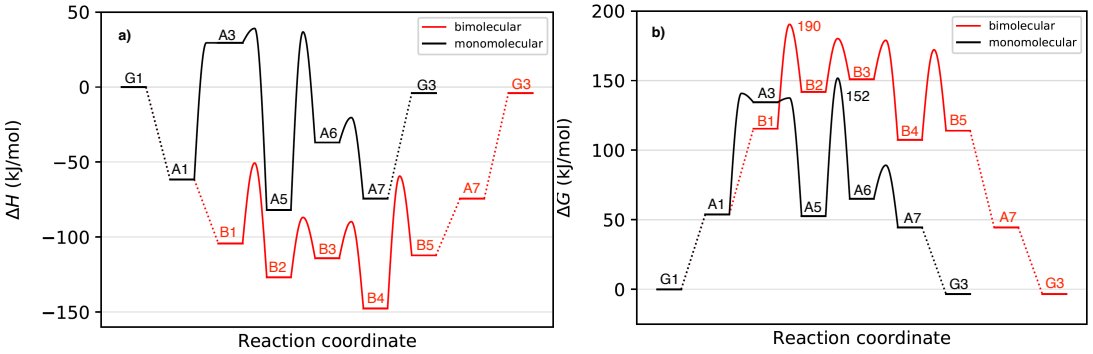

Figure 3.7.: a) Enthalpy diagram of the monomolecular and bimolecular 2-butene isomerization mechanism. b) Free energy diagram of the monomolecular and bimolecular 2-butene isomerization mechanisms. The RDS barriers of the overall mechanisms are 190 and 152 kJ/mol, respectively. All energies are given in kJ/mol, at T=400 °C and 1 bar. All energies and barriers are given in kJ/mol at T=400 °C and 1 bar.

Table 3.4.: Table showing the $\Delta\Delta G$ values for each investigated zeolite at T=400 °C and 1 bar, given in kJ/mol. The $\Delta\Delta G$ values are calculated by subtracting the RDS barrier of the monomolecular mechanism from the RDS barrier of the bimolecular mechanism.

Zeolite	RDS $\Delta\Delta G$ [kJ/mol]
H-SSZ-13	39
H-SAPO-34	29
H-MgAlPO-34	11
H-CoAlPO-34	24
H-ZnAlPO-34	15
H-SSZ-24	12
H-SAPO-5	5
H-MgAlPO-5	7
H-MOR	26

When comparing the calculated enthalpic (Fig. 3.7a) and free energy pathways (Fig. 3.7b) for the bimolecular mechanism, it is evident that there is a large difference originating from the huge entropy penalty due to the adsorption of two olefins within the pore of H-SSZ-13. While the bimolecular mechanism seems to be more favorable than the monomolecular mechanism judging from Fig. 3.7b, the inclusion of entropic contributions reveals that the bimolecular mechanism has higher overall free energy barriers. Note that a similar effect has been observed for the concerted and step-wise mechanism of the methylation of olefins.[45] The most important difference between the monomolecular and bimolecular pathways is the fact that in the latter, co-adsorption of a second olefin into the zeolite pore is necessary (A1 to B1), as was already mentioned before.

To identify whether the mono- or the bimolecular 2-butene isomerization mechanism is predominant in which zeolite, the differences in RDS barriers between these two mechanisms for our investigated zeotypes have been calculated, shown in Table 3.4 as $\Delta\Delta G$ values. They are calculated by subtracting the RDS barrier of the monomolecular mechanism from the RDS barrier of the bimolecular mechanism. The $\Delta\Delta G$ value is positive for all zeotypes, meaning that the monomolecular reaction barrier is always lower than the bimolecular barrier. The largest $\Delta\Delta G$ value was calculated for H-SSZ-13 at 39 kJ/mol. The other zeotypes have lower $\Delta\Delta G$ values, ranging from 29 kJ/mol for H-SAPO-34 to 5 kJ/mol for

H-SAPO-5.
It is important to stress here that for these transition states, translational degrees of freedom of the adsorbed species make up for a significant part of the entropic contribution to the reaction barrier. These contributions are only poorly described within the harmonic oscillator approximation, leading to fairly large errors in the reaction energies (estimated to be up to 20 kJ/mol too large for an adsorbed C_4 species).[108] This error is then expected to be doubled for the bimolecular mechanism due to the co-adsorption of two C_4 hydrocarbons. Therefore, when further discussing the calculated $\Delta\Delta G$ values here, it is assumed that the true Gibbs free energy difference may be up to 20 kJ/mol lower than the calculated values in Table 3.4. Considering this, the true $\Delta\Delta G$ value for the H-SSZ-13 zeolite is expected to be roughly 20 kJ/mol. At this difference, while the monomolecular mechanism is obviously still dominant, the bimolecular mechanism can be considered as a competing mechanism. The difference of 20 kJ/mol in the free energy barrier results in a difference of factor 36 in the rate constant, i.e. the monomolecular mechanism is 36 times faster than the bimolecular mechanism.
Looking at e.g. the H-CoAlPO-34 zeolite with a $\Delta\Delta G$ value of 24 kJ/mol, the monomolecular mechanism is still dominant, similar to the H-SSZ-13 zeolite, but the true barrier of the bimolecular mechanism is expected to be only slightly higher. A difference of 4 kJ/mol in free barriers means that the monomolecular rate constant is higher than the bimolecular one by only a factor of 2. Therefore, it can be surmised that isobutene is formed in approximately equal amounts from both mono- and bimolecular mechanisms in this zeolite, especially considering the uncertainty of the approximation in the decrease of the $\Delta\Delta G$ values.
For all zeolites with calculated $\Delta\Delta G$ values <20 kJ/mol, the true $\Delta\Delta G$ values are expected to be negative, leading to the conclusion that the bimolecular mechanism is dominant for butene isomerization in all those cases. This is the case for all investigated AFI zeolites, showing that the bimolecular mechanism is, in general, favored in the AFI zeolite. Seeing how the $\Delta\Delta G$ values consistently decrease going from CHA to AFI with the same type of framework and substitution, this can be attributed to the different framework topology.
As was shown in section 1.2, the topology of a specific zeolite can have large effects on the selectivity towards certain products in a reaction. One of these topology effects comes from the size of the pore in a pore zeolite like CHA, or the size of the channel in a channel zeolite like AFI. CHA is a rather small pore zeolite, with a pore window size of 0.38 x 0.38 nm.[102] AFI on the other hand has rather large channels of 7.3 x 7.3 Å due to the 12-ring channel structure. Since in the bimolecular mechanism a fairly large C_8^+ cation is formed, it is intuitive that the AFI zeolite would be more reactive towards it. The whole reaction pathway of the C_8^+ cation may require rotational rearrangement of the cation in the zeolite, which is expected to be difficult in the small CHA pore, but simple in the large AFI and MOR channels. However, the $\Delta\Delta G$ value for H-MOR is fairly high at 26 kJ/mol. This suggests that the zeolite acidity of H-MOR is somewhat lower than that of the H-SSZ-24 zeolite. As both AFI and MOR have channel structures of 12-ring channels, it is not expected that the difference in topology has any large impact on the selectivity towards one of the two reaction mechanisms. However, delineating the influences of acidity and framework from each other is difficult when considering only one specific zeolite.
One can further argue that the loss of translational entropy upon adsorption into the AFI and MOR zeolites is even more poorly described by the harmonic approximation than it is for the CHA zeolite. In CHA, especially the C_8 molecules are trapped inside the pore, as they are too big to be able to diffuse outside of the pore. In AFI and MOR, it may be possible for a C_8 molecule to still move along inside the channel of the zeolite, and therefore retain some of its translational entropy. This retainment of translational entropy would result in the reaction barriers being too high, which reinforces the argument that the bimolecular mechanism is dominant in AFI type zeolites. Additionally, this strengthens the argument

that non-C_4 side products are indeed likely to be produced through uneven β-scission, even if the even cracking reaction is favored, due to the low free energy barriers in AFI type zeolites.

3.3.2. Entropic Contributions for the Adsorption Steps

Exemplary for the H-SSZ-13 zeolite, it is interesting to investigate to which extent the poor description of the entropy, specifically due to the adsorption in the zeolite, has an influence on the reaction barriers for the two butene isomerization mechanisms. For the adsorption of alkanes in zeolites, investigations have been carried out assuming a loss of 1/3 of the molecules translational entropy upon adsorption, as the adsorbed species are still able to retain some translational modes inside the zeolite pore.[109,110] In the following, the approximation that adsorbed species retain 2/3 of the translational entropy of the corresponding gas phase species is considered, which generally lowers the Gibbs free energy of adsorbed species. For most cases, this concerns the entropy of the reactant 2-butene, with $T\Delta S_{\mathrm{trans,gas}} = 118.5$ kJ/mol at T = 400 °C. In practice, the simplest way to do this is to shift the entropic contribution of the gas phase reference by this amount ($\frac{2}{3}T\Delta S = 78.9$ kJ/mol), effectively increasing the Gibbs free energy of 2-butene. Importantly, simply ΔS at 1 bar reference pressure is employed here. The 2/3-fraction of the translational entropy corresponds to two degrees of freedom and to avoid double counting, the corresponding number of vibrational degrees of freedom from adsorbed species (two for C_4-species and four for two co-adsorbed C_4-species) have been removed. Here the two or four lowest vibrational frequencies have been removed. The effect of removing these frequencies is rather small ($\leq$20 kJ/mol) compared to the correction stemming from $\frac{2}{3}T\Delta S$.

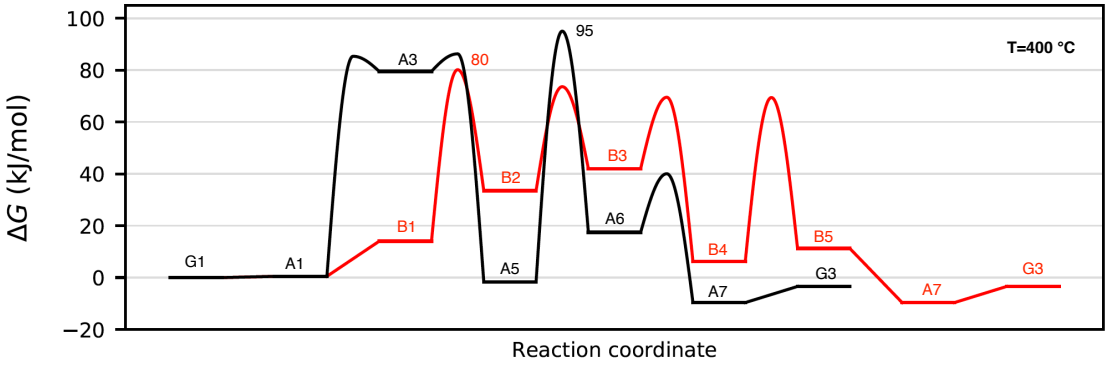

Figure 3.8.: Free energy diagram for the unimolecular (black) and bimolecular (red) 2-butene isomerization mechanisms at 400 °C, where adsorbed molecules retain 2/3 of their translational gas phase entropy (2-butene or isobutene). Energies and barriers are given in kJ/mol and referenced to the clean zeolite and 2-butene in gas phase.

Fig. 3.8 shows the free energy diagram obtained in this way. The barriers that have been calculated this way should be seen as a lower bound as it is expected that a significantly higher fraction of translational entropy is lost when considering the tightly bound transition states. However, this analysis nicely highlights that a different treatment of entropic contribution would decrease the overall barriers for the bimolecular pathway by twice the amount, hence decreasing their free energy differences.
This then reinforces the argument that the true $\Delta\Delta G$ values are indeed lower than those reported in table 3.4. This decrease is however expected to be larger for the CHA zeolite, as it has harsher confinement effects than the AFI and MOR zeolites.

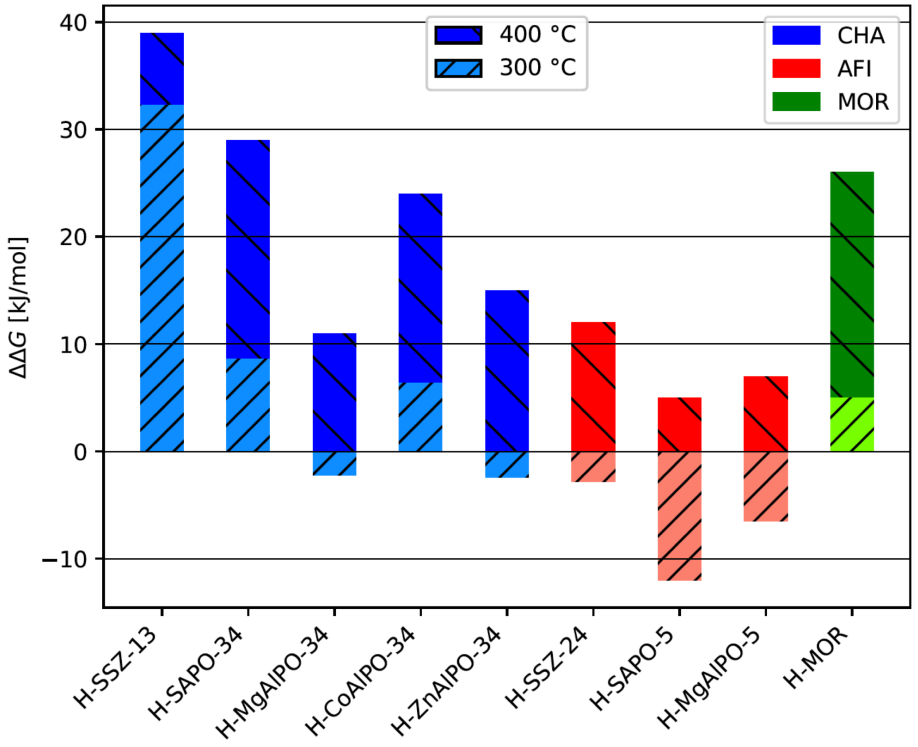

Figure 3.9.: Comparison of the free energy barriers of the rate determining steps between the monomolecular and bimolecular butene isomerization mechanisms for all investigated zeolites. Barriers differences are calculated at both T=400 °C and T=300 °C and given in kJ/mol.

3.3.3. Comparison at Different Temperatures

While the general consensus is that the monomolecular and bimolecular mechanisms are the two main reaction pathways through which butene isomerization occurs, there still is an ongoing debate in the literature about which of these mechanisms is predominant for which catalytic system and under which conditions.[9,25,28–33,35,104] We try to shed some light onto this by comparing the two mechanisms to each other for our investigated systems at two different temperatures. For this, ΔΔG values were calculated, which are the differences in the free energy barriers of the rate determining step of the mono-and bimolecular mechanisms. These ΔΔG values were calculated at both 400 °C and 300 °C and are shown in Fig. 3.9. The ΔΔG values at 400 °C will be discussed first, where it can be seen that, without exception, all zeolites show a positive ΔΔG value, indicating that the monomolecular free energy barriers are consistently lower than those of the bimolecular mechanism.

It is important to keep in mind that the overall accuracy of the used method (cluster-model corrections using the M06 functional) has been shown to yield average errors of 7 kJ/mol for a benchmark of transition states in the zeolite-catalyzed methanol-to-olefins process,[40] which contains transition states similar to the ones investigated here. Only the AFI zeolites H-SAPO-5 and H-MgAlPO-5 are in that range with ΔΔG values of 5 kJ/mol and 7 kJ/mol, respectively. For these two zeolites, as well as H-MgAlPO-34, H-SSZ-24 and H-ZnAlPO-34, the argument can be made that both mechanisms are competing and may contribute to butene isomerization equally. This is not the case, however, for all other investigated zeolites which have ΔΔG values of >20 kJ/mol, leading to the conclusion that the monomolecular mechanism is clearly dominant in those cases.

At the lower temperature of 300 °C, the ΔΔG values change drastically, with the exception of H-SSZ-13, where the ΔΔG value decreases only by 7 kJ/mol. For all other zeolites, the

decrease of the ΔΔG value caused by the change in reaction temperature ranges from 13 kJ/mol for H-MgAlPO-34 up to 21 kJ/mol for H-MOR. The small difference in ΔΔG values for the H-SSZ-13 zeolite can be explained by the fact that the reaction step that is the rate determining step changes from TS(A5-A6) at 400 °C to TS(A1-A3) at 300 °C. The pathway through n-butoxide in H-SSZ-13 (A4-A5) has also been calculated, for which the rate determining step barrier is 181 kJ/mol at 400 °C (see Table A.1), leading to a ΔΔG value of 9 kJ/mol. The decrease in ΔΔG values causes them to be negative for all AFI zeolites as well as the two most acidic CHA zeolites, meaning that for them the bimolecular mechanism is now predominant over the monomolecular mechanism. The lowest ΔΔG value at 300 °C can be seen for H-SAPO-5 at -12 kJ/mol.
The first conclusion is that lower temperatures favor the bimolecular mechanism. This makes sense because of the difference in the number of molecules that adsorb into the zeolite pore. One can additionally look at the influence of the topology by comparing the ΔΔG values of CHA with AFI. Here it can clearly be seen that the CHA zeolites show much higher ΔΔG values than the AFI zeotypes. While the ΔΔG value for MOR is fairly high at 26 kJ/mol at 400 °C, the decrease with the change in temperature is the largest for all zeolites, going down to 5 kJ/mol at 300 °C. It is therefore concluded that the cavity-type zeolite CHA favors the monomolecular mechanism, while the channel-type zeolites AFI and MOR favor the bimolecular mechanism, especially at lower temperatures. This is also substantiated by findings in the literature, where large pore size zeolites like zeolite H-Beta have been found to be preferable for the bimolecular mechanism,[111] while small channel or pore zeolites like ferrierite (FER) enable the monomolecular mechanism.[112,113]
It needs to be stressed that for the transition states that are discussed here, translational degrees of freedom of the adsorbed species make up for a significant part of the entropic contribution to the reaction barrier. These contributions are only poorly described within the harmonic oscillator approximation, leading to fairly large errors in the reaction energies (estimated to be up to 20 kJ/mol too large for an adsorbed C_4 species).[104,108] This error is then expected to be doubled for the bimolecular mechanism due to the co-adsorption of two C_4 hydrocarbons. This line of reasoning has been previously used to argue that even at a ΔΔG value of 39 kJ/mol for H-SSZ-13, the bimolecular mechanism can still be considered as a competing mechanism.[104] Therefore, when further discussing the calculated ΔΔG values here, it is assumed that the true free energy difference is up to 20 kJ/mol lower than the calculated values. Considering these points, it is deduced that for the H-CoAlPO-34 zeolite with a ΔΔG value of 24 kJ/mol, the monomolecular mechanism is still dominant, similar to the H-SSZ-13 zeolite, but the true barrier of the bimolecular mechanism is expected to be only slightly higher. Therefore, it is surmised that isobutene is formed in approximately equal amounts from both mono- and bimolecular mechanisms in this zeolite. For all other investigated zeolites, the true ΔΔG values are expected to be negative for all zeolites except H-SSZ-13, leading to the conclusion that the bimolecular mechanism is dominant for butene isomerization in all those cases.
One can further argue that the loss of translational entropy upon adsorption into the CHA zeolite is even more poorly described by the harmonic approximation than it is for the AFI and MOR zeolite. In CHA, especially the C_8 molecules are trapped inside the pore, resulting in the loss of translational and rotational degrees of freedom, which the harmonic approximation fails to describe. In AFI and MOR, it may be possible for a C_8 molecule to still move along inside the channel of the zeolite as well as rotate due to the large channels, therefore retaining some of its translational and rotational entropy. This discrepancy results in further inaccuracies one has to be mindful of when comparing the calculated ΔΔG barriers reported here.

4. Formation of Side Products During Butane Isomerization

In this chapter, we first take a look at the product distribution of n-butane isomerization experiments. Afterwards, the origin of the main side products of the reaction, which are propane and pentane, is discussed. The methyl transfer (MT) mechanism is presented as a new reaction mechanism that can explain the formation of these prominent side products, the full mechanism of which is investigated within the H-SSZ-13 zeolite. After identification of the RDS, the mechanism is calculated up until this reaction step for all other zeolites and zeotypes, and the resulting barriers are discussed. Lastly, the RDS barriers of the MT mechanisms are compared with the RDS barriers of the bimolecular mechanism to conclude how the mechanisms compete against each other for the formation of C_3 and C_5 hydrocarbons.

4.1. Experimental Findings

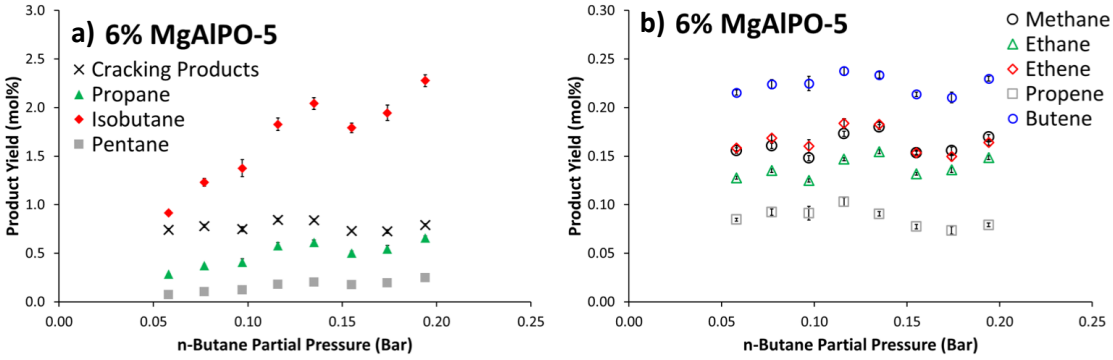

Figure 4.1.: Catalytic data for the n-butane isomerization reaction, using 6% MgAlPO-5 as the catalyst. Shown is the variation in product yield of the main products, as a function of n-butane partial pressure between 0.05 and 0.20 bar. a) Shows the main products of the reaction, highlighting n-butane as the main product, and combining all smaller cracking products into one data point. b) Shows the product yield of the cracking products for 6% MgAlPO-5. Conditions: 0.6 g of catalyst, T=400 °C, flow rate: 496 µmol/g. All experimental work has been performed by Matthew E. Potter of the School of Chemistry, University of Southampton, who also created the figures shown here. Permission to use the data shown here has been specifically granted by Matthew E. Potter.

The n-butane isomerization reaction has been investigated extensively in the literature to gain insights into reaction mechanisms, effects of different zeolite structures and acidities, and also product distribution. It is known that when performing the n-butane isomerization, propane and pentane side products are very prominent, with smaller amounts of hydrocarbons of other chain lengths being produced as well. For an experimental insight, the focus here lies on the experimental work performed by Matthew E. Potter of the

University of Southampton. Here, the n-butane isomerization reaction was performed with 0.6 g of the strongly acidic H-MgAlPO-5 catalyst, using a combined n-butane and nitrogen flow, corresponding to a total of 3.91 to 3.94 mL/min, depending on the desired partial pressure. The catalyst was sieved between 300 - 500 µm and then used as a 4 cm high catalyst bed. Product distribution was investigated using gas chromatography, the results of which are shown in Fig. 4.1. The product distribution of the main products is shown in Fig. 4.1a, the prominent one being the desired product isobutane with a product yield of 2.3 mol% at 0.19 bar n-butane partial pressure. The two most prominent side products of the reaction are propane and pentane, with 0.6 and 0.25 mol%, respectively. This shows that while isobutane is indeed the dominant product, significant amounts of especially propane are produced during the reaction as well.
Further cracking products are shown in Fig. 4.1a as black crosses, and broken down in more detail in Fig. 4.1b. These cracking products are made out of alkanes like methane and ethane, as well as olefins like ethene, propene and butene. Of these other products, butene is produced at a somewhat significant rate of 0.23 mol% at 0.19 bar n-butane partial pressure. This, as well as the production of other olefins with chain lengths differing from C_4, substantiates the fact that olefinic species are paramount in the n-butane isomerization reaction.
While the C_2 hydrocarbons ethane and ethene, as well as methane, are indeed byproducts of the n-butane isomerization reaction, they are produced in only very minor amounts of below 0.2 mol%. The focus of the mechanistic investigations here lies in explaining the main side products, which are of C_3 and C_5 chain length. One of the reasons why the bimolecular pathway has been considered for n-butane isomerization is that through the possibility of uneven β-scission, it can explain side product hydrocarbons with chain lengths other than four. A barrier for the cracking of 2,3,4-trimethylpent-2-ene into C_3 and iso-C_5 in H-SSZ-13 has been calculated by Pleßow and Studt[86] and is shown to be 168 kJ/mol; 57 kJ/mol higher than the even scission of a similar C_8 intermediate (E-3,4,4-trimethylpent-2-ene into C_4 and iso-C_4). Other uneven β-scission reactions are calculated to exhibit even higher barriers. This shows that the even cracking towards two C_4 species is favored for C_8 cracking, likely because of the ability to form the stable t-butyl cation intermediate. Still, uneven β-scission is expected to be prominent due to the product distribution of experiments. Further, it is stressed here that these calculations just described have been performed using the less acidic H-SSZ-13 zeolite; for the H-MgAlPO-5 zeolite used in the experiment, the barriers are expected to be significantly lower. However, another mechanistic possibility of non-C_4 side products being produced that does not involve scission of longer chain hydrocarbons will be proposed in the following.

4.2. Methyl Transfer Mechanism

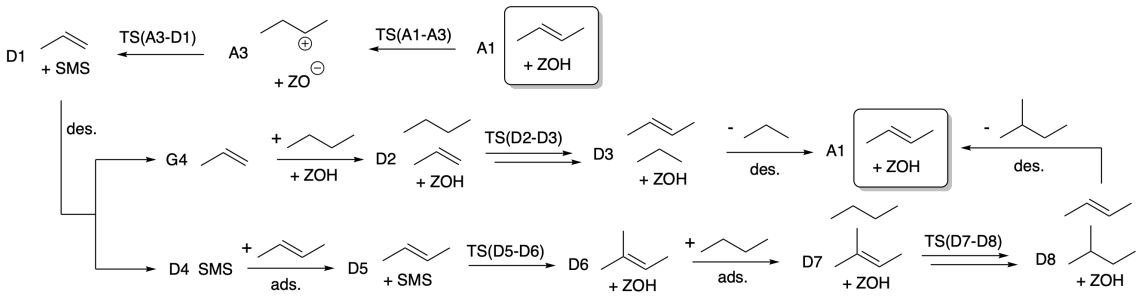

Figure 4.2.: Overview of the methyl transfer mechanism.

As discussed above, C_3 and C_5 hydrocarbons are the main by-products formed during n-butane isomerization which is typically attributed to the bimolecular mechanism. An

alternative possibility for their formation that is investigated here is the transfer of a methyl group (methyl transfer, MT) from an olefin to the acid site, forming a surface methoxy species (SMS or ZOMe), while reducing the olefin length by one CH_2 unit. Note that this reaction is, in principle, the reverse reaction of the methanol-to-olefins (MTO) initiation reaction.[114]
A detailed overview of the MT reaction mechanism is shown in Fig. 4.2. There, adsorbed 2-butene (A1) is first protonated by the acid site, forming the 2-butyl cation (A3), from which a CH_3 group can then transfer back to the acid site, forming propene and an SMS (D1). This is the key reaction step, in which the carbon number of the hydrocarbon changes. The transition state of this reaction in H-SSZ-13 is shown in Fig. 4.3 together with some important bond lengths.

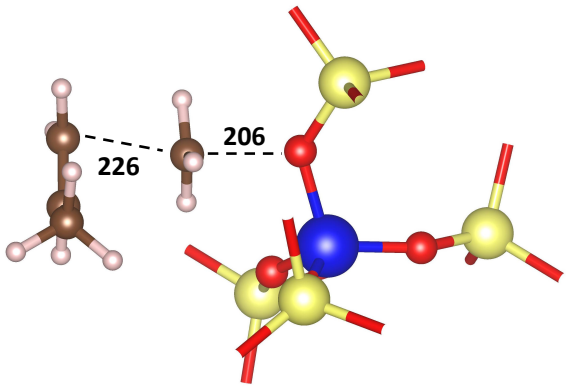

Figure 4.3.: Transition state image of the RDS of the methyl transfer mechanism, TS(A3-D1), which is the methyl shift from the 2-butyl cation to the acid site, in the H-SSZ-13 zeolite. Coloring: blue - Al, yellow - Si, red - O, brown - C, white - H. Key bond distances are given in pm.

Incidentally, this reaction step is also the RDS for this reaction mechanism, as will be shown later in Fig. 4.4.
After this reaction, the propene molecule can desorb into the gas phase (G4), leaving the SMS behind (D4). Now a second 2-butene molecule can adsorb at the SMS (D5) and, after being methylated, yields 2-methylbut-2-ene and the clean acidic zeolite (D6). The 2-methylbut-2-ene molecule can afterwards desorb and partake in the next reaction. This way, both C_3 and C_5 olefins can be produced by means of methyl shifts, without any cracking of larger hydrocarbons.
After the C_3 and C_5 olefins have been formed, they can both co-adsorb together with n-butane into the zeolite (D2 and D7). After co-adsorption, the olefins can be converted into alkanes, while n-butane is converted to 2-butene, yielding pentane (D8) as well as propane (D3) co-adsorbed with 2-butene, respectively. These transition states are intermolecular hydrogen shifts and will be discussed in the following chapter. It is noted here, however, that the reaction steps TS(D2-D3) and TS(D7-D8) consist of two seperate transition states each. For simplicity, they have been contracted to one reaction step in the reaction scheme. Both transition states are shown in an exemplary way for H-SSZ-13 in the discussion of the reaction barriers in Fig. 4.4.
After their formation, the formed propane and pentane molecules can then desorb from the zeolite pore, leaving adsorbed 2-butene behind (A1), which is the primary reactant for this mechanism. It is important to note here again that only the reaction pathway leading to the C_3 and C_5 side products was investigated, as those are the main side products of the main reaction. It is in principle possible to, for example, have a methyl shift from an SMS to pentene to form hexene, which then may crack into two propene molecules. This may serve as an explanation as to why more than twice as much propane than pentane is

formed during the reaction. However, reaction pathways and barriers for these reactions have not been computed in this thesis.

4.3. Discussion of Reaction Barriers

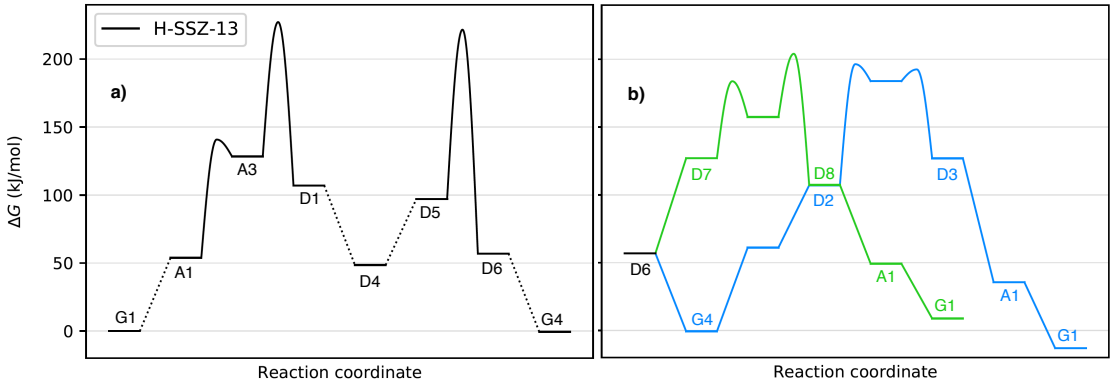

Figure 4.4.: Free energy diagrams for the full methyl transfer mechanism in H-SSZ-13, leading to the products of propane and 2-methyl-2-butane. a) Shows the reaction barriers for the formation of C_3 and C_5 olefins. The rate determining step TS(A3-D1) has a barrier of 227 kJ/mol. b) Shows the hydrogen transfer reactions that convert the C_3 and C_5 to the respective alkanes. The C_3 hydrogenation pathway is shown in blue, and the C_5 hydrogenation pathway is shown in green. All energies and barriers are given at T=400 °C and p=1 bar, referenced to the empty zeolite and 2-butene in the gas phase.

The full reaction pathway was investigated in the H-SSZ-13 zeolite. A free energy diagram showing the reaction steps up until the formation of the propene and pentene is shown in Fig. 4.4a. The following barriers to convert those olefins into alkanes are shown in Fig. 4.4b. These reactions are hydrogen transfers between alkanes and olefins, which will be discussed in detail in the following chapter.
The methyl transfer (MT) mechanism was originally proposed as another possible pathway other than the bimolecular mechanism that could explain how non-C_4 side products like C_3 and C_5 may be formed during butane isomerization. The investigations show that the rate determining step in this mechanism is always the methyl transfer from the 2-butyl cation to the acid site to form propene and a SMS (TS(A3-D1) in Table 4.1). The transition state TS(D5-D6), which is the methyl shift from an SMS to 2-butene to form 2-methylbut-2-ene, also shows a very high barrier of 222 kJ/mol. This indicates that these methyl shifts from a hydrocarbon to the Brønsted acid site are likely to be accompanied by very high reaction barriers. Calculations of the TS(D5-D6) in a few other zeolites showed that the methyl transfer to form propene has a higher barrier than the methyl shift to form pentene in those cases as well (see Table A.1, TS(D5-D6) in the appendix). Therefore, after the H-SSZ-13 zeolite, the MT mechanism was only investigated up to the methyl shift transition state TS(A3-D1) for all zeolites, and more thoroughly for a few other zeolites. The resulting free energy diagrams are shown in Fig. 4.5, with the corresponding RDS barriers given in Table 4.1. As for some zeolites the 2-butyl cation (A3) was not found to be a stable intermediate, the reaction barrier was simply drawn from A1 to D1 in those cases. The geometry of the transition state TS(A3-D1) differs only very slightly between the different zeolite structures.

Taking a look at the calculated free energy barriers for this reaction, it can be seen that the barriers are much larger than 200 kJ/mol for all zeotypes. For example, the reaction

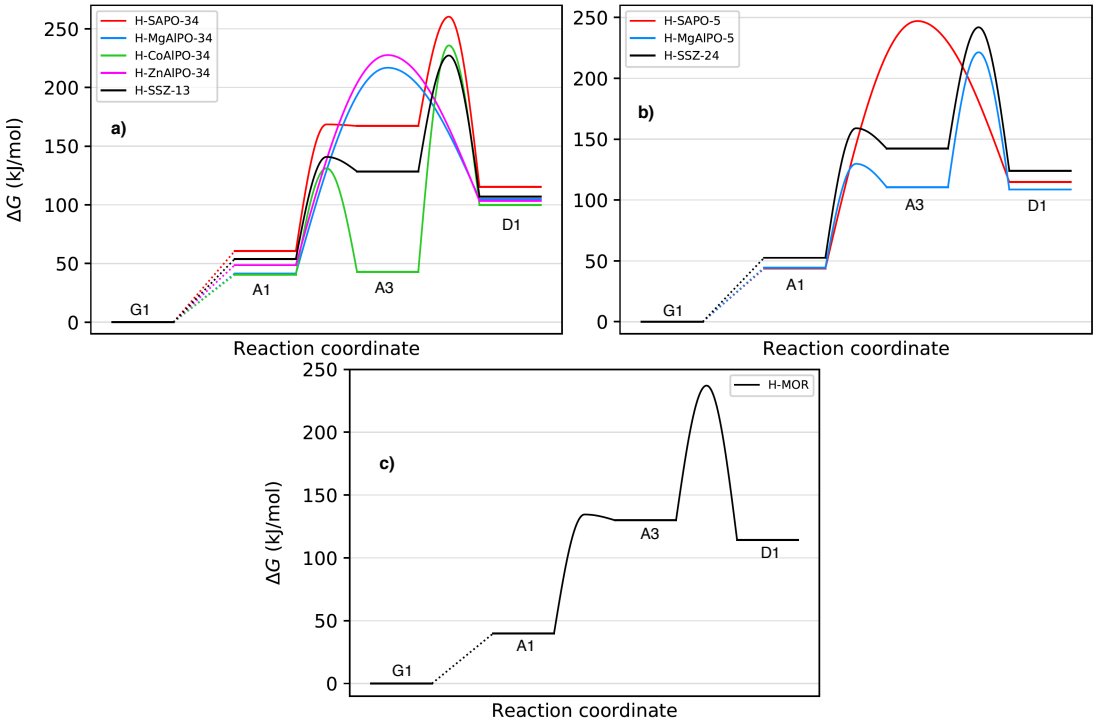

Figure 4.5.: Free energy diagrams of the methyl shift mechanism, up to the RDS of the methyl shift, for all investigated zeotypes of a) CHA, b) AFI and c) MOR structure. The RDS barriers are given for each zeolite in Table 4.1. All energies and barriers are given in kJ/mol at T=400 °C and p=1 bar.

Table 4.1.: RDS barriers of the methyl transfer mechanism for all investigated zeolites. The RDS for all zeolites is TS(A3-D1). RDS barriers are given in kJ/mol at T=400 °C.

Zeolite	RDS barrier
H-SSZ-13	227
H-SAPO-34	260
H-MgAlPO-34	217
H-CoAlPO-34	236
H-ZnAlPO-34	228
H-SSZ-24	242
H-SAPO-5	247
H-MgAlPO-5	221
H-MOR	237

between n-butene and an acid site yielding a SMS is accompanied by a free energy barrier of 227 kJ/mol for H-SSZ-13, which is 37 kJ/mol higher than the even C_8 cracking barrier into isobutene and 2-butene, given in Table 3.3. Using the simple TST approach, this barrier gives a rate constant of $3.4 \cdot 10^{-5}$ s^{-1}, which is almost a factor of 1000 times slower than the bimolecular pathway. Considering this, one might argue that the methyl transfer is not likely to play any role in the n-butane isomerization reaction scheme. It is important to note, however, that the comparison between the two reaction pathways also greatly depends on the partial pressures and temperature, since the MT reaction is monomolecular. The calculated barriers for the MT mechanism therefore do not suffer from an additional co-adsorption penalty for the entropy of the system, like it is the case for the bimolecular mechanism.

This indicates that for zeolites with lower barriers for the MT mechanism (close to 200

kJ/mol), the MT mechanism may be competing for the formation of side products after all, depending on the reaction conditions. A rough estimate is that the MT mechanism may play a role for the zeolites H-SSZ-13, H-MgAlPO-34 and H-MgAlPO-5. For all other investigated zeolites, the RDS barriers are too high to give reasonable rate constants, even considering the inaccuracies in the entropic contribution. The conclusion therefore is that the non-C_4 side products are predominantly formed through uneven β-scission of longer-chain hydrocarbons within the bimolecular mechanism.

5. Origin of Olefinic Species During Butane Isomerization

In this chapter, some ideas about where the olefinic species needed for the n-butane isomerization may originate from are first given and discussed. In a new mechanistic idea, the hydrogen transfer mechanism is then introduced and the mechanism explained. The RDS barriers are calculated and discussed for CHA, AFI and MOR zeolites and afterwards compared to each other, followed by a discussion about how much this new pathway is able to contribute to the reaction network of n-butane isomerization.

5.1. Possibilities for the Production of Olefins

Up until this point, only the butene isomerization reaction of 2-butene to isobutene has been the focus of attention. This leaves the problem of figuring out where the olefinic species, which are certainly needed for the isomerization reaction to happen in the first place, are originating from. In principle, there are four different possibilities that one can think of:

- The olefinic species are present as a reactant from the start. For example, the n-butane feed that is used in experiments may be contaminated by a small amount of olefinic impurities, which are able to catalyze the n-butane isomerization reaction. This would require for very small amounts of olefins to be able to either catalyze the entire reaction cycle, or to enable a reaction mechanism through which more olefins can be produced.

- The olefinic species may be formed by coking of the catalyst. Coke exists almost entirely of hydrocarbons, which can be aliphatic and aromatic in nature. Coke composition research done for the n-butene isomerization reaction over a H-FER zeolite at 350 °C shows that the coke that is produced during the reaction contains large amounts of aromatic compounds.[115] Usually, coking is an unwanted side reaction during catalytic processes that utilize zeolites as catalysts, as the coke species grow large and are able to deactivate the catalyst by blocking the catalyst pores. However, the amount of coke as well as the size of the coke species increases over time during the reaction. It is therefore not unreasonable to argue that slight catalyst coking may be able to catalyze the n-butane isomerization reaction, if the coke species are unsaturated. How these hypothetical coke species fit into the reaction scheme, we will discuss in this chapter.

- Olefins may be produced during the reaction through a direct dehydrogenation of the reactant n-butane to the 2-butyl cation and H_2, catalyzed by the zeolite. The 2-butyl cation can then be deprotonated again to yield butene and recover the zeolite Brønsted

active site. This reaction has been investigated in this work for the H-SSZ-13 zeolite, and a reaction barrier of 247 kJ/mol was found at 400 °C and 1 bar. This reaction was therefore disregarded as a possibility for olefin production due to the extremely high barrier. In the other investigated zeolites as well, the direct dehydrogenation barrier is not expected to be lower than 200 kJ/mol and is therefore not considered any further.

- Olefins may be produced during the reaction through the transfer of hydrogen between co-adsorbed hydrocarbons, specifically, one alkane and one olefin molecule. It is important to note here that while this reaction is able to produce olefins using alkanes, at least a very small amount of olefins needs to be present here initially, as it was discussed in the first point. Due to the nature of this olefin production consisting of only these hydrogen transfers between hydrocarbons, we call this the intermolecular hydrogen transfer (HT) mechanism, which will be presented in the following.

5.2. Intermolecular Hydrogen Transfer Mechanism

5.2.1. CHA

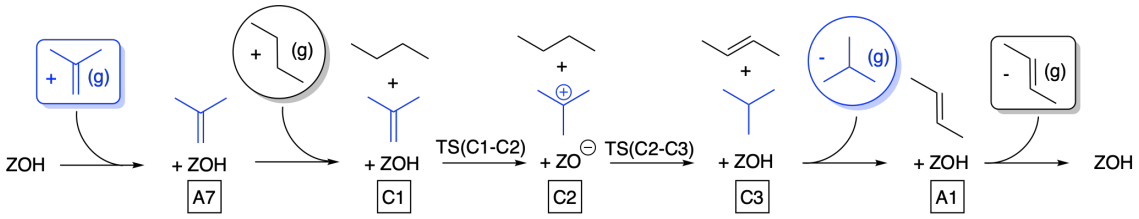

Figure 5.1.: Mechanistic scheme of the hydrogen transfer reactions to convert selected olefins into the respective saturated alkanes. Shown here in blue is the mechanism converting isobutene into isobutane; the same mechanism is used for converting propene into propane and 2-methylbut-2-ene into 2-methylbutane. Structure C2 needs to rotate 180° in the cavity before the second hydrogen transfer can take place. Intermediate energies and reaction barriers for this mechanism are given in Table **??** below.

A reaction mechanism for hydrogen transfers (HTs) between olefins and hydrocarbons is illustrated in Fig. 5.1, for two C_4 molecules as reactants, with the olefinic species depicted in blue. The reaction mechanism is as follows: After co-adsorption of the olefin and n-butane within the zeolite pore (C1), protonation of the olefin with the proton from the acid site TS1(C1-C2) yields the tert-butyl-cation, co-adsorbed with n-butane (C2). The next reaction requires a rotation of the two co-adsorbed hydrocarbons by 180°. It is assumed that the associated rotational barriers are negligible based on previous work,[116] where rotational barriers for protonated methanol in H-ZSM-5 have been calculated to be up to 20 kJ/mol. After rotation, n-butane now faces the acid site. Subsequently, a concerted reaction takes place as n-butane gets deprotonated by the acid site while simultaneously a hydride is transferred from n-butane towards the isobutyl cation to form isobutane and 2-butene (C3). This reaction is the rate determining step of the HT mechanism in H-SSZ-13, and the corresponding transition state is shown together with important bond distances in Fig. 5.2. The olefinic species that is hydrogenated in this reaction is, however, not limited to just isobutene. The transition state for the hydrogen shift reaction from the Brønsted acid site to the olefin is structurally very similar for olefinic substrates of non-C_4 chain lengths. Likewise, the alkane substrate may also not be limited to n-butane; however, seeing as n-butane is the main reactant in our reaction, reactions involving other alkane species have not been considered here. Instead, to investigate the reactions leading to propane and pentane as products, propene and 2-methyl-2-butene have been investigated as the reactant olefinic species for the HT mechanism. For propene as the reactant, the transition

states TS(C1-C2) and TS(C2-C3) of Fig. 5.1 are condensed as TS(D2-D3) in Fig. 4.2, and for 2-methylbut-2-ene as the reactant as TS(D7-D8).

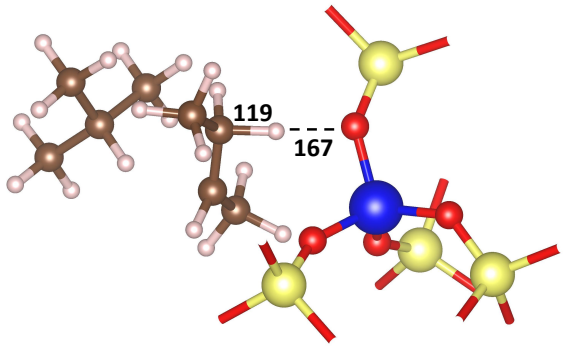

Figure 5.2.: Transition state image of the RDS of the intermolecular hydrogen transfer mechanism, TS(C2-C3), which is the protonation of 2-butene with isobutane co-adsorbed in the pore, in the H-SSZ-13 zeolite. Coloring: blue - Al, yellow - Si, red - O, brown - C, white - H. Key bond distances are given in pm.

It is, in principle, also possible to think of ethene as well as longer-chain olefins like hexanes to be the substrates for these hydrogen shift reactions. However, the barrier for the ethene protonation is expected to be very high due to the necessary formation of a primary carbocation, which is very unstable. In the case of C_{6+} hydrocarbons, the confinement effects of the zeolites, especially in the case of H-SSZ-13 with a rather small zeolite pore, need to be taken into account. In the case of C_5 and C_4 as the reactants, the zeolite pore is already very full, containing nine carbon atoms in total. Any more carbon atoms may lead to repulsive and destabilizing interactions between the reactants and the zeolite framework, as well as the inability of the reactants to freely rotate in the cavity. The conclusion therefore is that these transition states are very unlikely, i.e. for them to have very high barriers, and the investigations were limited to the hydration of C_3 to C_5 olefins.

A free energy diagram for the HT mechanism converting either propene, isobutene or 2-methylbut-2-ene to their corresponding alkane is shown in Fig. 5.3. Similar to the case of the bimolecular mechanism, two hydrocarbons have to co-adsorb within the zeolite pore, which is entropically unfavorable. Using isobutene and n-butane in the gas phase as the reference (black line), the highest barrier would be the protonation of 2-butene TS(C2-C3) to yield 2-butene and isobutane at 203 kJ/mol. This barrier is even higher than that of the bimolecular mechanism by 13 kJ/mol, and is somewhat too high for the reaction to take place at reasonable rates at reaction conditions typically employed. For example, the rate constant of an elementary process with a barrier of 203 kJ/mol at 400 °C is $2.5 \cdot 10^{-2}$ s^{-1}. The heights of the RDS barriers differ only slightly for all three reactions, ranging from 197 kJ/mol to 205 kJ/mol. Interestingly, the RDS barrier changes when propene is used as a substrate to TS(C1-C2). This can be explained by the fact that the protonation of the shorter chain length substrate propene is energetically more demanding than the protonation of butene. Comparing the transition states TS(C2-C3) for isobutene and 2-methylbut-2-ene as substrates with each other, it is obvious that the RDS barrier does not change much between the two, seeing as the reactive moiety of the transition state stays the same with the protonation of 2-butene, and only the co-adsorbed substrate is different, which does not partake in the reaction in a meaningful way.
Another interesting fact here is that when looking at the transition states TS(B1-B2), TS(B4-B5) and TS(C2-C3), all of them describe the same reaction, which is the protonation of 2-butene by the acid proton of the zeolite. The differences between the transition state

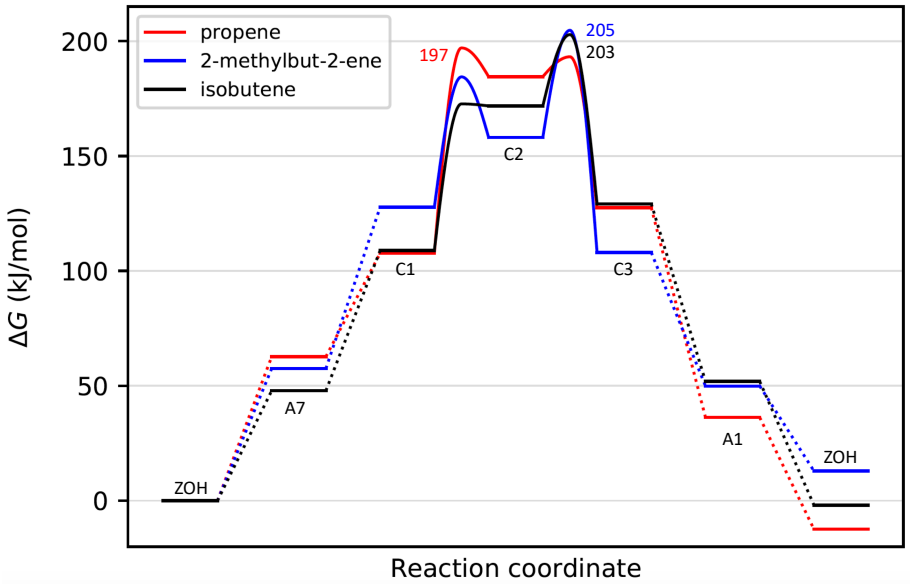

Figure 5.3.: Free energy diagram of the hydrogen transfer mechanism to convert either propene (red), isobutene (black) or 2-methylbut-2-ene (blue) together with n-butane to 2-butene and the respective alkane. The barrier heights for the respective RDSs are given explicitly; all other free energies are given in Fig. A.1 in the appendix. The reference for each reaction is the clean zeolite and the respective olefin in the gas phase. All energies and barriers are given in kJ/mol at T=400 °C and p=1 bar.

structures is the second hydrocarbon co-adsorbed in the zeolite, which in the three cases here are 2-butene, isobutene and isobutane, respectively. One might guess that since the basic structure for the transition state is essentially the same, the barriers should therefore also be similar. However, in the case of H-SSZ-13, there is a difference of 31 kJ/mol between the transition states TS(C2-C3) and TS(B4-B5). This indicates that there are other chemical effects that need to be taken into consideration for these transition states.

5.2.2. AFI and MOR

The hydrogen transfer mechanism converting n-butane and isobutene into 2-butene and isobutane has been calculated for all other investigated zeolites, and the resulting free energy diagrams are shown in Fig. 5.4a-c for the CHA, AFI and MOR zeolites, respectively. The RDS barriers for each zeolite are given in Table 5.1. For all zeolites, the protonation of 2-butene, TS(C2-C3), is the rate determining step. This is due to the fact that the 2-butene protonation forms a secondary carbocation, whereas the isobutene protonation TS(C1-C2) forms a tertiary and therefore more stable carbocation.
The calculated free energy barriers are overall rather high, with H-MgAlPO-34 showing the lowest barrier at 181 kJ/mol. H-MgAlPO-5 has a fairly similar barrier of 189 kJ/mol. Again, as previously discussed for the bimolecular mechanism, the errors in entropy due to the harmonic approximation are expected to be possibly up to 40 kJ/mol for this mechanism as well, as it also involves co-adsorption of two C_4 species into the zeolite pore. Especially for the Mg-substituted zeotypes, consideration of this error leads to reasonable reaction barriers at the given temperature (e.g. 140-150 kJ/mol). This is, however, not the case for most of the other calculated zeotypes here, as the barriers get increasingly large. For zeolites having reaction barriers of over 200 kJ/mol, rate constants will be very low, as has already been shown for the case of H-SSZ-13.

Looking back at the discussion of the origin of olefinic species, it is clear that for the HT mechanism to take place, some amount of olefinic species has to be present from the

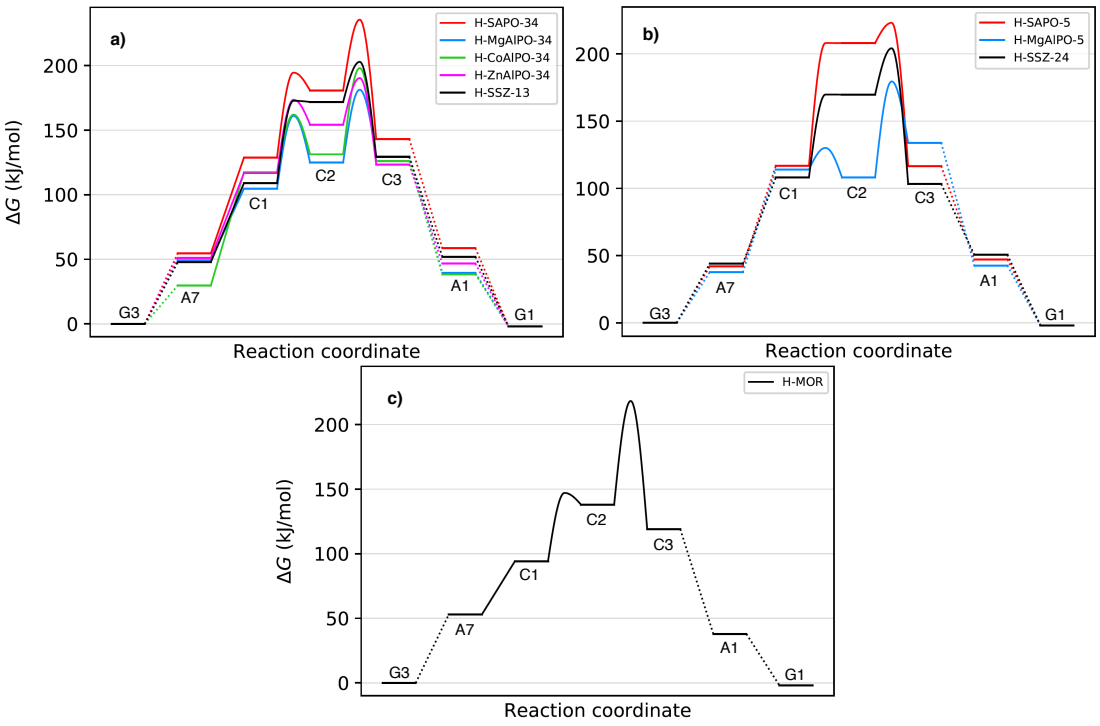

Figure 5.4.: Free energy diagrams of the hydrogen shift mechanism to convert isobutene and n-butane to isobutane and 2-butene, for all investigated zeotypes of a) CHA, b) AFI and c) MOR structure. The RDS barriers are given for each zeolite in Table 5.1. All energies and barriers are given in kJ/mol at T=400 °C and 1 bar.

Table 5.1.: RDS barriers of the intermolecular hydrogen transfer mechanism, converting isobutene and n-butane to isobutane and 2-butene,for all investigated zeolites. The RDS for all zeolites is the protonation of isobutane, TS(C2-C3). RDS barriers are given in kJ/mol at T=400 °C.

Zeolite	RDS barrier
H-SSZ-13	203
H-SAPO-34	236
H-MgAlPO-34	181
H-CoAlPO-34	198
H-ZnAlPO-34	190
H-SSZ-24	204
H-SAPO-5	223
H-MgAlPO-5	189
H-MOR	218

start. However, as discussed in the second point of section 5.1, coking of the catalyst is a reasonable source of at least a small amount of unsaturated hydrocarbons. These olefinic species may be able to, through means of the HT mechanism, produce a small amount of short-chain olefins, like 2-butene. Once butene is formed for the first time, it is not only able to isomerize to isobutene, but is also reproduced by dehydration of n-butane, while isobutene is hydrogenated to isobutane. This strengthens the point that for alkanes to be formed through the HT mechanism, only a small initial amount of olefins is needed. This point is additionally backed by experimental work of Wulfers & Jentoft,[25] who have shown that the addition of even very small amounts of butene (on the

ppm scale) to the n-butane reaction feed results in an immediate rise in concentration of isobutane as well as propane and pentanes. The n-butane reaction takes place initially due to very small amounts of 2-butene as impurities that have been measured to always exist in the reactant feed (no less than 10 ppm of n-butene), even when using an alkene trap.

Some clearer insights into the effects that olefinic species have on the product formation rate as well as product distribution may be won by performing kinetic simulations in the future. By choosing the same reaction conditions for the simulations as they are in a specific experiment, they can be compared to each other to decipher whether the here investigated mechanistic scheme and the calculated reaction barriers can accurately predict the actual product formation.

6. Linear Scaling Relations

6.1. General Points

In this chapter, the relationships between the calculated RDS barriers of the previous chapters and the acidity of the specific zeolites will be explored. The ammonia heat of adsorption ($\Delta_{\text{ads.}}^{\text{NH}_3}$) is a widely used descriptor able to gauge the reactivity of similar systems in terms of transition state energies[45–47] and the influence of the framework.[117] The ammonia heats of adsorption calculated here are shown in Table 6.1 for all investigated catalysts at T=400 °C and p=1 bar at the M06 level of theory. In general, a lower $\Delta_{\text{ads.}}^{\text{NH}_3}$ value indicates a higher acidity and therefore reactivity of the catalyst. Looking at the calculated $\Delta_{\text{ads.}}^{\text{NH}_3}$ values, the H-MgAlPO-34 zeolite is expected to be the most acidic of these zeolites, while H-SAPO-34 is the least acidic. Interestingly, when comparing the CHA zeotypes with AFI zeotypes, the ones with the same type of substitution do not necessarily provide the same shift in reactivity. For example, while the SSZ-13 zeolite has a 22 kJ/mol lower $\Delta_{\text{ads.}}^{\text{NH}_3}$ than SSZ-24, the SAPO-34 structure has a 2 kJ/mol higher $\Delta_{\text{ads.}}^{\text{NH}_3}$ than SAPO-5. This may be due to the different frameworks of the zeolites, e.g. hydrogen bonds between the H atoms of NH_3 and the framework oxygen, leading to different framework effects that influence the adsorption of NH_3 in the pore.

Table 6.1.: Calculated ammonia heats of adsorption $\Delta_{\text{ads.}}^{\text{NH}_3}$ at the M06 level of theory for all investigated zeotypes at T=400 °C and 1 bar, given in kJ/mol, referenced to the respective clean zeotype and NH_3 in the gas phase.

	H-SSZ-13	H-SAPO-34	H-MgAlPO-34	H-CoAlPO-34	H-ZnAlPO-34	H-SSZ-24	H-SAPO-5	H-MgAlPO-5	H-MOR
$\Delta_{\text{ads.}}^{\text{NH}_3}$	-125.7	-98.6	-142.1	-134.8	-131.8	-102.6	-100.1	-130.9	-124.9

Correlations between $\Delta_{\text{ads.}}^{\text{NH}_3}$ and different important transition states have been found for the Methanol-to-DME reaction scheme for a variety of different zeolites and zeotypes by Arvidsson et al.[47] The correlations are approximately linear and are therefore called linear scaling relations. These scaling relations have been used quite frequently in zeolite catalysis.[46,47,106,117–121] While the shift in frequency of the Brønsted hydroxyl group that is caused by the adsorption of CO has also been shown to be a reliable descriptor of the reactivity of a system, the ammonia heat of adsorption is usually used instead.[47,106] This has also been recently done by Cnudde et al.,[106] who investigated linear scaling relations between $\Delta_{\text{ads.}}^{\text{NH}_3}$ and the electronic adsorption energies of 2-butene, 2-butoxide, isobutoxide and isobutene for a wide variety of AFI zeotypes. Additionally, linear scaling relations were found for the reaction free energies of the isobutene protonation reaction, but for a smaller amount of AFI zeotypes. This substantiates that these scaling relations are a powerful tool to predict reaction energies and barriers in zeolite catalysis, which will be used in the following for the mechanisms presented in this thesis.

6.2. Scaling Relations of Transition States

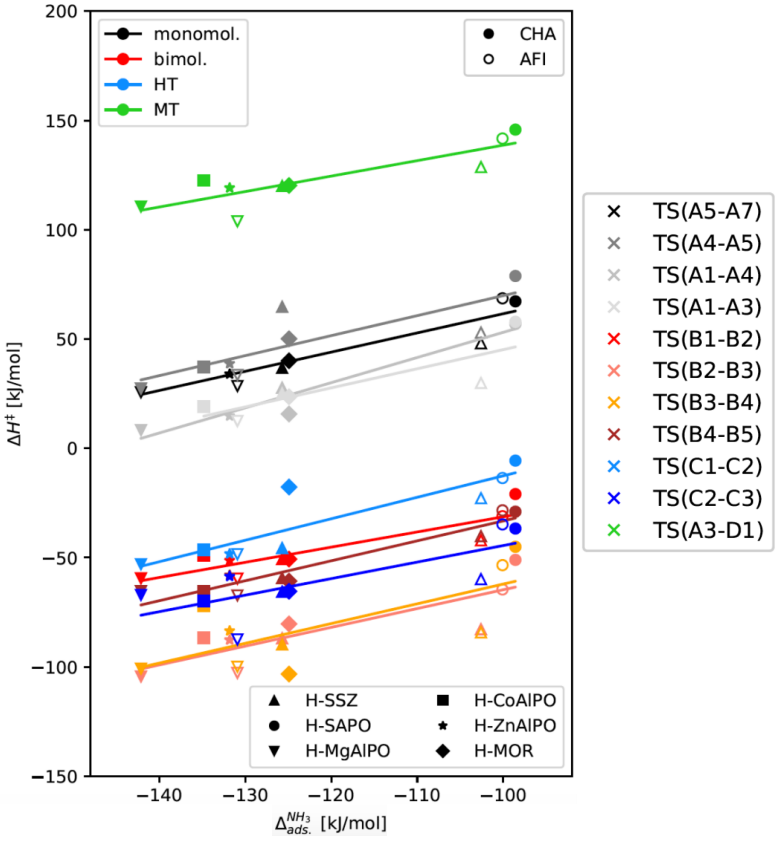

Figure 6.1.: Linear scaling relations for a set of selected transition states, related to the ammonia heat of adsorption of the specific zeolite. Slopes as well as mean average errors of key scaling lines are additionally given in the figure.

Table 6.2.: Functions and mean average errors (MAEs) of the scaling lines of Fig. 6.1.

Transition state	MAE [kJ/mol]	Scaling line (y=ax+b)
TS(A5-A7/A6-A7)	4.3	0.88x + 149.50
TS(A4-A5)	7.3	0.92 + 161.50
TS(A1-A4)	4.1	1.15x + 168.30
TS(A1-A3)	6.2	0.88x + 132.60
TS(B1-B2)	4.3	0.69x + 38.17
TS(B2-B3)	6.9	0.86x + 21.36
TS(B3-B4)	11.9	0.90x + 28.38
TS(B4-B5)	4.1	0.91x + 58.21
TS(C1-C2)	5.8	0.98x + 85.79
TS(C2-C3)	8.2	0.75x + 31.24
TS(A3-D1)	5.0	0.71x + 209.50

We use the enthalpy contributions of most of the transition states calculated here, consisting of four transition states of the monomolecular mechanism, the rate determining transition state of the methyl transfer mechanism, as well as all calculated transition states of the bimolecular and hydrogen transfer mechanisms, to relate them to the ammonia heat of adsorption, which is done in Fig. 6.1. Note that the focus only lies in the enthalpy contribution to the free energy barriers because the entropic contribution does not scale with the ammonia heat of adsorption. The monomolecular transition states are shown in

black, bimolecular in red, hydrogen transfer (HT) in blue and methyl transfer (MT) in green. Table 6.2 lists the mean average errors (MAEs) as well as the functional equations of all scaling lines.

Taking a look at the scaling lines, their slopes are all within a range of 0.7 to 1.2, indicating a consistent dependency of the transition state barriers on the zeolite acidity. The conclusion is that for all reaction mechanisms herein, the investigated catalysts have a mostly similar dependency on the zeolite acidity. Only a few outliers can be seen, like e.g. the TS(C1-C2) transition state in mordenite. This allows the use of these scaling lines as a predictive model for the enthalpy contributions of these reactions. The MAEs of the scaling lines range from 4.1 kJ/mol for TS(B4-B5) to 11.9 kJ/mol for TS(B3-B4), with the overall MAE being 6.2 kJ/mol. It was previously discussed that Goncalves et al. reported the accuracy of our applied method to yield results within a 7 kJ/mol MAE range for transition states;[40] the overall MAE shown here being slightly lower than this method-based error further substantiates the applicability and quality of these scaling lines as a predictive model.
The accuracy of the scaling lines in Fig. 6.1 is now verified by them being used to predict the reaction enthalpies calculated herein. The predicted enthalpies are then compared to the calculated enthalpies, referenced to the enthalpies in H-SSZ-13:

$$\Delta\Delta H_{\text{calculated}} = \Delta H^{\text{Zeotype}}_{\text{calculated}} - \Delta H^{\text{H-SSZ-13}}_{\text{calculated}} \tag{6.1}$$

$$\Delta\Delta H_{\text{predicted}} = \Delta H^{\text{Zeotype}}_{\text{predicted}} - \Delta H^{\text{H-SSZ-13}}_{\text{predicted}} \tag{6.2}$$

This is done in the parity plot in Fig. 6.2a. The black reference line in the middle represents the H-SSZ-13 reference. As can be seen by the dashed lines which indicate an error range of ±10 kJ/mol, most of the predicted enthalpies are within this range. Out of the outliers that have a larger deviation, the most noticeable is the TS(A4-A5) transition state (n-butoxide to isobutoxide), for which all other zeolites have a positive deviation larger than 10 kJ/mol. This is directly caused by the large deviation of the H-SSZ-13 data point for TS(A4-A5) from the respective scaling line in Fig. 6.1. The overall MAE for all data points shown in Fig. 6.2a at 8.6 kJ/mol shows that the scaling relations presented here have an accuracy similar to that of the quantum-chemical method used to calculate the enthalpies that they are supposed to predict. One can therefore conclude that the scaling relations that utilize the ammonia heat of adsorption as an acidity descriptor can indeed be used to predict the enthalpy contributions to the free energy barriers within a mean uncertainty of less than 10 kJ/mol.
Additionally, it is investigated how well the trends in energies and barriers between zeolites are preserved at different levels of accuracy. For this, the differences in energies and barriers between the H-SSZ-13 zeolite and all other zeotypes are calculated as ΔΔH values for each method:

$$\Delta\Delta H^{\text{method}} = \Delta H^{\text{method}}_{\text{zeotype}} - \Delta H^{\text{method}}_{\text{H-SSZ-13}} \tag{6.3}$$

A similar approach for the investigation of the accuracy of the PBE-D3 method in comparison to higher-level methods in zeolite catalysis by Plessow and Studt has shown that this approach is indeed able to discern these types of trends.[39] This is done in Fig. 6.2b for the enthalpy contributions of almost all investigated intermediates (squares) and transition states (circles) of the investigated zeolite structures. The detailed table that lists all data points depicted can be found in the appendix under Table D.2.

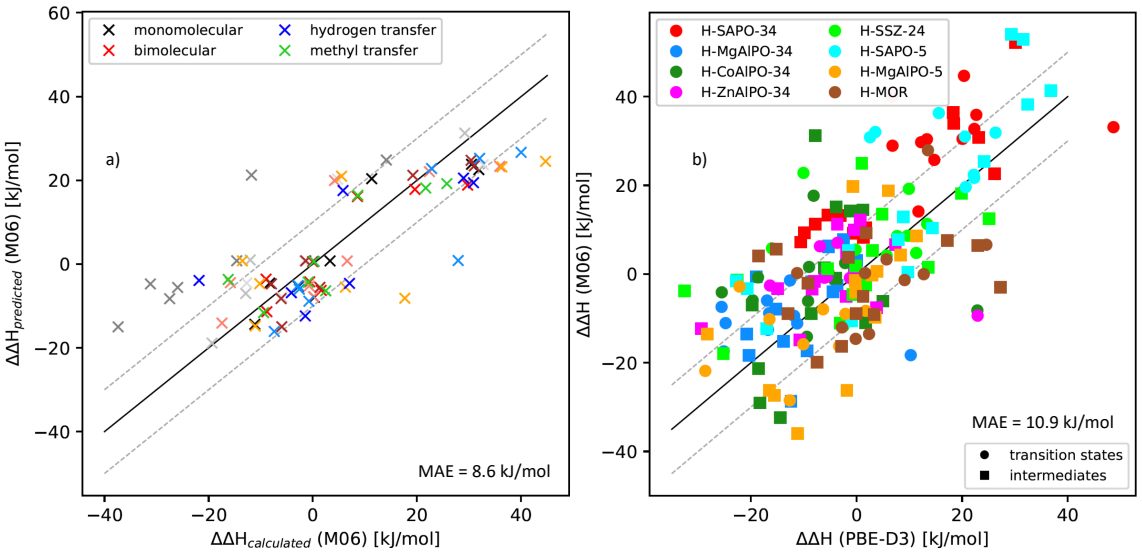

Figure 6.2.: a) Parity plot showcasing the accuracy of the predicted ΔH values, referenced to the H-SSZ-13 zeolite, represented by the black scaling line. The dashed gray lines indicate a range of ±10 kJ/mol. The coloring convention for the transition states is taken over from Fig. 6.1. b) Parity plot showing most of the intermediate structures and barriers with respect to the H-SSZ-13 zeolite at the PBE-D3 and the M06 level of theory. The black line represents the H-SSZ-13 zeolite, while the gray dashed lines indicate a range of ±10 kJ/mol.

Similar to Fig. 6.2a, the black line represents the H-SSZ-13 reference, while the dashed gray lines indicate an error range of ±10 kJ/mol. The strongly acidic zeolites like H-MgAlPO-5 and H-MgAlPO-34 can be found at lower ΔΔH values, while the less acidic zeolites like H-SAPO-34 and H-SAPO-5 can be found at higher ΔΔH values. The bulk of the data points lies within the range of ±10 kJ/mol, while the majority of data points with a larger deviation than that have a positive deviation of >10 kJ/mol. This is also the cause of the slightly larger positive MAE of 10.9 kJ/mol for all data points.
For the mechanisms investigated herein, the description of reaction energies and barriers is accurate for all zeolites and zeotypes except H-SAPO-34 (red data points), for which the large majority of data points can be found significantly above the +10 kJ/mol deviation line. This results in slightly larger errors (roughly 6 kJ/mol larger on average) to be expected for this specific catalyst. For instance, only the H-SAPO-34 zeolite data points yield a MAE of 14.6 kJ/mol, while all other zeotypes excluding H-SAPO-34 yield a MAE of 10.3 kJ/mol. Keeping these deviations in mind, this investigation still gives a strong argument towards the predictive power of DFT towards reaction energies and barriers showcased by the parity plots in Fig. 6.1.
An additional parity plot which uses the Gibbs free energy differences ΔΔG, calculated in line with Eq. 6.3, is shown in the Appendix as Fig. D.5. With an MAE of 10.5, the difference between the ΔΔG and the ΔΔH parity plots is <1 kJ/mol, which is well within the accuracy of the applied methods. This further illustrates the point that an investigation of the enthalpy contributions suffices for the calculation of linear scaling relations.

7. Summary and Outlook

This work gives new insights into the mechanistic details of the n-butane isomerization reaction catalyzed by acidic zeolites, as well as acidity and confinement effects for various zeolites and zeotypes on the reaction. Fig. 7.1 illustrates how quantum-chemical calculations of the reactions in the model zeolite H-SSZ-13 led to the proposal of new reaction mechanisms, a rigorous investigation of in total nine different zeolites and zeotypes with differing confinements and acidities, and lastly their linear correlation using scaling relations for the accurate prediction of reaction barriers.

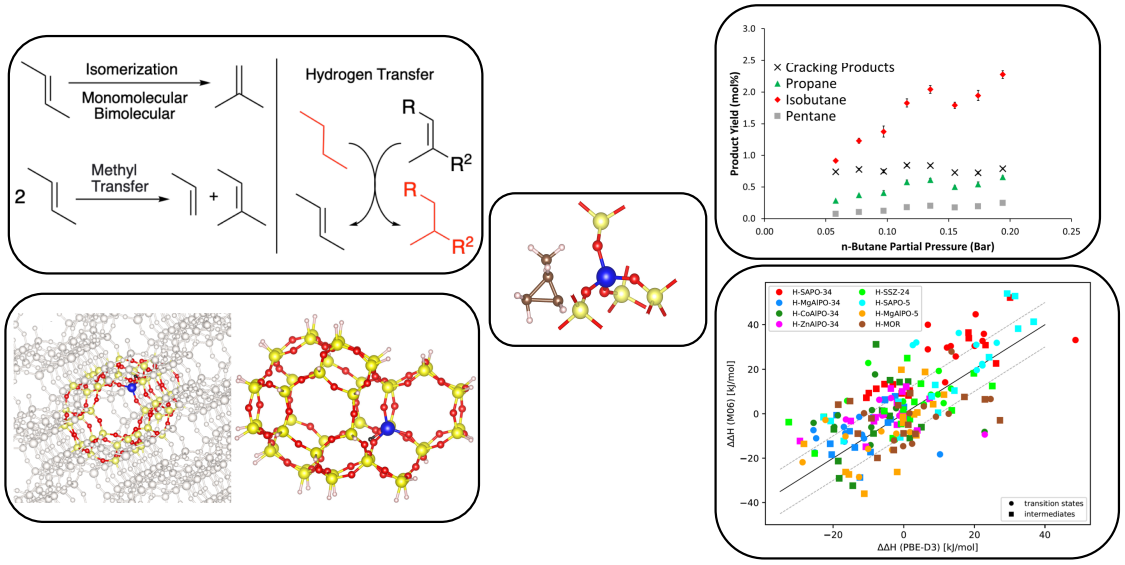

Figure 7.1.: The top left image shows an overview of the reaction mechanisms investigated in this work. This image is adapted from Ref.[104] with Copyright 2023 Frontiers in Catalysis. In the bottom left, the left image shows a cutout of a H-SSZ-13 cluster model highlighted in the periodic structure, while the right image shows the cluster model in detail. In the middle, the isomerization transition state from n-butoxide to isobutoxide is shown, which is the key transition state for the monomolecular mechanism.. In the top right, the product distribution measured in an experiment is shown. In the bottom right is a parity plot showcasing the accuracy and predictability of energies and barriers of the n-butane isomerization mechanism.

Density functional theory (DFT) calculations on the M06 level of theory utilizing a cluster model approach were used as a tool to investigate both the monomolecular and the bimolecular isomerization reaction from 2-butene to isobutene. Calculations of these reaction barriers at such a high level of computational accuracy had not been performed earlier, and the results of this work bring a clearer insight into the interplay between different reaction mechanisms for the investigated reaction.
In the first part of the research, the two main reaction mechanisms from 2-butene to

isobutene in the model H-SSZ-13 zeolite catalyst were investigated in detail. These two mechanisms are the monomolecular and bimolecular mechanisms. They were optimized in H-SSZ-13 first to compare those mechanisms to each other in detail at a reaction temperature that is generally used in experiments. The monomolecular mechanism was found to be predominant at 400 °C. Calculating the free energy barriers in a range of 100 °C to 700 °C shows that the bimolecular mechanism begins to be predominant at very low temperatures around 100 °C due to the fact that the rate determining step changes in the monomolecular mechanisms depending on the temperature. This is caused by the change in entropic contribution -TΔS for each transition state, ultimately dictating the RDS of the mechanism depending on the temperature.
Afterwards, the reaction mechanisms have been calculated in a variety of CHA, AFI and MOR zeolites and zeotypes. For other chabazite-type (CHA) zeotypes, the monomolecular mechanism was also found to be predominant, but to a lesser extent. In all investigated AFI zeolites, both mechanisms have been found to have fairly similar barriers, meaning they are competing at a temperature of 400 °C. Generally, due to their specific framework structures, the monomolecular mechanism has been found to be prevalent in CHA-type zeolites, while the bimolecular mechanism is prevalent in AFI-type zeolites. The mordenite (MOR) zeolite was calculated as a third zeolite structure, and the monomolecular mechanism was found to be predominant there as well.
A novel mechanism for the formation of non-C_4 side products, the methyl transfer mechanism, is investigated. This methyl transfer corresponds to the reverse reaction of the initiation reaction in the methanol-to-olefins process. However, this mechanism has fairly large barriers compared to the uneven β-scission barriers of a C_8 species within the bimolecular mechanism and is therefore regarded as not competing.
Lastly, a novel intermolecular hydrogen transfer mechanism is investigated, explaining how alkanes can be converted to olefins and vice versa. Through this mechanism, it can be explained how even small amounts of olefins can catalyze the n-butane isomerization reaction, as the olefins can keep being reproduced through alkanes. Additionally, the reactant n-butane can, in the presence of some olefinic species, be converted into 2-butene and partake in any isomerization mechanism. Also, after isomerization, isobutene can be transformed into the product isobutane through the same mechanism by using n-butane as a second reactant, recreating another 2-butene molecule in the process. In addition to the dehydrogenation and hydrogenation of C_4 species, side products like C_3 and C_5 olefins can also be converted to their alkane counterparts through this mechanism.
Using linear scaling relations, the dependency of the barriers of the aforementioned mechanisms on the acidity of the zeolite, described by the ammonia heat of adsorption, has been established as a great tool to be able to predict reaction barriers for not yet investigated zeolites and zeotypes. Fairly low mean average errors of those scaling lines confirm the accuracy of those predictions even at a computationally low-cost level of theory.

In general, this work helps to shed some light into the intricate interplay between monomolecular and bimolecular mechanisms for n-butane isomerization catalyzed by zeolites. This is important as the n-butane isomerization to isobutane is of great scientific interest, specifically in petroleum chemistry. Through the very high level of theory, a deeper understanding was gained about how these mechanisms compete against each other depending on zeolite acidity and confinement effects. Additional novel reaction mechanisms help to understand how alkanes can be turned into olefins using olefins, and how prominent side products of the reaction may be formed. Furthermore, the linear scaling relations established here will help to determine these mechanistic differences for a much broader range of zeolites. This will aid to further improve upon this reaction by investigating and (hopefully) finding new catalysts that improve upon currently used catalysts in terms of their applicability, reactivity and selectivity.

The reaction landscape calculated here for the H-MgAlPO-5 catalyst is compared to experimental n-butane isomerization work done by Matthew E. Potter and others. There, the findings showcased in this work were able to substantiate the experimental findings towards through which isomerization mechanism n-butane is mainly formed for this specific zeolite. However, the calculations are not yet fully able to properly predict product distributions and their reaction orders, i.e. through which mechanisms they are produced. The main attention for this lies in the differentiation between monomolecular and bimolecular mechanisms. A reason for this might be the calculated entropic contributions to the free energies, which still come with a fairly large uncertainty.

Overall, the computational method used in this thesis of correcting the periodic low-level DFT calculations with high-level cluster model DFT calculations yields very accurate intermediate and transition state enthalpies. However, the Gibbs free energy consists of both enthalpy and entropy contributions. Therefore, the necessity arises to calculate the entropy at the same level of accuracy as the enthalpy if the free energies are to be as accurate as possible. This is especially important for eventual kinetic simulations, as the rate constants are calculated with the free energy barriers, and even small changes in those barriers result in huge changes in the rate constants. Unfortunately, this is not feasible at the current time, and the entropy contributions here have been calculated using the harmonic approximation, as it is the general *modus operandi* for zeolite catalysis.

A promising alternative to the harmonic approximation that is being worked on is the thermodynamic λ-path integration.[122,123] Using this method, it is possible to compute anharmonic corrections to the harmonic approximation that remedy its errors, leading to very accurate entropy contributions, albeit currently at a very high computational cost.

Still, quantum chemical methods as well as computational resources are constantly improved. According to Moore's law, we can expect further large increases in computational power in the upcoming years. The steady development and improvement of the computational capacities give hope that in a few years time, these thermodynamic integration calculations will be part of the standard procedure when calculating the entropy contribution of reaction energies and barriers. In terms of methods, machine learning is gaining increased popularity in the last couple of years as a way to train algorithms to accurately predict chemical properties.[124–127] Considering the speed at which such methods improve and evolve, I firmly believe that machine learning is very likely to also play an important role in zeolite catalysis in the future, as its possible uses and applicability are vast.

Looking at the results I have gained during my work, and at the broad field of zeolite catalysis in general, I believe that the final goal in terms of quantum chemical calculations lies in the ability to design new catalysts which are customized to optimize the n-butane isomerization mechanism. After reaching the milestone of being able to accurately calculate both enthalpic and entropic contributions, it will be possible to scan a large amount of new catalysts using scaling relations. The highly accurate free energies will then also bring the opportunity for accurate kinetic simulations with them, with which the overall performance of model catalysis can be compared to each other in terms of reactivity and selectivity.

Appendix

A. Gibbs Free Energies Table

Gibbs free energies of all calculated intermediate structures and transition states are given for all investigated zeolites, referenced to the respective clean zeolite and 2-butene in the gas phase, at T=400 °C and p=1 bar.

Table A.1.: Calculated Gibbs free energies of all intermediate structures and transition states for each zeotype at T=400 °C and 1 bar, given in kJ/mol.

	H-SSZ-13	H-SAPO-34	H-MgAlPO-34	H-CoAlPO-34	H-ZnAlPO-34	H-SSZ-24	H-SAPO-5	H-MgAlPO-5	H-MOR
G1	0	0	0	0	0	0	0	0	0
G2							16	16	
G3	-3	-3	-3	-3	-3	-3	-3	-3	-3
A1	54	61	41	40	59	53	44	45	39
A2						66	72	82	
A3	134	167	112		133	142	154	111	130
A4	75	77	58	43	59	62	58	38	58
A5	53	90	58	39	59	67	67	57	61
A6	89		59	53	56			53	
A7	45	51	46	26	48	41	39	34	50
B1	115	129	120	119	123	104	116	135	121
B2	142	165	128	139	141	150	164	124	143
B3	151	172	130	142	138	150	153	121	132
B4	107	153	84	131	96	114	147	87	112
B5	114	121	117	112	109	115	94	112	103
C1	109	129	105	117	117	108	117	114	94
C2	172	181	125	131	154	201	208	108	138
C3	129	143	130	126	130	103	117	134	119
D1	107	115	105	100	103	124	115	109	114
D2	107	127						127	
D3	127	143	124					124	
D4	49	65	49					47	
D5	97	115	86					111	
D6	57	51	54					56	
D7	127	137	124					106	
D8	107	121	126					109	
TS(A1-A2)	129	167				83	189	139	
TS(A1-A3)	141	169		131		159		130	135
TS(A3-A5)	138	188	147		158				
TS(A3-A4)						157			
TS(A1-A4)	132	163	120		127				127
TS(A4-A5)	181	200	151	155	165				169
TS(A2-A5)							199	147	
TS(A5-A6)	152		154	163	161			148	
TS(A6-A7)	89		82	78	90			64	
TS(A5-A7)		183				172	182		163
TS(B1-B2)	190	203	165	179	171	181	204	154	177
TS(B2-B3)	180	218	160	174	165	177	192	155	195
TS(B3-B4)	179	214	159	187	176	167	199	154	162
TS(B4-B5)	72	203	157	163	165	189	201	152	177
TS(C1-C2)	173	195	161	162	174	162	187	130	147
TS(C2-C3)	203	236	181	198	190	204	223	180	218
TS(A3-D1)	227	260	217	236	228	242	247	223	237
TS(D2-D3)*)	196	242	188					185	
TS(D5-D6)	222	249	206					207	
TS(D7-D8)*)	204		177						

*) TS(D2-D3) and TS(D7-D8) both represent the higher barrier of two protonation reactions, as is discussed in chapter 5. For TS(D2-D3) this is the protonation of propene, and for TS(D7-D8) it is the protonation of 2-butene.

B. Acronyms

AIMD	Ab Initio Molecular Dynamics
ARPESS	Automated Relaxed Potential Energy Surface Scan
ASE	Atomic Simulation Environment
CCSD(T)	Coupled Cluster Singles Doubles and perturbative Triples
cGTO	contracted Gaussian-Type Orbital
CHA	Chabazite
CI	Configuration Interaction
CM	Cluster Model
D3	Grimme's dispersion correction model
DFT	Density Functional Theory
DLPNO	Domain-based Local Pair Natural Orbitals
FAU	Faujasite
FER	Ferrierite
FS	Final State
GGA	Generalized Gradient Approximation
GTO	Gaussian-Type Orbital
HF	Hartree-Fock
HT	Hydrogen Transfer
IS	Initial State
KS	Kohn-Sham
LDA	Local Density Approximation
MAE	Mean Absolute Error
MEP	Minimum Energy Path
mGGA	Meta-Generalized Gradient Approximation
MHYB	Meta-Hybrid Exchange-Correlation functional
MOR	Mordenite
MP2	Møller-Plesset 2nd order perturbation theory
MT	Methyl Transfer
MTBE	Methyl-tert-butyl ether
MTO	Methanol-to-olefins Process
M06	Minnesota MHYB functional
NEB	Nudged Elastic Band Method
PAW	Projected Augmented Wave
PBE	Perdew-Burke-Ernzerhof Functional
RDS	Rate-Determining Step
RI	Resolution of the Identity
SCF	Self-Consistent Field scheme
SMS	Surface Methoxy Species
SSD	Surface Site Density
STO	Slater-Type Orbital
SZ	Sulfated Zirconia
TS	Transition State
TST	Transition State Theory
TWh	Terawatt-hours
TZVP(P)	Triple-Zeta Valence Polarization with extra Polarization function
UOP	Universal Oil Products (company)
VASP	Vienna Ab initio Simulation Package
vdW	Van-der-Waals interaction
XC	Exchange Correlation

C. Transition State Images for H-SSZ-13

Transition state images of all important transition states investigated in this thesis are shown below. Key bond distances are given in pm. The color coding in all images is: blue - Al, yellow - Si, red - O, brown - C, white - H.

C.1. Monomolecular Mechanism

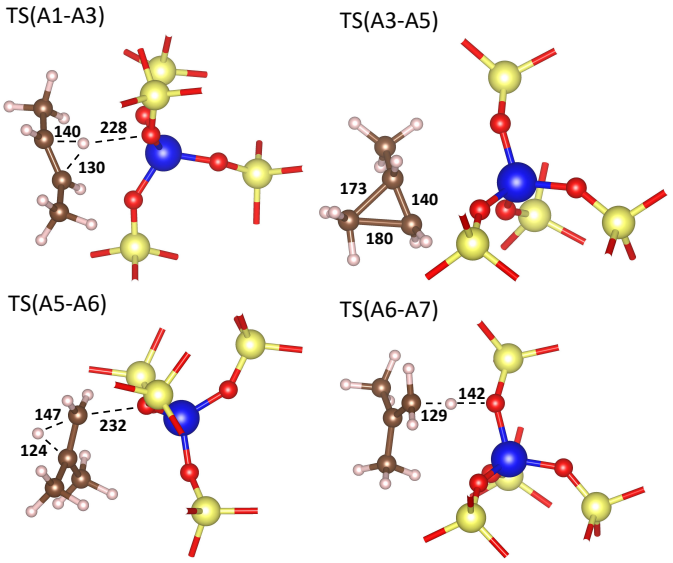

Figure C.1.: Transition state images of the monomolecular mechanism transition states in the H-SSZ-13 zeolite. Key bond distances are given in pm.

C.2. Bimolecular Mechanism

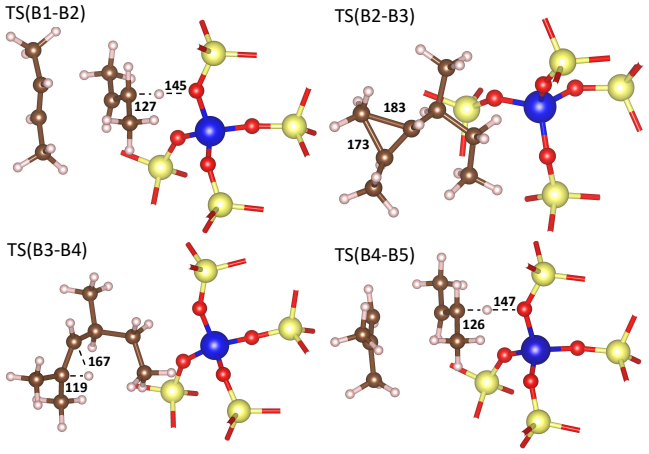

Figure C.2.: Transition state images of the bimolecular mechanism transition states in the H-SSZ-13 zeolite. Key bond distances are given in pm.

C.3. Methyl Transfer Mechanism

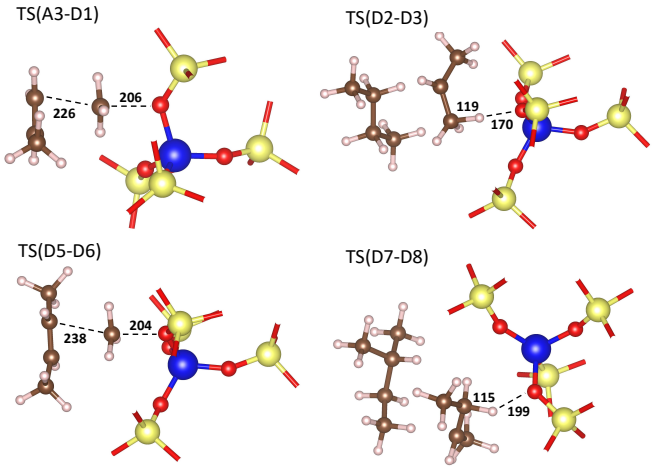

Figure C.3.: Transition state images of the methyl transfer mechanism transition states in the H-SSZ-13 zeolite. Key bond distances are given in pm.

C.4. Intermolecular Hydrogen Transfer Mechanism

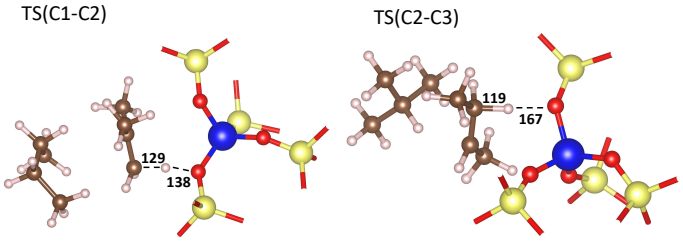

Figure C.4.: Transition state images of the intermolecular hydrogen transfer mechanism transition states in the H-SSZ-13 zeolite. Key bond distances are given in pm.

D. Supplementary Scaling Relation Data

D.1. Data for Parity Plot in Fig. 6.2

Table D.2.: Differences in Enthalpy ($\Delta\Delta$H) between the specific zeolite and H-SSZ-13. All energies are given in kJ/mol and at T=400 °C and p=1 bar.

M06	H-SAPO-34	H-MgAlPO-34	H-CoAlPO-34	H-ZnAlPO-34	H-SSZ-24	H-SAPO-5	H-MgAlPO-5	H-MOR
A1	8.239	-2.599	-0.981	-0.585	-2.456	0.445	-9.759	-8.89
A3	30.82	-17.288		-7.568	1.479	25.414	-26.212	7.523
A4	-0.525	-15.204	-32.37	-14.882	-11.058	-10.61	-27.315	-9.102
A5	13.262	-1.702	-21.327	-3.276	1.198	5.347	0.555	-2.084
A7	10.411	3.058	-6.113	6.678	1.838	7.797	4.274	3.807
B1	11.226	7.781	14.241	9.973	-1.368	-3.258	-13.573	-8.964
B2	36.473	-7.895	1.432	4.835	18.152	38.227	-0.257	6.447
B3	33.934	-13.552	-8.923	-1.628	-4.602	10.383	-26.229	-19.916
B4	52.193	-18.366	31.175	-5.002	12.445	41.367	-4.078	-2.994
B5	7.2	6.389	15.101	11.279	-3.794	-1.532	18.766	4.082
C1	13.209	6.108	14.47	12.206	24.963	52.896	19.746	5.658
C2	22.598	-28.715	-29.045	-3.42	5.276	54.006	-35.968	-5.007
C3	9.28	-0.637	-7.017	-12.274	-17.891	-12.288	8.575	-16.339
D1	9.166	-4.028	-11.006	0.018	13.515	12.919	-1.441	9.252
TS(A1-A3)	32.717		-5.938		3.754			
TS(A3-A5)	33.12	-18.287	-8.204	-9.383				
TS(A1-A4)								-12.025
TS(A4-A5)	14.104				-11.781			-14.610
TS(A5-A6)	30.476*)	-11.131	0.287	-2.765	11.299*)	31.872*)	-8.290	3.302*)
TS(A6-A7)		-12.576	-14.144	-0.834			-28.489	
TS(B1-B2)	29.726	-8.818	1.606	-0.609	8.566	19.596	-8.981	-0.034
TS(B2-B3)	35.89	-17.446	0.165	-0.713	4.169	22.378	-15.828	6.603
TS(B3-B4)	44.688	-11.062	17.658	6.259	5.513	36.303	-10.187	-13.513
TS(B4-B5)	30.391	-5.964	-6.097	1.354	19.209	30.991	-7.947	-1.357
TS(C1-C2)	28.935	-1.442	-4.124	7.042	5.797	30.841	-21.835	0.215
TS(C2-C3)	39.989	-7.407	-0.749	-2.593	22.8	32.024	-2.829	27.912
TS(A3-D1)	25.735	-9.449	2.473	-0.884	8.638	21.681	-16.243	0.214
PBE-D3								
A1	1.323	-3.69	-3.973	0.873	1.771	9.731	3.563	-0.048
A3	23.161	-9.397		3.823	13.611	24.167	-1.837	17.204
A4	-5.431	-13.851	-14.424	-10.721	-3.076	-0.961	-15.555	3.314
A5	-5.434	-8.549	-18.534	-14.986	-5.482	-1.539	3.844	-9.166
A7	1.711	0.028	5.004	7.36	-0.129	7.908	8.319	-1.559
B1	-7.78	-2.457	-1.162	-0.436	-22.625	-20.708	-28.276	-12.999
B2	18.33	-15.305	-6.123	-1.93	19.864	32.404	2.95	22.996
B3	18.414	-20.818	-8.564	-7.993	-0.724	14.354	-16.467	-7.463
B4	30.132	-20.397	-7.828	-1.934	25.088	36.825	-0.156	27.252
B5	-10.589	-5.318	-3.859	-3.64	-32.554	-22.746	6.054	-18.556
C1	-3.107	-5.352	1.243	0.681	0.992	31.536	-0.672	-15.199
C2	26.145	-12.414	-18.294	-8.439	3.001	29.303	-11.158	1.258
C3	-9.91	-19.026	-19.795	-29.399	-25.226	-17.011	11.391	-2.825
D1	-0.589	-4.478	1.697	-0.467	4.868	8.887	-0.259	1.805
TS(A1-A3)	22.313		-19.676		11.306			
TS(A3-A5)	48.672	10.270	22.889	22.945				
TS(A1-A4)								-2.761
TS(A4-A5)	11.727				-2.478			-0.163
TS(A5-A6)	20.084*)	-11.242	0.079	1.051	13.381*)	26.330*)	1.746	5.680*)
TS(A6-A7)		-16.780	-9.406	-6.065			-12.645	
TS(B1-B2)	12.24	-16.543	-8.996	-5.607	7.689	20.676	-2.104	12.729
TS(B2-B3)	22.691	-25.157	-5.533	-6.147	5.705	22.214	-10.085	24.597
TS(B3-B4)	20.355	-24.799	-8.127	-6.937	-0.181	15.582	-16.496	2.37
TS(B4-B5)	13.328	-16.958	-9.182	-5.693	9.925	20.544	-6.335	9.106
TS(C1-C2)	6.813	-12.606	-25.53	-3.622	-16.025	2.56	-28.65	-11.246
TS(C2-C3)	6.819	-25.567	-18.657	-16.382	-10.056	3.55	-22.166	13.53
TS(A3-D1)	14.728	-11.807	-2.164	-1.257	9.672	22.293	-3.294	1.605

*) As the isobutyl cation (A6) is an unstable intermediate, the transition state TS(A5-A7) is shown here and compared to the H-SSZ-13 TS(A5-A6).

D.2. Parity Plot of the ΔΔG Free Energy Differences

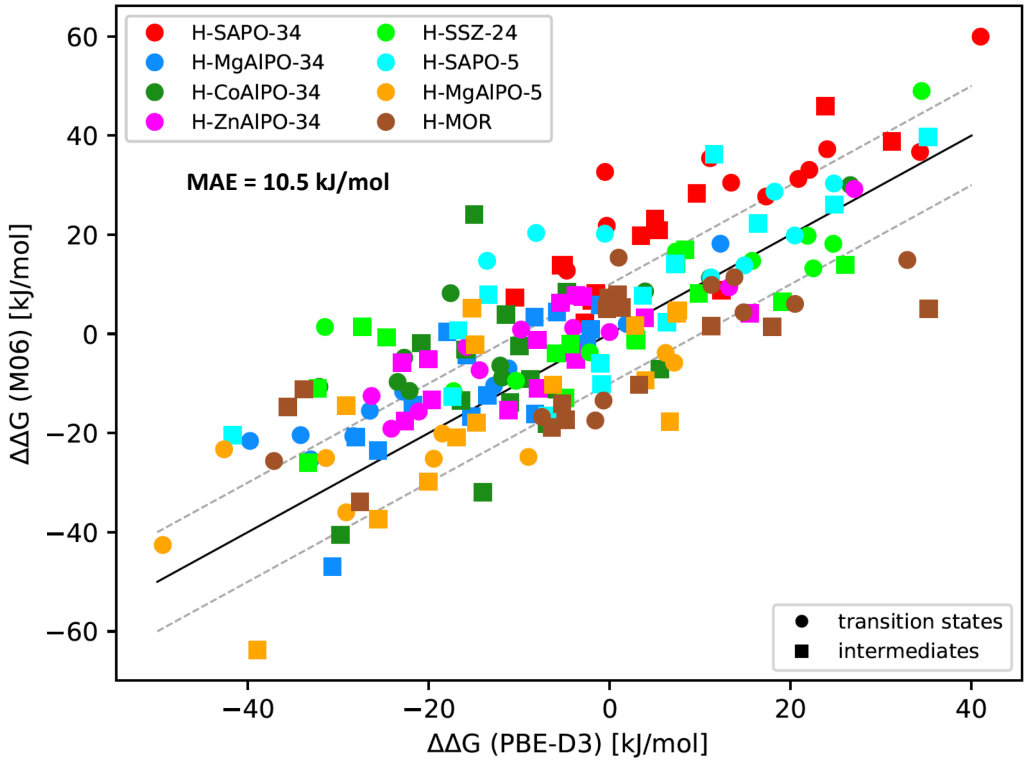

Figure D.5.: Parity plot showing the free energy differences for most of the intermediate structures and barriers with respect to the H-SSZ-13 zeolite at the PBE-D3 and the M06 level of theory. The black line represents the H-SSZ-13 zeolite, while the gray dashed lines indicate a range of 10 kJ/mol.

Acknowledgements

In the following I would like to thank the people who have supported me during my PhD work.

First of all, I am obliged to Professor Felix Studt, who deserves special gratitude for allowing me to work in his group and in an interesting scientific consortium, granting me valuable life experiences for the future and supporting me in my application for a scholarship after my PhD.

Secondly, I want to thank every member at the KIT that I have had the pleasure of working with and have helped creating a warm, friendly and joyous working environment for me and everyone else. This includes first and foremost my supervisor Phillip P., who never failed to lend a helping hand and support me with great advice when I had problems understanding things (which was basically always) and had great patience in guiding me in the right directions.
All other group members that I had the pleasure of working with deserve a mention as well; this includes the other postdocs of this group, Dima and Jelena. As for PhD students, for me they are somewhat split into two groups due to the pandemic isolating everyone from one another for the better part of my time as a PhD student. The first "half" of my PhD colleagues include Elizabeth, Tiago, Amir, Eduard, Ashley, Mikhal, Chandra and Sabrina, while the second "half" includes Philipp H, Annika, Sarah, Jiachen, Karnajit, Aleksandr I, Aleksandr II, Enrico, Claude, Thanh-Namh, Bogdan and Tilman.

As a member of the TotalEnergies consortium on metal nanocatalysis, I had the pleasure of working together with many members of the TotalEnergies company, as well as members of other universities like the University of Southampton, who I intensively collaborated with. Special thanks therefore go to TotalEnergies itself for funding this project, as well as Bart and Kamila for their great cooperation and interesting and helpful discussions on the subject matter. Further thanks go out to my collaborators of the University of Southampton, namely Matt, Robert, Evangeline and Marina, who did tremendous work on the experimental side of the project as well as writing up articles about our work.

Very importantly, I want to thank my parents as well as my grandmother for their continuous support during my studies, not only during my time as a PhD student, but also for the entirety of my scientific career.

Last, but certainly not least, my good friends Robert, Patrick and Marc deserve special appreciation for always helping me and giving me advice when needed, proof-reading my thesis together with Philipp H and Jiachen, and giving me the motivation to work on my project and thesis a little bit more than I would have otherwise.

List of Publications

[1] L. Spiske, P. N. Plessow, K. Kazmierczak, B. Vandegehuchte, and F. Studt, Theoretical investigation of catalytic n-butane isomerization over the H-SSZ-13 zeolite, *Front. Catal.* **2023**, *3, 1213803*.

[2] M. E. Potter, J. Amsler, L. Spiske, P. N. Plessow, T. Asare, M. Carravetta, R. Raja, P. A. Cox, F. Studt, and L-M. Armstrong, Combining theoretical and experimental methods to probe confinement within microporous solid-acid catalysts for alcohol dehydrations, *ACS Catal.* **2023**, *13, 9, 5955-5968*.

[3] L. Spiske, P. N. Plessow, K. M. Kazmierczak, B. Vandegehuchte, and F. Studt, Towards predicting trends for n-butane isomerization in zeolite catalysis, *in preparation.*

[4] M. E. Potter, L. Spiske, P. N. Plessow, E. B. McShane, M. Carravetta, A. E. Oakley, T. Bere, J. H. Carter, G. J. Hutchings, B. Vandegehuchte, K. M. Kazmierczak, F. Studt, and R. Raja, Combining computational and experimental studies to gain mechanistic insights for n-butane isomerisation with a model microporous catalyst, *to be resubmitted to Catal. Sci. Techol.*

[5] L. Spiske, P. N. Plessow, K. Kazmierczak, B. Vandegehuchte, and F. Studt, Kinetic simulations of the n-butane isomerization over acidic mordenite, *in preparation.*

Poster Presentations

- L. Spiske, P. N. Plessow, K. Kazmierczak, B. Vandegehuchte, and F. Studt, "Theoretical investigations of the catalytic n-butane isomerization with the H-SSZ-13 zeolite", *International Conference on Theoretical Aspects of Catalysis (ICTAC online scientific meeting)*, Lyon, France, June 14-30, 2021.
- L. Spiske, P. N. Plessow, K. Kazmierczak, B. Vandegehuchte, and F. Studt, "Theoretical investigations of the catalytic n-butane isomerization with the H-SSZ-13 zeolite", *The 27th North American Catalysis Society Meeting*, New York, US, May 22-27, 2022.
- L. Spiske, P. N. Plessow, K. Kazmierczak, B. Vandegehuchte, and F. Studt, "Theoretical investigation of the catalysis of n-butane isomerization over CHA and AFI zeolites", *International Conference on Theoretical Aspects of Catalysis*, Lyon, France, June 13-17, 2022.
- L. Spiske, P. N. Plessow, K. Kazmierczak, B. Vandegehuchte, and F. Studt, "Theoretical investigation of the catalysis of n-butane isomerization over CHA and AFI zeolites", *55. Jahrestreffen Deutscher Katalytiker*, Weimar, Germany, June 27-29, 2022.
- L. Spiske, P. N. Plessow, K. Kazmierczak, B. Vandegehuchte, and F. Studt, "Theoretical investigation of the catalysis of n-butane isomerization over CHA and AFI zeolites", *56. Jahrestreffen Deutscher Katalytiker*, Weimar, Germany, March 15-17, 2023.

Bibliography

[1] Hannah Ritchie, Max Roser, and Pablo Rosado. Energy. *Our World in Data*, 2022. https://ourworldindata.org/energy.

[2] Naeem Abas, A Kalair, and Nasrullah Khan. Review of fossil fuels and future energy technologies. *Futures*, 69:31–49, 2015.

[3] James G Speight and Baki Ozum. *Petroleum refining processes*. CRC Press, 2001.

[4] Jens Weitkamp and Yvonne Traa. Isobutane/butene alkylation on solid catalysts. where do we stand? *Catal. Today*, 49(1-3):193–199, 1999.

[5] James H Gary, Glenn E Handwerk, and Mark J Kaiser. *Petroleum refining: technology and economics*. CRC press, 2007.

[6] Mohammad Soltanieh, Angineh Zohrabian, Mohammad Javad Gholipour, and Eugenia Kalnay. A review of global gas flaring and venting and impact on the environment: Case study of iran. *Int. J. Greenh. Gas Con.*, 49:488–509, 2016.

[7] TA Brzustowski. Flaring in the energy industry. *Prog. Energ. Combust.*, 2(3):129–141, 1976.

[8] Michael F Farina. Flare gas reduction: Recent global trends and policy considerations. *General Electric Company*, 2011.

[9] Yoshio Ono. A survey of the mechanism in catalytic isomerization of alkanes. *Catal. Today*, 81(1):3–16, 2003. Acid-catalyzed Transformation of Alkanes, Post Conference TOCAT.

[10] Jens Weitkamp. Zeolites and catalysis. *Solid State Ionics*, 131(1-2):175–188, 2000.

[11] Richard M Barrer. Zeolites and their synthesis. *Zeolites*, 1(3):130–140, 1981.

[12] United Stated Geological Survey (USGS). Zeolites statistics and information. `https://www.usgs.gov/centers/national-minerals-information-center/zeolites-statistics-and-information#:~:text=More%20than%20150%20zeolites%20have,molecular%20sieve%2C%20and%20catalytic%20properties.` Accessed: 2023-06-14.

[13] ML Poutsma. Zeolite chemistry and catalysis. *ACS Monograph*, 171:437, 1976.

[14] Esmat Koohsaryan and Mansoor Anbia. Nanosized and hierarchical zeolites: A short review. *Chinese J. Catal.*, 37(4):447–467, 2016.

[15] Mohau Moshoeshoe, M Silas Nadiye-Tabbiruka, and Veronica Obuseng. A review of the chemistry, structure, properties and applications of zeolites. *Am. J. Mater. Sci*, 7(5):196–221, 2017.

[16] Certain data included herein are derived from clarivate web of science. ©copyright clarivate 202. all rights reserved. `https://www.webofscience.com/wos/woscc/summary/f760d150-9cc7-4a28-a108-b6cc95ae6823-918e585a/relevance/1`. Accessed: 2023-06-14.

[17] IUPAC. Compendium of Chemical Terminology, 2nd ed. (the "Gold Book"). Compiled by A. D. McNaught and A. Wilkinson. Blackwell Scientific Publications, Oxford (1997). Online version (2019-) created by S. J. Chalk. ISBN 0-9678550-9-8. `https://doi.org/10.1351/goldbook`. Accessed: 2023-06-15.

[18] Valeria Adeeva and Wolfgang MH Sachtler. Mechanism of butane isomerization over industrial isomerization catalysts. *Appl. Catal. A Gen.*, 163(1-2):237–243, 1997.

[19] Antonio Melchor, Edouard Garbowski, Michel-Vital Mathieu, and Michel Primet. Chlorinated alumina. acidic properties and catalytic activity towards n-butane isomerization. *J. Chem. Soc. Farad. T 1*, 82(6):1893–1901, 1986.

[20] GA Urzhuntsev, EV Ovchinnikova, VA Chumachenko, SA Yashnik, VI Zaikovsky, and GV Echevsky. Isomerization of n-butane over Pd–SO4/ZrO2 catalyst: Prospects for commercial application. *Chem. Eng. J.*, 238:148–156, 2014.

[21] Serge Raseev. *Thermal and catalytic processes in petroleum refining*. CRC Press, 2003.

[22] PJ Kuchar, JC Bricker, ME Reno, and RS Haizmann. Paraffin isomerization innovations. *Fuel Process. Technol.*, 35(1-2):183–200, 1993.

[23] GV Echevskii, DG Aksenov, EG Kodenev, EV Ovchinnikova, and VA Chumachenko. Activity of a sulfated zirconia catalyst in isomerization of n-butane fractions. *Petrol. Chem.*, 59:S101–S107, 2019.

[24] Makoto Hino, Sakari Kobayashi, and Kazushi Arata. Solid catalyst treated with anion. 2. reactions of butane and isobutane catalyzed by zirconium oxide treated with sulfate ion. solid superacid catalyst. *J. Am. Chem. Soc.*, 101(21):6439–6441, 1979.

[25] Matthew J. Wulfers and Friederike C. Jentoft. Mechanism of n-butane skeletal isomerization on H-mordenite and Pt/H-mordenite. *J. Catal.*, 330:507–519, 2015.

[26] Jérôme Rey, Pascal Raybaud, Céline Chizallet, and Tomáš Bučko. Competition of secondary versus tertiary carbenium routes for the type B isomerization of alkenes over acid zeolites quantified by ab initio molecular dynamics simulations. *ACS Catal.*, 9(11):9813–9828, 2019.

[27] Jérôme Rey, Axel Gomez, Pascal Raybaud, Céline Chizallet, and Tomáš Bučko. On the origin of the difference between type A and type B skeletal isomerization of alkenes catalyzed by zeolites: The crucial input of ab initio molecular dynamics. *J. Catal.*, 373:361–373, 2019.

[28] C Bearez, F Chevalier, and M Guisnet. Mechanism of butane tranformation on H mordenite I, kinetic study. *React. Kinet. Catal. L*, 22(3):405–409, 1983.

[29] Raymond A Asuquo, Gabriele Edermirth, and Johannes A Lercher. n-butane isomerization over acidic mordenite. *J. Catal.*, 155(2):376–382, 1995.

[30] Christian Tuma and Joachim Sauer. Protonated isobutene in zeolites: tert-butyl cation or alkoxide? *Angew. Chem. Int. Edit.*, 44(30):4769–4771, 2005.

[31] Mikhail V Luzgin, Alexander G Stepanov, Sergei S Arzumanov, Vladimir A Rogov, Valentin N Parmon, Wei Wang, Michael Hunger, and Dieter Freude. Mechanism studies of the conversion of 13C-labeled n-butane on zeolite H-ZSM-5 by using 13C magic angle spinning NMR spectroscopy and GC–MS analysis. *Chem-Eur. J.*, 12(2):457–465, 2006.

[32] Matias Kangas, Narendra Kumar, Elina Harlin, Tapio Salmi, and Dmitry Yu Murzin. Skeletal isomerization of butene in fixed beds. 1. experimental investigation and structure- performance effects. *Ind. Eng. Chem. Res.*, 47(15):5402–5412, 2008.

[33] Jindvrich Houvzvicka and Vladimir Ponec. Skeletal isomerization of butene: On the role of the bimolecular mechanism. *Ind. Eng. Chem. Res.*, 36(5):1424–1430, 1997.

[34] Miao He, Jie Zhang, Rui Liu, Xiu-Liang Sun, Biao-Hua Chen, and Yang-Gang Wang. Density functional theory studies on the skeletal isomerization of 1-butene catalyzed by H-ZSM-23 and H-ZSM-48 zeolites. *RSC Adv.*, 7(15):9251–9257, 2017.

[35] Matthew E. Potter, Joshua J.M. Le Brocq, Alice E. Oakley, Evangeline B. McShane, Bart D. Vandegehuchte, and Robert Raja. Butane isomerization as a diagnostic tool in the rational design of solid acid catalysts. *Catal.*, 10(9), 2020.

[36] John P Perdew, Kieron Burke, and Matthias Ernzerhof. Generalized gradient approximation made simple. *Phys. Rev. Lett.*, 77(18):3865, 1996.

[37] John P Perdew, Adrienn Ruzsinszky, Gábor I Csonka, Oleg A Vydrov, Gustavo E Scuseria, Lucian A Constantin, Xiaolan Zhou, and Kieron Burke. Restoring the density-gradient expansion for exchange in solids and surfaces. *Phys. Rev. Lett.*, 100(13):136406, 2008.

[38] John P Perdew, Adrienn Ruzsinszky, Gábor I Csonka, Oleg A Vydrov, Gustavo E Scuseria, Lucian A Constantin, Xiaolan Zhou, and Kieron Burke. Restoring the density-gradient expansion for exchange in solids and surfaces. *Phys. Rev. Lett.*, 100(13):136406, 2008.

[39] Philipp N Plessow and Felix Studt. How accurately do approximate density functionals predict trends in acidic zeolite catalysis? *J. Phys. Chem. Lett.*, 11(11):4305–4310, 2020.

[40] Tiago J Goncalves, Philipp N Plessow, and Felix Studt. On the accuracy of density functional theory in zeolite catalysis. *ChemCatChem*, 11(17):4368–4376, 2019.

[41] Yan Zhao and Donald G Truhlar. The M06 suite of density functionals for main group thermochemistry, thermochemical kinetics, noncovalent interactions, excited states, and transition elements: two new functionals and systematic testing of four M06-class functionals and 12 other functionals. *Theor. Chem. Acc.*, 120(1):215–241, 2008.

[42] Yury Minenkov, Giovanni Bistoni, Christoph Riplinger, Alexander A Auer, Frank Neese, and Luigi Cavallo. Pair natural orbital and canonical coupled cluster reaction enthalpies involving light to heavy alkali and alkaline earth metals: the importance of sub-valence correlation. *Phys. Chem. Chem. Phys.*, 19(14):9374–9391, 2017.

[43] Christoph Riplinger, Peter Pinski, Ute Becker, Edward F Valeev, and Frank Neese. Sparse maps—a systematic infrastructure for reduced-scaling electronic structure methods. ii. linear scaling domain based pair natural orbital coupled cluster theory. *J. Chem. Phys.*, 144(2):024109, 2016.

[44] Masaaki Saitow, Ute Becker, Christoph Riplinger, Edward F Valeev, and Frank Neese. A new near-linear scaling, efficient and accurate, open-shell domain-based local pair natural orbital coupled cluster singles and doubles theory. *J. Chem. Phys.*, 146(16):164105, 2017.

[45] Rasmus Y Brogaard, Reynald Henry, Yves Schuurman, Andrew J Medford, Poul Georg Moses, Pablo Beato, Stian Svelle, Jens K Nørskov, and Unni Olsbye. Methanol-to-hydrocarbons conversion: The alkene methylation pathway. *J. Catal.*, 314:159–169, 2014.

[46] Chuan-Ming Wang, Rasmus Y Brogaard, Bert M Weckhuysen, Jens K Nørskov, and Felix Studt. Reactivity descriptor in solid acid catalysis: predicting turnover frequencies for propene methylation in zeotypes. *J. Phys. Chem. Lett.*, 5(9):1516–1521, 2014.

[47] Adam A Arvidsson, Philipp N Plessow, Felix Studt, and Anders Hellman. Influence of acidity on the methanol-to-dme reaction in zeotypes: A first principles-based microkinetic study. *J. Phys. Chem. C*, 124(27):14658–14663, 2020.

[48] J. C. Slater. A simplification of the hartree-fock method. *Phys. Rev.*, 81:385–390, Feb 1951.

[49] Felix Bloch. Über die quantenmechanik der elektronen in kristallgittern. *Z. Phys.*, 52:555–600, 1929.

[50] P. A. M. Dirac. Note on exchange phenomena in the thomas atom. *Math. Proc. Cambridge*, 26(3):376–385, 1930.

[51] John P Perdew, Karla Schmidt, et al. Density functional theory and its application to materials. *Van Doren, V*, pages 1–20, 2001.

[52] Paul Adrien Maurice Dirac. The quantum theory of the electron. *P. R. Soc. Lond. A Conta.*, 117(778):610–624, 1928.

[53] Seymour H Vosko, Leslie Wilk, and Marwan Nusair. Accurate spin-dependent electron liquid correlation energies for local spin density calculations: a critical analysis. *Can. J. Phys.*, 58(8):1200–1211, 1980.

[54] John P Perdew and Yue Wang. Accurate and simple analytic representation of the electron-gas correlation energy. *Phys. Rev. B*, 45(23):13244, 1992.

[55] Chengteh Lee, Weitao Yang, and Robert G Parr. Development of the colle-salvetti correlation-energy formula into a functional of the electron density. *Phys. Rev. B*, 37(2):785, 1988.

[56] Axel D Becke. Density-functional exchange-energy approximation with correct asymptotic behavior. *Phys. Rev. A*, 38(6):3098, 1988.

[57] John P Perdew. Density-functional approximation for the correlation energy of the inhomogeneous electron gas. *Phys. Rev. B*, 33(12):8822, 1986.

[58] John P Perdew, JA Chevary, SH Vosko, Koblar A Jackson, Mark R Pederson, DJ Singh, and Carlos Fiolhais. Erratum: Atoms, molecules, solids, and surfaces: Applications of the generalized gradient approximation for exchange and correlation. *Phys. Rev. B*, 48(7):4978, 1993.

[59] BJKN Hammer and Jens K Nørskov. Electronic factors determining the reactivity of metal surfaces. *Surf. Sci.*, 343(3):211–220, 1995.

[60] Axel D Becke. Density-functional thermochemistry. i. the effect of the exchange-only gradient correction. *J. Chem. Phys.*, 96(3):2155–2160, 1992.

[61] John P Perdew, Matthias Ernzerhof, and Kieron Burke. Rationale for mixing exact exchange with density functional approximations. *J. Chem. Phys.*, 105(22):9982–9985, 1996.

[62] D. R. Hartree. The wave mechanics of an atom with a non-coulomb central field. part I. theory and methods. *Math. Proc. Cambridge*, 24(1):89–110, 1928.

[63] Christopher J. Cramer. *Essentials of Computational Chemistry - Theories and Models.* Wiley, 2004.

[64] Stefan Grimme. Accurate description of van der waals complexes by density functional theory including empirical corrections. *J. Comput. Chem.*, 25(12):1463–1473, 2004.

[65] Stefan Grimme. Semiempirical gga-type density functional constructed with a long-range dispersion correction. *J. Comput. Chem.*, 27(15):1787–1799, 2006.

[66] Stefan Grimme, Jens Antony, Stephan Ehrlich, and Helge Krieg. A consistent and accurate ab initio parametrization of density functional dispersion correction (dft-d) for the 94 elements h-pu. *J. Chem. Phys.*, 132(15):154104, 2010.

[67] Eike Caldeweyher, Sebastian Ehlert, Andreas Hansen, Hagen Neugebauer, Sebastian Spicher, Christoph Bannwarth, and Stefan Grimme. A generally applicable atomic-charge dependent london dispersion correction. *J. Chem. Phys*, 150(15):154122, 2019.

[68] Ignacio Ema, JM Garcia De La Vega, Guillermo Ramírez, Rafael López, J Fernández Rico, H Meissner, and J Paldus. Polarized basis sets of slater-type orbitals: H to ne atoms. *J. Comput. Chem.*, 24(7):859–868, 2003.

[69] Warren J Hehre, Robert F Stewart, and John A Pople. Self-consistent molecular-orbital methods. i. use of gaussian expansions of slater-type atomic orbitals. *J. Chem. Phys.*, 51(6):2657–2664, 1969.

[70] RBJS Krishnan, J Stephen Binkley, Rolf Seeger, and John A Pople. Self-consistent molecular orbital methods. xx. a basis set for correlated wave functions. *J. Chem. Phys.*, 72(1):650–654, 1980.

[71] Thom H Dunning Jr and P Jeffrey Hay. Gaussian basis sets for molecular calculations. In *Methods of electronic structure theory*, pages 1–27. Springer, 1977.

[72] Thom H Dunning Jr. Gaussian basis sets for use in correlated molecular calculations. i. the atoms boron through neon and hydrogen. *J. Chem. Phys.*, 90(2):1007–1023, 1989.

[73] David E Woon and Thom H Dunning Jr. Gaussian basis sets for use in correlated molecular calculations. iii. the atoms aluminum through argon. *J. Chem. Phys.*, 98(2):1358–1371, 1993.

[74] David E Woon and Thom H Dunning Jr. Gaussian basis sets for use in correlated molecular calculations. v. core-valence basis sets for boron through neon. *J. Chem. Phys.*, 103(11):4572–4585, 1995.

[75] Frank Jensen. Polarization consistent basis sets: Principles. *J. Chem. Phys.*, 115(20):9113–9125, 2001.

[76] Frank Jensen. Atomic orbital basis sets. *Wires. Comput. Mol. Sci.*, 3(3):273–295, 2013.

[77] Florian Weigend, Filipp Furche, and Reinhart Ahlrichs. Gaussian basis sets of quadruple zeta valence quality for atoms H–Kr. *J. Chem. Phys.*, 119(24):12753–12762, 2003.

[78] Florian Weigend and Reinhart Ahlrichs. Balanced basis sets of split valence, triple zeta valence and quadruple zeta valence quality for h to rn: Design and assessment of accuracy. *Phys. Chem. Chem. Phys.*, 7(18):3297–3305, 2005.

[79] Dimitrios A Pantazis and Frank Neese. All-electron basis sets for heavy elements. *Wires. Comput. Mol. Sci.*, 4(4):363–374, 2014.

[80] Peter E Blöchl. Projector augmented-wave method. *Phys. Rev. B*, 50(24):17953, 1994.

[81] Christian Tuma, Torsten Kerber, and Joachim Sauer. The tert-butyl cation in h-zeolites: Deprotonation to isobutene and conversion into surface alkoxides. *Angew. Chem. Int. Edit.*, 49(27):4678–4680, 2010.

[82] Christian Tuma and Joachim Sauer. Treating dispersion effects in extended systems by hybrid MP2: DFT calculations—protonation of isobutene in zeolite ferrierite. *Phys. Chem. Chem. Phys.*, 8(34):3955–3965, 2006.

[83] Niels Hansen, Torsten Kerber, Joachim Sauer, Alexis T Bell, and Frerich J Keil. Quantum chemical modeling of benzene ethylation over H-ZSM-5 approaching chemical accuracy: a hybrid MP2: DFT study. *J. Am. Chem. Soc.*, 132(33):11525–11538, 2010.

[84] Stian Svelle, Christian Tuma, Xavier Rozanska, Torsten Kerber, and Joachim Sauer. Quantum chemical modeling of zeolite-catalyzed methylation reactions: toward chemical accuracy for barriers. *J. Am. Chem. Soc.*, 131(2):816–825, 2009.

[85] Marcin Rybicki and Joachim Sauer. Ab initio prediction of proton exchange barriers for alkanes at brønsted sites of zeolite H-MFI. *J. Am. Chem. Soc.*, 140(51):18151–18161, 2018.

[86] Philipp N Plessow. Efficient transition state optimization of periodic structures through automated relaxed potential energy surface scans. *J. Chem. Theory Comput.*, 14(2):981–990, 2018.

[87] Greg Mills and Hannes Jónsson. Quantum and thermal effects in H2 dissociative adsorption: Evaluation of free energy barriers in multidimensional quantum systems. *Phys. Rev. Lett.*, 72:1124–1127, Feb 1994.

[88] Graeme Henkelman, Blas P. Uberuaga, and Hannes Jónsson. A climbing image nudged elastic band method for finding saddle points and minimum energy paths. *J. Chem. Phys.*, 113(22):9901–9904, 12 2000.

[89] Graeme Henkelman and Hannes Jónsson. Improved tangent estimate in the nudged elastic band method for finding minimum energy paths and saddle points. *J. Chem. Phys.*, 113(22):9978–9985, 12 2000.

[90] Semen A. Trygubenko and David J. Wales. A doubly nudged elastic band method for finding transition states. *J. Chem. Phys.*, 120(5):2082–2094, 01 2004.

[91] Matthias U. Bohner, Jan Meisner, and Johannes Kästner. A quadratically-converging nudged elastic band optimizer. *J. Chem. Theory Comput.*, 9(8):3498–3504, 2013. PMID: 26584106.

[92] Georg Kresse and Jürgen Hafner. Ab initio molecular-dynamics simulation of the liquid-metal–amorphous-semiconductor transition in germanium. *Phys. Rev. B*, 49(20):14251, 1994.

[93] Georg Kresse and Jürgen Hafner. Ab initio molecular dynamics for liquid metals. *Phys. Rev. B*, 47(1):558, 1993.

[94] Georg Kresse and Jürgen Furthmüller. Efficiency of ab-initio total energy calculations for metals and semiconductors using a plane-wave basis set. *Comp. Mater. Sci.*, 6(1):15–50, 1996.

[95] Georg Kresse and Jürgen Furthmüller. Efficient iterative schemes for ab initio total-energy calculations using a plane-wave basis set. *Phys. Rev. B*, 54(16):11169, 1996.

[96] Georg Kresse and Daniel Joubert. From ultrasoft pseudopotentials to the projector augmented-wave method. *Phys. Rev. B*, 59(3):1758, 1999.

[97] Ask Hjorth Larsen, Jens Jørgen Mortensen, Jakob Blomqvist, Ivano E Castelli, Rune Christensen, Marcin Dułak, Jesper Friis, Michael N Groves, Bjørk Hammer, Cory Hargus, et al. The atomic simulation environment—a python library for working with atoms. *J. Phys-Condens. Mat.*, 29(27):273002, 2017.

[98] A Alberti, P Davoli, and G Vezzalini. The crystal structure refinement of a natural mordenite. *Z. Krist. Cryst. Mater.*, 175(1-4):249–256, 1986.

[99] Rasmus Y Brogaard, Chuan-Ming Wang, and Felix Studt. Methanol-alkene reactions in zeotype acid catalysts: insights from a descriptor-based approach and microkinetic modeling. *ACS Catal.*, 4(12):4504–4509, 2014.

[100] Reinhart Ahlrichs, Michael Bär, Marco Häser, Hans Horn, and Christoph Kölmel. Electronic structure calculations on workstation computers: The program system turbomole. *Chem. Phys. Lett.*, 162(3):165–169, 1989.

[101] Malte Von Arnim and Reinhart Ahlrichs. Performance of parallel turbomole for density functional calculations. *J. Comput. Chem.*, 19(15):1746–1757, 1998.

[102] Donald W Breck and Donald Wesley Breck. *Zeolite molecular sieves: structure, chemistry, and use*. John Wiley & Sons, 1973.

[103] Martin Brändle and Joachim Sauer. Acidity differences between inorganic solids induced by their framework structure. a combined quantum mechanics/molecular mechanics ab initio study on zeolites. *J. Am. Chem. Soc.*, 120(7):1556–1570, 1998.

[104] Lucas Spiske, Philipp N. Plessow, Kamila Kazmierczak, Bart D. Vandegehuchte, and Felix Studt. Theoretical investigation of catalytic n-butane isomerization over H-SSZ-13. *Front. Catal.*, 3, 2023.

[105] Pengzhao Wang, Wenfang Zhang, Qiang Zhang, Zhusong Xu, Chaohe Yang, and Chunyi Li. Comparative study of n-butane isomerization over SO42-/Al2O3-ZrO2 and H-ZSM-5 zeolites at low reaction temperatures. *Appl. Catal. A Gen.*, 550:98–104, 2018.

[106] Pieter Cnudde, Michel Waroquier, and Veronique Van Speybroeck. Universal descriptors for zeolite topology and acidity to predict the stability of butene cracking intermediates. *Catal. Sci. Technol.*, 2023.

[107] Philipp N Plessow and Felix Studt. Olefin methylation and cracking reactions in H-SSZ-13 investigated with ab initio and dft calculations. *Catal. Sci. Technol.*, 8(17):4420–4429, 2018.

[108] Kristof De Wispelaere, Philipp N Plessow, and Felix Studt. Toward computing accurate free energies in heterogeneous catalysis: a case study for adsorbed isobutene in H-ZSM-5. *ACS Phys. Chem. Au*, 2(5):399–406, 2022.

[109] Paul J Dauenhauer and Omar A Abdelrahman. A universal descriptor for the entropy of adsorbed molecules in confined spaces. *ACS Cent. Sci.*, 4(9):1235–1243, 2018.

[110] Amber Janda, Bess Vlaisavljevich, Li-Chiang Lin, Berend Smit, and Alexis T Bell. Effects of zeolite structural confinement on adsorption thermodynamics and reaction kinetics for monomolecular cracking and dehydrogenation of n-butane. *J. Am. Chem. Soc.*, 138(14):4739–4756, 2016.

[111] Wenfang Zhang, Pengzhao Wang, Chaohe Yang, and Chunyi Li. A comparative study of n-butane isomerization over h-beta and h-zsm-5 zeolites at low temperatures: Effects of acid properties and pore structures. *Catalysis Letters*, 149:1017–1025, 2019.

[112] Donghui Jo, Suk Bong Hong, and Miguel A Camblor. Monomolecular skeletal isomerization of 1-butene over selective zeolite catalysts. *ACS Catalysis*, 5(4):2270–2274, 2015.

[113] Donghui Jo and Suk Bong Hong. Mechanisms for the reverse skeletal isomerization of n-butenes to isobutene over zeolite catalysts. *ChemCatChem*, 9(1):114–116, 2017.

[114] Wei Wang, Andreas Buchholz, Michael Seiler, and Michael Hunger. Evidence for an initiation of the methanol-to-olefin process by reactive surface methoxy groups on acidic zeolite catalysts. *J. Am. Chem. Soc.*, 125(49):15260–15267, 2003.

[115] Michel Guisnet, Luís Costa, and Fernando Ramôa Ribeiro. Prevention of zeolite deactivation by coking. *J. Mol. Catal. A Chem.*, 305(1-2):69–83, 2009.

[116] Michal Fecik, Philipp N Plessow, and Felix Studt. Simple scheme to predict transition-state energies of dehydration reactions in zeolites with relevance to biomass conversion. *J. Phys. Chem. C*, 122(40):23062–23067, 2018.

[117] Chuan-Ming Wang, Rasmus Y Brogaard, Zai-Ku Xie, and Felix Studt. Transition-state scaling relations in zeolite catalysis: influence of framework topology and acid-site reactivity. *Cat. Sci. Technol.*, 5(5):2814–2820, 2015.

[118] Chong Liu, Ionut Tranca, Rutger A Van Santen, Emiel JM Hensen, and Evgeny A Pidko. Scaling relations for acidity and reactivity of zeolites. *J. Phys. Chem. C*, 121(42):23520–23530, 2017.

[119] Yanyan Chen, Xunhua Zhao, Zhangfeng Qin, Sen Wang, Zhihong Wei, Junfen Li, Mei Dong, Jianguo Wang, and Weibin Fan. Insight into the methylation of alkenes and aromatics with methanol over zeolite catalysts by linear scaling relations. *J. Phys. Chem. C*, 124(25):13789–13798, 2020.

[120] Jeffrey Greeley. Theoretical heterogeneous catalysis: scaling relationships and computational catalyst design. *Annu. Rev. Chem. Bimol.*, 7:605–635, 2016.

[121] Chuan-Ming Wang, Yang-Dong Wang, and Zai-Ku Xie. General scaling relations and prediction of transition state energies in CHA/AlPO-34-structured zeolite catalysis related to the methanol-to-olefins conversion. *Catal. Sci. Technol.*, 9(9):2245–2252, 2019.

[122] Jérôme Rey, Charles Bignaud, Pascal Raybaud, Tomáš Bučko, and Céline Chizallet. Dynamic features of transition states for β-scission reactions of alkenes over acid zeolites revealed by AIMD simulations. *Angew. Chem.*, 132(43):19100–19104, 2020.

[123] Jonas Amsler, Philipp N Plessow, Felix Studt, and Tomáš Bučko. Anharmonic correction to adsorption free energy from DFT-based MD using thermodynamic integration. *J. Chem. Theory Comput.*, 17(2):1155–1169, 2021.

[124] Sicong Ma and Zhi-Pan Liu. Machine learning potential era of zeolite simulation. *Chem. Sci.*, 13(18):5055–5068, 2022.

[125] Takashi Toyao, Zen Maeno, Satoru Takakusagi, Takashi Kamachi, Ichigaku Takigawa, and Ken-ichi Shimizu. Machine learning for catalysis informatics: recent applications and prospects. *ACS Catal.*, 10(3):2260–2297, 2019.

[126] Sicong Ma and Zhi-Pan Liu. The role of zeolite framework in zeolite stability and catalysis from recent atomic simulation. *Top. Catal.*, 65(1-4):59–68, 2022.

[127] Aaron W Thornton, David Alan Winkler, Ming Sheng Liu, Maciej Haranczyk, and DF Kennedy. Towards computational design of zeolite catalysts for CO2 reduction. *RSC Adv.*, 5(55):44361–44370, 2015.